

**SEMMELWEIS EGYETEM**  
**DOKTORI ISKOLA**

**Ph.D. értekezések**

**2835.**

**FORGÁCH LÁSZLÓ**

**A gyógyszerészeti tudományok korszerű kutatási irányai**  
című program

Programvezető: Dr. Antal István, egyetemi tanár

Témavezető: Dr. Szigeti Krisztián, tudományos főmunkatárs

# DEVELOPMENT, IN VITRO CHARACTERIZATION & IN VIVO TESTING OF MULTIMODAL NANOPARTICLES IN AN ANIMAL MODEL

PhD thesis

**László Forgách**

Doctoral School of Pharmaceutical Sciences  
Semmelweis University



Supervisor:

Krisztián Szigeti, Ph.D

Official reviewers:

Adrienn Kazsoki, Ph.D

Gregory E.D. Mullen, Ph.D

Head of the Complex Examination Committee:

Romána Zelkó, D.Sc

Members of the Complex Examination Committee:

Viktor Fülöp, Ph.D

Dávid Juriga, Ph.D

Budapest  
2023

## Table of Contents

List of Abbreviations .....	5
1. Introduction .....	7
2.1. Biomedical imaging and contrast materials .....	9
2.2.1. Radiopharmaceuticals .....	9
2.2.2. Contrast agents .....	9
2.2. Imaging modalities .....	10
2.3. Optical imaging.....	11
2.3.1. Fluorescent and infrared dyes .....	12
2.4. Magnetic resonance imaging .....	17
2.5. Prussian blue nanoparticles.....	19
2. Objectives .....	20
3. Materials & Methods .....	21
3.1. Methods of nanoparticle synthesis.....	21
3.1.1. Production of uncoated Prussian Blue nanoparticles .....	21
3.1.2. Citrate coated Prussian Blue production .....	21
3.1.3. Fluorescent labelling of the particles with Eosine Y, Rhodamine B and Methylene Blue .....	21
3.1.4. PEGylation of Prussian Blue nanoparticles .....	22
3.1.5. Preparation of fluorescent Prussian Blue nanoparticle complexes with labelled IR820 dye .....	22
3.2. Methods of particle characterization in vitro .....	23
3.2.1. Dynamic light scattering (DLS) and zeta-potential measurement .....	23
3.2.2. Transmission Electron Microscopy (TEM).....	23
3.2.3. Scanning Electron Microscopy (SEM) .....	24

3.2.4. Atomic Force Microscopy (AFM) .....	24
3.2.5. Fourier Transformation Infrared Spectroscopy (FT-IR) .....	25
3.2.6. X-Ray diffraction (XRD) .....	25
3.2.7. In vitro MRI measurements .....	25
3.3. Methods for in vivo particle characterization .....	26
3.3.1. Animals .....	26
3.3.2. In vivo MRI measurements .....	26
3.3.3. In vitro Fluorescence-labeled Organism Bioimaging Instrument (FOBI) measurements .....	27
3.3.4. In vivo Fluorescence-labeled Organism Bioimaging Instrument (FOBI) measurements .....	27
3.4 Output parameters of nanoparticle characterization methods.....	27
4. Results .....	28
4.1. PEGylated, fluorescent Prussian blue nanoparticles.....	28
4.1.1. In vitro results.....	28
4.1.2. In Vivo and Ex Vivo Measurements .....	35
4.2. Prussian blue-based dual fluorescent and magnetic contrast agent .....	38
4.2.1. In vitro results.....	38
4.2.2. In vivo results .....	40
5. Discussion.....	43
5.1. PEGylated, fluorescent Prussian blue nanoparticles.....	43
5.1.1. In vitro measurements .....	43
5.1.2. In Vivo and Ex Vivo Measurements .....	47
5.2. Prussian blue-based dual fluorescent and magnetic contrast agent .....	49
5.2.1. In vitro results.....	50



5.2.2. In vivo results .....	51
6. Conclusion .....	53
6.1. Achievements.....	54
7. Summary.....	55
8. Összefoglalás (Summary in Hungarian).....	56
9. Bibliography .....	57
3 2 0 " D k d n k q i t c r j { " q h ".v.j.g."e.c.p.f.k.f.c.v.g.ø.u." 70 w d n k e c v	
I. Publications related to the topic of the Ph.D. thesis .....	70
II.. Publications not related to the top of the Ph.D. thesis .....	70
11. Acknowledgements .....	72

List of Abbreviations

AFM - Atomic force microscopy

CA - Contrast agent

CT - Computed tomography

DLS - Dynamic light scattering

DoE - Design of Experiments

ELISA - Enzyme-linked immunosorbent assay

EMA - European Medicines Agency

FDA - Food and Drug Administration

FTIR - Fourier-transformation infrared spectroscopy

HTA - High throughput screening

ICG - Indocyanine green

IR820 6 2-[2-[2-Chloro-3-[[1,3-dihydro-1,1-dimethyl-3-(4-sulfobutyl)-2H-benzo[e]indol-2-ylidene]-ethylidene]-1-cyclohexen-1-yl]-ethenyl]-1,1-dimethyl-3-(4-sulfobutyl)-1H-benzo[e]indolium hydroxide inner salt, sodium salt, New Indocyanine Green

MB - Methylene blue

MDVA - Multivariate data analysis

MRI - Magnetic resonance imaging

nDDS - Nano drug delivery systems

NIR - Near infrared

NMRI-Foxn1 - NMRI Nude Mouse

NP ó Nanoparticle

OI - Optical imaging

PAT - Process Analytica Technology

PB ó Prussian blue

PBNP - Prussian Blue nanoparticle

PBNP-MB - Methylene blue labelled Prussian blue nanoparticles

PBNP-MB@PEG3000 -

PBNP-MB@PEG6000

PBNP-MB@PEG8000

PDI ó Polydispersity index

PDSA - Plan-Do-Study-Act

PEG - Polyethylene glycol

PET - Positron emission tomography

QbD - Quality by Design

QD - Quantum dots

RES - Reticuloendothelial system

SEM - Scanning electron microscopy

SNR - Signal-to-noise ratio

SPECT - Single-photon emission computed tomography

TEM - Transmission electron microscopy

XRD - X-Ray diffraction

## 1. Introduction

The basis of the modern statistical analysis was laid in the 1920s by Sir Roland Fisher, suggesting the need of the implementation of statistical analysis not only as a final step, but as a continuous process in the scientific research. This pioneering idea have formed the approach of the current regulatory and governing framework of the pharmaceutical products of the 20<sup>th</sup> century (1). Continuing and understanding the impact of Fischer`s work, Joseph O " L w t c p " k p v t q f w e g f " v (QbD) as highlighting the need of built-in-quality into goods and services by closely detecting five critical steps: costumers and their needs must be determined, followed by product features, development reaching to the final step ó transferring it into practice and manufacturing (2). Epep " d g h q t g " L w W. E p ø u " h k p Deming has proposed a similar quality assurance system, based on theoretical knowledge, planning, testing and quality control (1). His work mainly focused on the constant improvement of quality with the help of statistical process-control and the use of Plan-Do-Study-Act (PDSA) cycles (3).

The quality and process-oriented perspective of the pharmaceutical industry helped in the early adoption of the aforementioned approaches and methods. Nevertheless, the concept of QbD has only been taken over in the beginning of the 21<sup>st</sup> century, by the biggest regulatory authorities ó the U.S. Food and Drug Administration (FDA) and the European Medicines Agency (EMA) (4). As the main statistical subpart of QbD, the Design of Experiments (DoE) only entered the chemical industry v j t g g " f g e c f g u " c h v g t agricultural implementation in the 1920s, and were influenced by the research of Box and Wilson (5).

The technological development in the computing field since the 1950s, highly contributed to the processing power increase in the field of information technology, allowing multi-thread processing of calculations, developing mathematical and statistical modelling v g e j p k s w g u 0 " V j k u " r t q e g u u k p i " r q y g t ø alsò k p h n w g p mentionable, thus allowing the observation of the critical parameters influencing the manufacturing process, and the use of Process Analytica Technology (PAT), alongside with the QbD. Nonetheless, DoE alone is not sufficient for the proper application of QbD, also multivariate data analysis (MVDA) must be considered and validated in the understanding

the designed and non-designed factors in the manufacturing process (6). The costs of the drug development have increased 1.5-fold, compared to the past century. Being a long-term process with a high rate of failure as an outcome of the development and design pipeline, out of 10 possible drug candidates only one reaches the clinical trials (7). Therefore, the need for computer aided techniques (computer-aided drug discovery), along with high throughput screening (HTS) and minimizing the unsuccessful experiments is high in this industry. However, the tools of drug development are far more sophisticated: molecular dynamics, protein interactions and routes of metabolism can be calculated, in silico assays for human organs are widely available and used. Molecular imaging methods offer cell-to-cell resolution of the biodistribution of radio- or fluorescently labelled drug candidates, in vitro and in vivo (8).

The development of fine-tuned nanocarriers and nano drug delivery systems (nDDS) have only been investigated since the late 90s, showing a strongly increasing tendency in the field of successful licensing, therapeutic efficacy and safety. The toxicology as well as the detailed examination of such novel, nano-sized materials, however, still requires extensive screening not only in computer simulations and in silico testing, but in vivo experiments too, as the most complex, multivariate system is still the living body (9).

Nevertheless, to determine possible structures, to predict interactions and labelling possibilities along with the detection of the effect on a molecular-level resolution, both instrumentation and superior computing power is crucial, which became widely available in the past decade. Several newly developed, imaging modality is already in preclinical use (10-12). These devices offer the detection of vast variety of details regarding the neuronal activation, circulation or brain imaging, with a nano-range resolution. Using the modalities aforementioned, determining the possible candidates through HTS, defining the critical parameters regarding quality with MVDA while applying PAT in every phase of the manufacturing, could lead us to real, consciously crafted, personalized diagnostics and therapy, keeping the main focus on the individual well-being and shortest recovery time possible.

## 2.1. Biomedical imaging and contrast materials

Several approaches of medical imaging are present, ranging from the simplest X-Ray screening, to more complicated techniques that utilize the emitted radio frequency that are produced by local magnetic momentum changes. Generally, images are obtained by alterations of electromagnetic waves or energies that passed through the human body during the imaging process. This procedure is facilitated by advanced computing and the captured images are handed to the clinicians. By default, medical imaging is used for diagnosis of pathological conditions, yet sometimes the contrast ratio, image quality or method used is not sufficient to provide the required data. Commonly, these shortcomings can be compensated by administering radioactive (gallium) or non-radioactive (gadolinium) materials administered into body fluids or cavities (13).

Comprehensively, the imaging method defines the required materials for the imaging. For instance, during SPECT scanning, radioactive materials are required for binding the specific regions of pathological deformities which gives a precise image of the tissue. This image combined with an anatomical modality (like CT) will provide the desired information (14, 15). However, during ultrasound imaging a well-detailed, well-targeted image is less achievable, since the imaging process only relies on the acoustic impedance changes of the tissues, giving a diffuse, anatomic overview of the body. Furthermore, the combination of ultrasound imaging with other methods is only available in the preclinical practice (16).

### 2.2.1. Radiopharmaceuticals

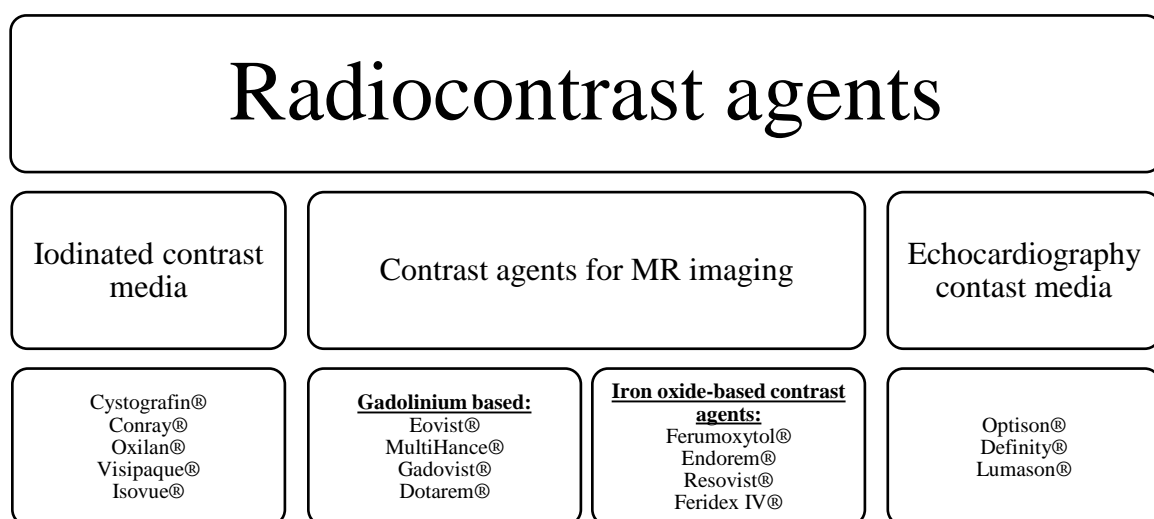
The main types of radiation emitting materials are therapeutic and diagnostic radiopharmaceuticals. While therapeutic materials are mainly focused on the destruction of malignant cells, the diagnostic radiopharmaceuticals are directly targeting specific organs, tissues or other areas of the body. Nevertheless, these materials only provide a diffuse image of the desired area, the combination of metabolic (functional) and anatomic (structural) imaging is strongly needed when they are applied (17).

### 2.2.2. Contrast agents

Contrast agents are certain materials helping with enhancing the contrast ratio or visibility of tissues, cavities or internal structures during different types of biomedical

scanning techniques (18). The main types of the radiocontrast materials are: iodinated or barium based materials, which are used for CT or X-Ray scanning; magnetic materials used for MR imaging and materials capable of altering the acoustic impedance of cavities utilized in echocardiographic imaging. To be noted, the contrast agents mentioned above are different from radiopharmaceuticals, which are used in the nuclear medicine (19-21). Table 1 summarizes the main types of contrast materials used in the clinical practice.

**Table 1.** The summary of existing contrast materials modalities, based on their use and molecular quality (13).



## 2.2. Imaging modalities

To successfully develop a CA platform, which is capable providing detailed signal enhancements during the medical examinations across multiple imaging modalities, would fill the void between the ranges of sensitivity, temporal and spatial resolution scales, and would allow the application as such in different clinical situations (22). The production of such materials would strongly rely on the computer predictions based on existing research results as input parameters; as part of the PAT, the testing of the physical properties of materials defining the critical parameters (of production and stability) for the development as well as the use of the existing instrumental background. The whole development process of materials of such would follow the outlines of the above mentioned QbD, designing materials on the existing needs, ensuring the optimal quality, safety and efficacy for the method used. The main properties of imaging modalities are summarized in Table 2.

**Table 2.** The summary of existing imaging modalities, with their main properties (23).

Modality	Signal source	Contrast	Spatial resolution	Sensitivity (moles of labelled substance)	Information	Instrument purchase price (USD)	Clinical relevance
MRI	Radio wave	Paramagnetic ( $Gd^{3+}$ ), superparamagnetic ( $Fe_3O_4$ ), endogenous (BOLD-fMRI)	10-3 2 2 "	$10^{-9} - 10^{-6}$	Anatomical, physiological, molecular	>\$300,000	Yes, wide-spread use
CT	X-Ray	$I_2$ , $BaSO_4$ , Au	50-3 2 2 "	$\sim 10^{-6}$	Anatomical, physiological	\$100,000 - \$300,000	Yes, wide-spread use
Nuclear methods (PET, SPECT)	-ray, -ray	Radioisotopes ( $^{18}F$ , $^{11}C$ , $^{13}N$ , $^{15}O$ , $^{64}Cu$ , $^{124}I$ )	1-2 mm	$10^{-15}$	Physiological, molecular	> \$300,000	Yes, wide-spread use
Optical imaging (fluorescence, bioluminescence, microscopy)	Light	Quantum dots (QD), fluorophores (VIS, NIR or IR)	@ " 2 . 5	$10^{-12}$	Physiological, molecular	\$100,000 ó \$300,000	In development

### 2.3. Optical imaging

Optical methods, offering a wide variety of observations from simple, whole-body observations to advanced tumour, metabolic pathway or fluorescent imaging or spectroscopy and microscopy methods, make them the simplest, quickest and easiest way of biomedical imaging and research. With the high spatial resolution and real-time imaging capability optical imaging (OI) methods are mainly used for ex vivo applications and image guidance as quick scout probes during surgeries or interventions (24, 25). These methods mainly use excitation followed by the detection of emission at a well-defined wavelength, despite the fact that a small portion of the irradiated intensity is lost due to thermal energy conversion and reflection. However, considering the drawbacks of OI, only a certain group of fluorophores is potentially suitable for the whole-body imaging: the optimal signal-to-noise ratio (SNR) at higher wavelengths is in the optimal range for fluorescent imaging.



Since the highly perfused tissues as well as macromolecules, e.g. collagen, muscles, skin and hair also scatter and absorb small amounts of light, resulting in autofluorescence (26-28). Nevertheless, the use of NIR light (NIR: 700-900 nm), as well as NIR emitting fluorophores for excitation and emission would greatly increase the penetration depth of OI, with a slight weakening by absorption by deoxy- and oxyhaemoglobin, melanin and collagen, with a negligible light scattering effect (29, 30).

Connecting fluorophores with chemical or physical reaction to nanoparticles, extracellular vesicles, bacteria or proteins would not only reduce the toxicity and early metabolism but would also increase the specificity and uptake to target molecules, structures or tumors as well. As Table 2. suggests, the highest sensitivity yet is available with the radioisotope techniques, the second most sensitive methods thereafter are the OI techniques, without any ionizing radiation in the imaging process involved. Considering all the drawbacks and positive properties, OI techniques offer a rational alternative as complementary methods for imaging (23, 28, 31-34).

Zeolitic nanoparticles with absorbing properties have been studied, being capable of fluorescent optical imaging, anticancer drug binding and delivery, ion and fluorescent dye absorption. During the manufacturing of such nanoparticles, besides the basic laboratory methods like centrifugal concentrating, rinsing and dialyzing, complicated steps can also be the synthesis process, making them cumbersome to reproduce or even scale-up the synthesis process to industrial level (35-38).

The use of commonly available, well-known materials and synthesis steps would greatly increase the every-day feasibility of the manufacturing of fluorescent nanomaterials.

Following this main principle, for the fluorescent labelling, Eosin Y, Rhodamine B and MB were chosen as possible candidates, whereas for the NIR labelling, based on the experience with the fluorescent dyes, we chose IR820 as a possible candidate.

### 2.3.1. Fluorescent and infrared dyes

For fluorescent imaging in living organisms, choosing proper instrumentation, methodology and fluorescent materials is essential for a satisfactory outcome. The traditional fluorescent dyes, owning strong absorption and emission peaks below 600 nm are suffering from photon reduction and autofluorescence by the living body. To overcome these, for in vivo imaging

the strong fluorescent intensity and long-wavelength emission are the primary choice. Nevertheless, nanomaterials are not only carrier systems with tunable size, shape and surface, but could also solve the previously mentioned issues, and allow the imaging in the optical window between 600-1000 nm and could also carry significantly increased amounts of fluorescent materials, compared to traditionally administered, bulk fluorescent dyes, reducing possible side effects, fluorescent bleaching and targeted in vivo imaging. Another mentionable advantage of fluorescently labelled NPs is the possibility of multimodal imaging. The tunable size, shape, surface properties and fluorescent materials allow the combination of multimodal imaging modalities, like nuclear methods and single photon emission computed tomography (SPECT) or positron emission computed tomography (PET), OI and MRI imaging (39).

### Eosin Y

Eosin Y, a xantene dye, a tetrabromo-derivate of a commonly used analytical dye, fluorescein. Besides the applications in fine arts, is often used in histological preparations as a counterdye of hematoxilin, for the Hematoxilin-Eosin staining (40, 41). The wide-spread use and the low price makes Eosine Y a reasonable candidate for fluorescent labelling.

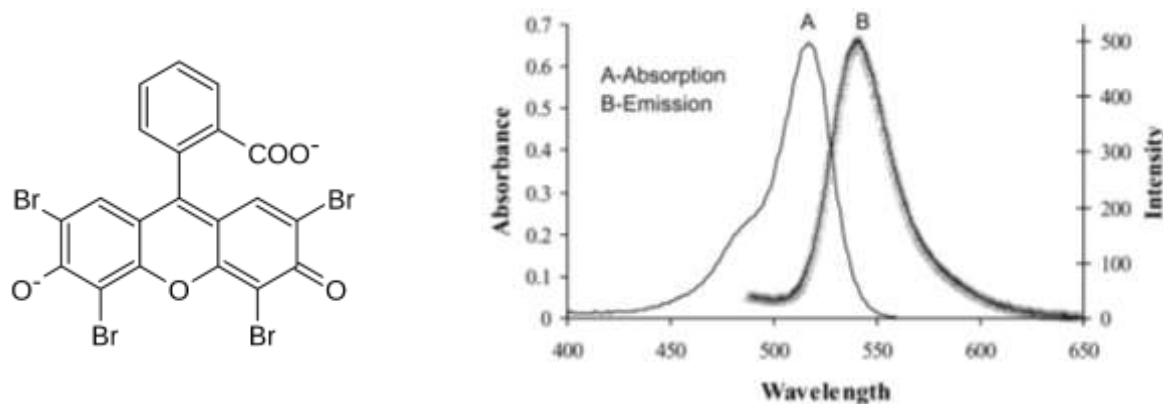


**Figure 1.** The structure, absorption and emission spectra of Eosin Y(42)

Having an excitation peak at 525 nm and an emission peak at 546 nm, 532 nm light source paired with a 575/25 nm bandpass filter would be suitable for the fluorescent imaging, however, the collagen in the skin and hair of the subjects would strongly scatter the emitted fluorescent signal, compromising the optimal SNR.

## Rhodamine B

Rhodamine B, a water-soluble inexpensive dye is often used as tracer or fluorescent dye in fluorescence microscopy, flow cytometry, ELISA and fluorescence correlation spectroscopy.

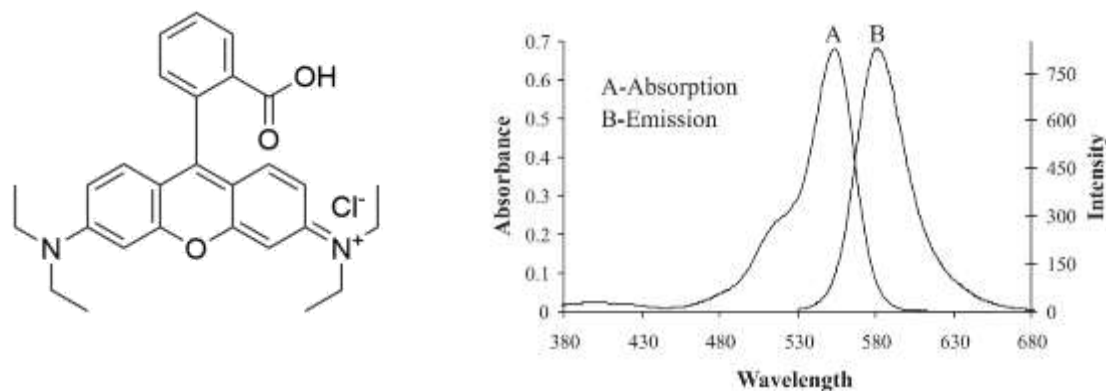


**Figure 2.** The structure, absorption and emission spectra of Rhodamine B (43)

The lactam-tautomeric structure of Rhodamine B is pH dependent; the fluorescent, open form of the spironolactone is present in acidic solutions, with a vivid, pink color (44). The excitation and emission peaks at 546 nm and 568 nm respectively place the dye's fluorescent properties closer to the desired 600 nm region. The dye is tuneable at 610 nm as a laser fluorescent probe too (45). However, regulatory bodies have labelled Rhodamine B as a potential carcinogenic compound, limiting its use in the every-day life (46).

### Methylene Blue

Methylene blue, with its excitation wavelength at 665 nm with a broad band at 610 nm and emission at 680 nm, resulting in a Stokes-shift of 21 nm, could be a potential candidate for fluorescent imaging (47).

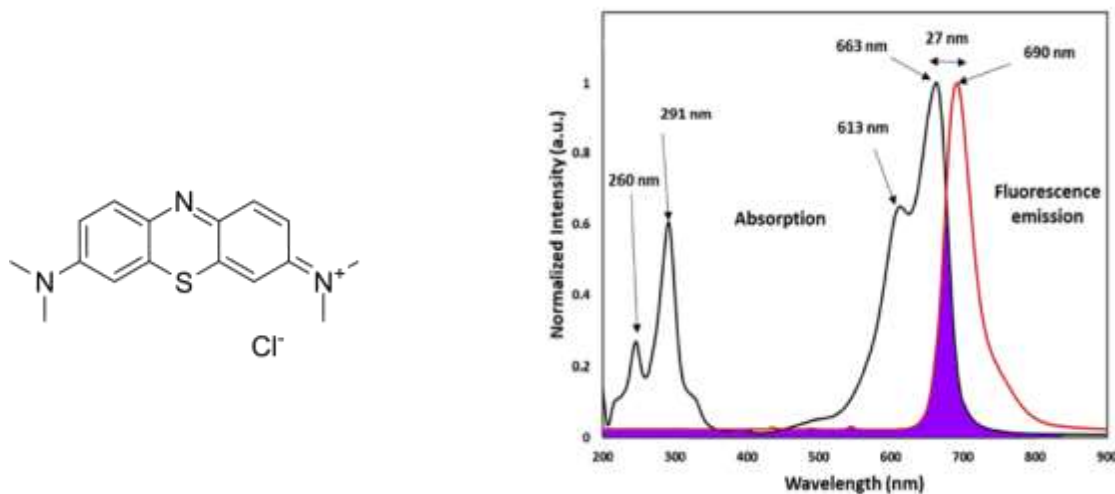


**Figure 3.** The structure, absorption and emission spectra of Methylene Blue (48)

Its emission wavelength is in the diagnostic window (650-900 nm), where the extinction coefficients of oxyhemoglobin, deoxyhemoglobin, and water are the lowest (28). Furthermore, methylene blue is on the World Health Organization List of Essential Medicines, the safest and most effective medicines needed in a health system and has been used widely in clinical and basic research (49, 50).

## IR820

As a modified version of the widely used indocyanine green (ICG), due to the IR820 has an absorption bands at 690 and 785 nm with the emission peak between 822 and 823 nm, having a slightly lower fluorescent intensity, compared to ICG (51).

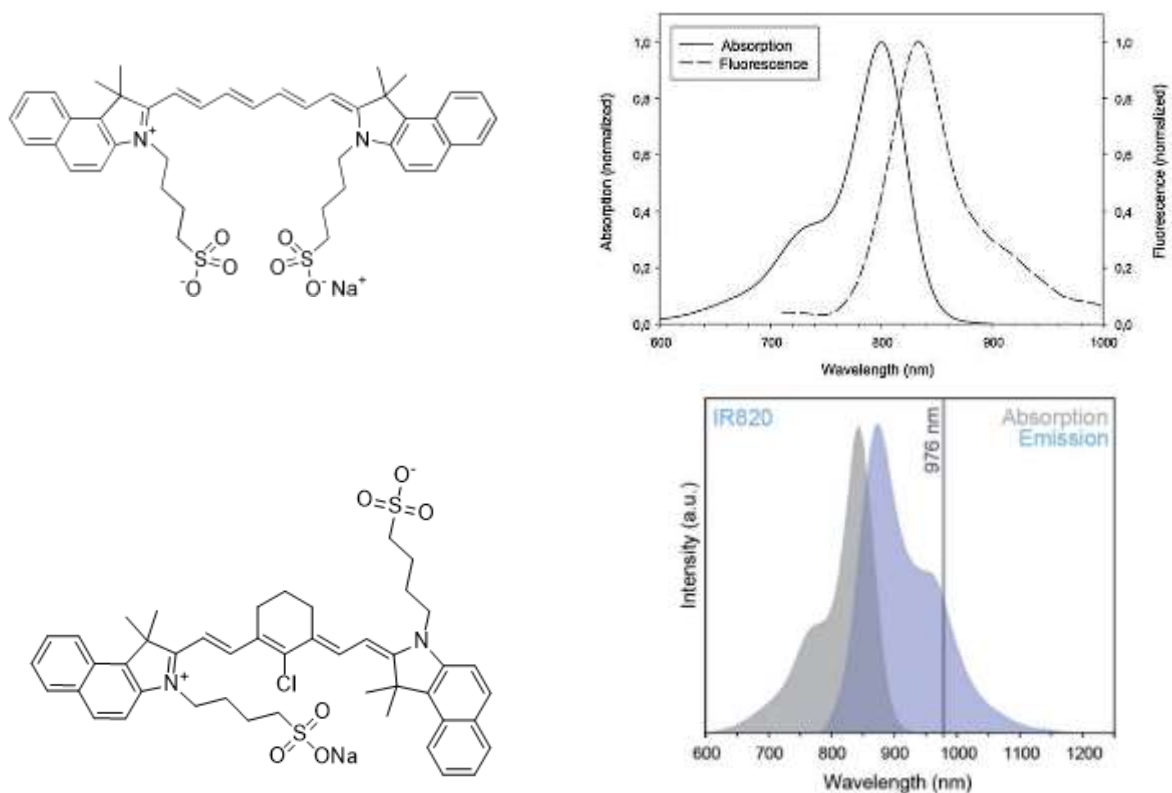


**Figure 4.** The structure, absorption and emission spectra of ICG (52) (top) and IR820 (53) (bottom)

Compared to ICG, IR-820 kept low cytotoxicity, while shows photo- and biostability in living organisms (51). Its applications cover image guided photothermal therapy for the treatment of cancer, the use as a contrasting agent for the detection and quantification of infected tissues in animals (54).

The theragnostic potential of PBNPs was proven in several studies, showing the capability of this nanosystem to adsorb metallic cations, gases, radionuclides, while owning an optimal thermal conversion capability, being considered as a potentially effective photoacoustic CA

too (36, 55-64). Functionalizing the terminal carboxylic group of the biocompatible citric acid layer on the nanoparticle surface could also widen the above mentioned theragnostic capabilities, allowing not only the long-term stabilization of the PBNPs, but also the connection of stealth-polymers, for prolonged circulation and duration of action.

#### 2.4. Magnetic resonance imaging

MRI, as a powerful imaging method for functional and morphological investigation, is a widely used whole-body diagnostic device used in the daily clinical practice. During the imaging, in most cases the intrinsic contrast of the different tissues is insufficient for the desired spatial resolution, thus requiring the application of a variety of extrinsic (injected) CAs. As their mode of action, these materials change local tissue relaxation, resulting in the shortening of transverse ( $T_2/T_2^*$ ; negative contrast) or the longitudinal ( $T_1$ ; positive contrast) relaxation times of water, resulting in hypo (negative contrast; local darkening)- or hyperintense (positive contrast; local brightening) changes on the captured images (65, 66).

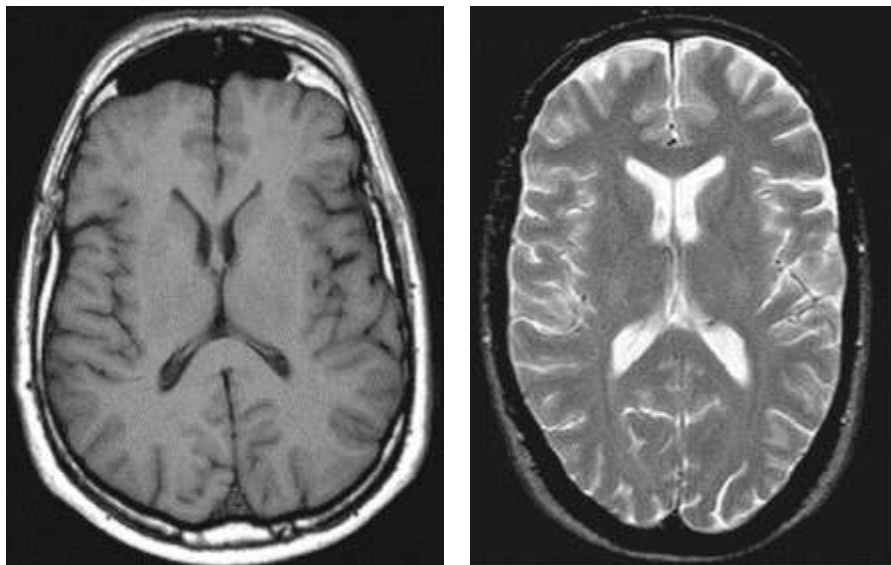


**Figure 5.** The comparison of MRI image contrasts. T1 weighted (left) and T2 weighted (right) MRI axial image of the human brain (67).

Iron containing MRI active materials and nanoparticles as CAs have been studied extensively, for their known  $T_2/T_2^*$  shortening properties in the past decades (68-70). In their case,  $T_2/T_2^*$  shortening can be interpreted as high  $r_2$  (transverse) relaxation time,

producing negative contrast on MRI images, however, this can only be hardly differentiated from other blood or calcium-rich areas of interest. Nevertheless, in the clinical practice, the detection of darkening on the screen is less convenient and harder to differentiate, than the detection of bright spots, which would appear in the case of T1 CAs. Understanding the drawbacks, the limited research and clinical application of iron containing CAs is understandable, enhancing the development of positive T1 CAs for MRI imaging (71-73).

As the main candidate, Gadolinium (III) and its complexes and derivatives offered a reasonable option as ideal T1 CAs in the early 2000s, causing hyperintense changes on MRI scans while providing optimal spatial and temporal resolution (74-76).

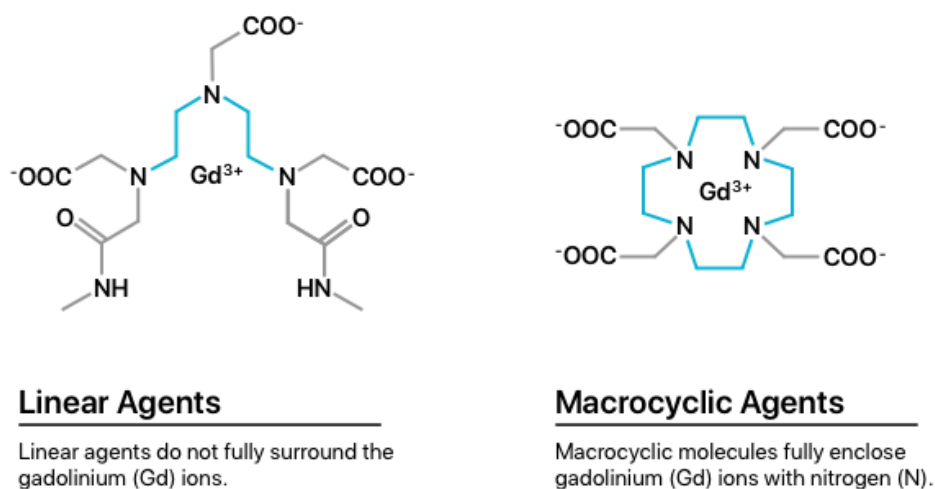


**Figure 6.** Linear and macrocyclic Gadolinium-based contrast agents (77).

Due to possible harmful side-effects of the linear-agent-bound Gd containing CA, in the declaration of European Medicines Agency (EMA; EMA/625317/2017) dated 19 December 2017, all drugs have been removed from the market in the second quarter of 2018. In the pronouncement, possible neurotoxic effects due to accumulation in the central nervous system (mainly in the brain) were reported, as leading to a possible conclusion to the macrocyclic CAs, having adverse effects as well. The lifeline of Gd-connected molecules after the EMA declaration is clear; recent authorizations as well as ongoing trials could be cancelled.

For this reason, iron-based nanomaterials for positive MRI contrast have been extensively investigated (78). Their magnetic core-shell structure allows biocompatible layers for modifications, customizing surface charge, thus stability, whereas their tuneable size allows to customize the MR contrast property. As part of the QbD, their final properties, namely the highly variable size, superparamagnetic MR-active property, biocompatibility and physical stability make iron-based nanomaterials one of the frequently studied substance for medical use (66).

## 2.5. Prussian blue nanoparticles

Among the nano-sized iron-based CA, PBNPs are a reasonable candidate as T1 MRI CAs. They have been known and studied for a variety of electrochemical, biomedical and contrast application, and have been used for nearly 300 years (79, 80).

The FDA has authorized and released a PBNP-based medication (Radiogardase®), in 2003, for human use, to treat heavy metal poisoning, using PBNP's unique metal complexing property (81). To fabricate them, direct or indirect synthesis methods can be applied, obtaining PBNPs of different shapes, sizes, and other parameters, depending on the method used (82-84). Biocompatible layer can be also added, using polymers, organic acids, enhancing the stability and half-life of circulation in living organisms (56, 85). Citric acid, the most widely used biocompatible shell material not only affects the particle size and shape depending on its concentration, but also plays a substantial role regulating the pH in the PBNP synthesis (86). Nevertheless, non-functionalized PBNPs show less significant T1 and T2 signal changes in vitro; their measured longitudinal and transversal relaxation times did not suggest their in vivo use. However, not only the functional groups and particle size influence the contrast capability, the marginal water near the CA's molecules also have significant effect in the contrast-enhancement (87). Therefore, functionalizing PBNPs, to achieve multimodal contrast would highly increase their impact for preclinical applications, thus in the routine procedures MRI is oftentimes coupled with other modalities providing greater functional contrast.



## 2. Objectives

Our studies were focused on creating a multimodal platform with fluorescent labelling of PBNPs with commonly used dye-candidates, with the following aims:

- I. To create a nanoparticle platform, with quality requirements as follows:
  - a stable nanosystem, which does not aggregate over 8 weeks of examination period;
  - the emission of a fluorescent signal that could be detected in living organisms to make the particle suitable for in vivo imaging;
  - a clearance mechanism to reduce possible side effects but also to slow down accumulation in the monocyte-macrophage system.
- II. To create a fluorescently labeled Prussian blue nanoparticle (PBNP) based nanosystem for preclinical fluorescent imaging;
- III. To also take advantage of the biocompatible coating of the particle, thus connecting the potential fluorescent dyes and stabilizers to PBNPs
- IV. To investigate the fluorescent imaging capabilities of the successfully labelled PBNP in a model system over 3 hours, in clinically relevant, translational study.

Furthermore, based on the obtained knowledge on the fluorescent labelling of PBNPs, we aimed to enhance the multimodal relevance of the PBNP platform, by aiming:

- V. To develop and characterize a Prussian Blue based biocompatible and chemically stable T1 magnetic resonance imaging (MRI) contrast agent with near infrared (NIR) optical contrast for preclinical application.
  - As part of the in vivo studies, investigating the physical properties of beforementioned nanoparticulate system by DLS, Zeta-potential measurements, AFM and TEM as well as the MRI contrast enhancement capabilities
- VI. To investigate the T1-weighted contrast of the prepared PBNPs in vivo, furthermore,
- VII. To measure the NIR fluorescence of the samples with optical imaging modality after intravenous administration into NMRI-Foxn1 nu/nu mice.

### 3. Materials & Methods

#### 3.1. Methods of nanoparticle synthesis

##### 3.1.1. Production of uncoated Prussian Blue nanoparticles

Native PBNPs were synthesized according to as described by Shokouhimehr [37], with modifications. As first step, the reactant solutions were prepared with Solution A containing 20 mL of 1.0 mM Fe(III) chloride anhydrous ( $\text{FeCl}_3$ ; Merck KGaA, Darmstadt, Germany) with 6 drops of 1 N HCl (Merck KGaA), while Solution B containing 20 mL of 1.0 mM potassium ferrocyanide anhydrous ( $\text{K}_4[\text{Fe}(\text{CN})_6]$ ; Merck KGaA, Darmstadt, Germany) with 6 drops of 1 N HCl (Merck KGaA). Secondly, these solutions were mixed slowly under vigorous stirring for 10 min at 60 °C (88).

##### 3.1.2. Citrate coated Prussian Blue production

Citrate-coated PBNPs were produced with the process as described by Shokouhimehr [37]. A two-step PBNP preparation was made. Reactant solutions were made first, Solution A containing 20 mL of 1.0 mM Fe(Fe (III) chloride anhydrous ( $\text{FeCl}_3$ ; Merck KGaA, Darmstadt, Germany) with 0.5 mmol of citric acid (Merck KGaA), while Solution B contained 20 mL of 1.0 mM anhydrous potassium ferrocyanide ( $\text{K}_4[\text{Fe}(\text{CN})_6]$ ; Merck KGaA, Darmstadt, Germany) with 0.5 mmol citric acid (Merck KGaA) solution. Next, these solutions were mixed using fast stirring for 10 min at 60 °C (89).

##### 3.1.3. Fluorescent labelling of the particles with Eosine Y, Rhodamine B and Methylene Blue

Eosin Y and Rhodamine B were adsorbed to the particles. For fluorescent labelling, the concentrated methylene blue (MB; Sigma-Aldrich) stock solution was diluted twofold and filtered through a 0.22  $\mu\text{m}$  pore size membrane filter (MILLEX GP 0.22  $\mu\text{m}$ ; Merck Millipore Ltd.). Further, 200  $\mu\text{L}$  of this filtered solution was added to 2 mL of the PBNP solution. This would result in absorbed MB on the mesoporous surface of the biocompatible PBNPs. After that, two main approaches were made:

- a.  $\text{V j g " u \{ p v j g u k | g f " R D P R u " y g t g " n c d g n n g f " c h v g t}$  using 21,130 rcf (Eppendorf 5424R centrifuge). Thereafter, the PEGylation process was performed and the solution was dialyzed against phosphate buffer saline solution (pH = 6.8; Ph.Eur. 8.).

b. The PBNP-MB mixture was centrifuged at 21,130 rcf (Eppendorf 5424R centrifuge) at 4 °C. Then, the PBNP-MBs were PEGylated, dialyzed, and stored at 268 °C until further use (89).

#### 3.1.4. PEGylation of Prussian Blue nanoparticles

For the PEGylation, PEG 3000 (for molecular biology; Sigma Aldrich Germany) was available in monodisperse solution, while PEG 6000 (for synthesis; USP) and PEG 8000 (for synthesis; USP) (Sigma Aldrich, Hungary) were commercially sold in solid form. At first, these power-based agents were dissolved in 50% ethanol/water mixture the final PEG content was set to 10 w/w%. PBNP-MB solutions (2 mg/mL) were prepared by adding distilled water (Milli-Q) to the stock MB-labelled PBNP solution. After 15 min incubation time at room temperature, different PEG solutions (PEG 3000, PEG 6000, and PEG 8000) were added to the PBNP-O D " u q n w v k q p u " c p f " f k c n { | g A l d r i c h , q t " 4 6 " j Hungary) in phosphate buffer saline solution (pH = 6.8; Ph.Eur. 8.). Different v/v% concentration compositions (PEG 3000: 1.47-1.96-2.44-3.85-9.09, PEG 6000: 1.47-1.96-2.44-3.85, and PEG 8000: 1.47-1.96-2.44) were prepared and characterized in the following with DLS and Zetasizer instruments (89).

#### 3.1.5. Preparation of fluorescent Prussian Blue nanoparticle complexes with labelled IR820 dye

Following the coated and uncoated particle syntheses, the two different types of PBNPs were mixed under vigorous stirring for 10 min at 60 °C. With 10 minutes passed, 5 g Chelex (chelating ion exchange resin, Merck KGaA, Darmstadt, Germany)/100 mL solution was applied to eliminate the superfluous metal or alkali metal ions from the system [38]. This suspension was stirred and incubated for one hour, whereby the styrene divinylbenzene copolymer beads were separated from the PBNP solution. In the next step, PBNPs were isolated from the complex suspension using ultracentrifugation (Eppendorf 5424R centrifuge, 21130 rcf) at 4 °C for 30 min.

A batch of uncoated PBNPs and fluorescent PBNP complexes were also produced, using the same method with a slight modification. Subsequently the production of reaction solutions of uncoated and complex PBNPs, an additional step of differential velocity centrifugation in

the synthesis was included. The reaction of uncoated PBNP solutions were sedimented (Eppendorf 5424R centrifuge) 2 times at 1000 rcf and 2 times at 2000 rcf for 10 minutes consecutively. The PBNP complexes were centrifuged (Eppendorf 5424R centrifuge) 2 times at 2000 rcf for 10 minutes; one batch was filtered through a 0.22  $\mu\text{m}$  pore size membrane filter (MILLEX GP 0.22  $\mu\text{m}$ ; Merck KGaA, Darmstadt, Germany) and centrifuged at 2000 rcf for 10 minutes. As a final step, we isolated the particles by ultracentrifugation (Eppendorf 5424R centrifuge, 21130 rcf) at 4 °C for 30 minutes. To achieve fluorescence in the PBNPs, 0.1 mg/mL IR820 NIR dye was filtered through a 0.22  $\mu\text{m}$  pore size membrane filter (MILLEX GP 0.22  $\mu\text{m}$ ; Merck KGaA, Darmstadt, Germany). 10  $\mu\text{L}$  of this filtered dye solution was adsorbed to the particles in 300  $\mu\text{L}$  PBNP solution for a one-hour incubation (88).

### 3.2. Methods of particle characterization in vitro

#### 3.2.1. Dynamic light scattering (DLS) and zeta-potential measurement

The surface charge and hydrodynamic diameter of the particles were determined using a Malvern Nano ZS (Malvern Instruments Ltd., Worcestershire, UK) and Litesizer 500 (Anton Paar, Hamburg, Germany.). DLS measurement was performed at 25 °C in automatic mode (for backscatter detector fixed at 175°; for side scatter 90° detector angle; for front scatter 15° detector angle) using a 633 nm He-Ne laser. Samples were measured in Omega cuvettes (Anton Paar, Hamburg, Germany). Measurement of zeta-potential was performed under similar conditions. The measurement data were evaluated using software provided by the manufacturer, and statistical data and graphs were created and evaluated with Origin 9.0 (OriginLab), Microsoft Excel 2013 and the built-in software. DLS measurements were performed weekly for a period of 4 weeks to determine colloidal stability. Samples were stored at 4 °C (88, 89).

#### 3.2.2. Transmission Electron Microscopy (TEM)

Morphological investigations of the NPs were carried out on a JEOL TEM 1011 TEM (JEOL, Peabody, MA, USA) operated at 80 kV. The camera used for image acquisition was a Morada TEM 11 MPixel from Olympus (Olympus, Tokyo, Japan) using iTEM5.1 software for metadata analysis. Diluted sample was dropped and dried on a carbon-coated copper grid.

Size distribution was determined manually by measuring the diameter of 1059 particles on the images, using a software custom designed for this purpose (tem\_circlefind by András Wacha, MTA TTK, Hungary). Morphological investigations of the NPs were carried out on a MORGAGNI 268(D) (FEI, Eindhoven, Netherlands) transmission electron microscope. The diluted sample was dropped and dried on a carbon-coated copper grid. The length (along multiple axes) and the area of the particles were determined manually by measuring the diameter ( $n = 195$ ) and circumference ( $n = 207$ ) of the nanoparticles, using ImageJ software (88, 89).

### 3.2.3. Scanning Electron Microscopy (SEM)

The nanoparticle suspension was diluted with distilled water (1:2) and applied to a metallic sample plate, which was covered with a double-sided carbon tape. The sample was dried under vacuum, metallized with gold and investigated with a field emission EM, JEOL JSM 6380LA SEM (Jeol Ltd., Japan), at 15 kV and a working distance of 15 mm. The morphology of the nanoparticles was observed (88, 89).

### 3.2.4. Atomic Force Microscopy (AFM)

For imaging PBNP complexes, two-fold diluted samples were applied onto poly-L-lysine (PLL)-coated surfaces. PLL (0.1% w/v) onto freshly cleaved mica, followed by incubation for 20 min, repeated rinsing with purified water, and drying with a stream of high-purity nitrogen gas. After a 30 min incubation, AFM images were collected in noncontact mode with a Cypher S instrument (Asylum Research, Santa Barbara, CA, USA) in air, using a silicon cantilever (OMCL AC-160TS, Olympus, Tokyo, Japan) oscillated at its resonance frequency (300.65 kHz) with a 10 mV peak-to-peak amplitude. The scanning rate was 1 Hz. The temperature of the measurements was  $25 \pm 1$  °C. AFM amplitude-contrast images are shown in this paper. The filter used on the images enhances the details of the height amplitude contrast images (violet, orange, yellow, red). AFM images were analyzed by using the built-in algorithms of the AFM driver software (Igor Pro, Wave Metrics Inc., Lake Oswego, OR, USA). Particle statistics was done by analyzing the contrast image with a particle analysis software. Maximum height values were taken as the height of particles, and rectangularity was

calculated as the ratio of the particle area to the area of a nonrotated inscribing rectangle. The closer a particle is to a rectangle, the closer this value is to unity (88, 89).

### 3.2.5. Fourier Transformation Infrared Spectroscopy (FT-IR)

The infrared spectra were recorded with a Bruker Vertex80v (Bruker Optics, Billerica, MA) FTIR spectrometer equipped with a high sensitivity MCT (mercury-cadmium-telluride) detector. Each spectrum was collected averaging 128 scans at  $2 \text{ cm}^{-1}$  resolution. The infrared beam was focused on a high-pressure diamond anvil cell (Diacell, Leichester, UK) using a Bruker A525 type beam condenser.

Two main measurement methods were used:

- 72 " N " q h " v j g " w p f k n w v g f " u w u r g p u k q p u " q h " v j g " compressed air. The measurements were executed under  $\text{N}_2$  atmosphere, to eliminate external humidity and water condensation at the detector (Figure 9/I).

Then, the samples were lyophilized, then the completely dry samples were measured in the diamond anvil cell (Figure 9/II):

- Freeze-dried samples were resolved in  $\text{D}_2\text{O}$  " \* 4 2 " N + " c q t l f e " d e t e c t o r u s i n g f t k g f " v compressed air. The measurements were executed under  $\text{N}_2$  atmosphere, to eliminate external humidity and water condensation at the detector (89).

### 3.2.6. X-Ray diffraction (XRD)

3 2 2 2 " N " q h " v j g " w p f k n w v g f " u w u r g - d i f f r a c t i o n p l a t e q h " v j g " (Silicon crystal cut with special orientation in order to eliminate background noise), using infrared light. X-ray diffractograms were recorded by Philips PW 1810/1870 diffractometer c r r n { k p i " o q p q e j t q o c v k | g f " E w M " t c f k c v k q p " \* 6 2 " u v g r " u k | g " q h " 2 0 2 6 \text{Å} . " - 5 0 \text{°} . The evaluation of the diffractograms " q h " 4 " was carried out using Origin 9.0 (OriginLab) (89).

### 3.2.7. In vitro MRI measurements

MRI measurements were performed in vitro with a nanoScan® PET/MR system (Mediso, Hungary), having a 1 T permanent magnetic field, 450 mT/m gradient system using a volume

transmit/receive coil with a diameter of 60 mm. MRI T1 relaxation rates and  $r_1$  relaxivity were calculated from inversion prepared snapshot gradient echo (T1 map, IR GRE SNAP 2D) images acquired with 60 x 90 mm FOV (field of view), plane resolution of 1 mm, slice thickness of 5 mm, 6 averages, TR/TE 4005/1.7, TI 10, 60, 100, 150, 200, 250, 300, 350, 400, 500, 700, 900, 1200, 2500, 4000 ms. MRI-signal enhancement of PBNPs was measured for three different Fe(Fe (III)) concentrations (13.75 mM, 41.25 mM, and 82.5 mM) in 1.5 mL Eppendorf tubes. After scanning, the concentration dependent signal changes were calculated and compared to the signal of saline (88, 89).

### 3.3. Methods for in vivo particle characterization

#### 3.3.1. Animals

In vivo imaging tests of the PBNP nano systems were carried out in NMRI FOXN nu/nu male mice (Janvier, France). Animals had ad libitum access to food and water and were housed under temperature-, humidity-, and light-controlled conditions. All procedures were conducted in accordance with the ARRIVE guidelines and the guidelines set by the European Communities Council Directive (86/609 EEC) and approved by the Animal Care and Use Committee of Semmelweis University (protocol number: PE/EA/1468-8/2019). Mice were kept under anesthesia using a mixture of 2.5% isoflurane gas and medical oxygen. Their body temperature was maintained at 37 °C throughout imaging. For the most humane termination of the animals, intravenous Euthasol (pentobarbital/phenytoin) injection was used (88, 89).

#### 3.3.2. In vivo MRI measurements

In vivo measurements were performed similarly as in vitro MRI measurements, with the same instrument and settings, described in chapter 4.2.7.. Experiments were performed in an adult male mouse under isoflurane anesthesia (5% for induction and 1.562% to maintain the appropriate level of anesthesia; Baxter, Arrane). Precisely, 300  $\mu$ L of IR820-labelled PBNP solution containing 3 mg of Fe(Fe (III)) in a 30 mg/mL concentration PBNP solution was administered intravenously into the tail. The T1-weighted MRI biodistribution images were collected at two different time points (pre- and post-injection) The MRI scans were performed with gradient echo (T1 GRE 3D) images acquired with 100 mm x 40 mm FOV,

matrix size 200 x 80, slice thickness of 0.5 mm, 4 averages, TR/TE 75/4, dwell time 25 ms. Images were further analyzed with Fusion (Mediso Ltd., Hungary) and VivoQuant (inviCRO LLC, US) dedicated image analysis software, for fluorescent images as well (88, 89).

### 3.3.3. In vitro Fluorescence-labeled Organism Bioimaging Instrument (FOBI) measurements

The fluorescent labelled PBNPs were imaged using a two-dimensional epifluorescent optical imaging instrument (FOBI, Neoscience Co. Ltd., Suwon-si, Korea). For in vitro scans, 0.5 mL of samples were tested with the following imaging parameters: excitation at 680 nm corresponding to the excitation maximum of the dye (excitation: 690 nm; emission: 820 nm), exposure time: 1000 msec and gain: 1. The emission spectrum of the dye was in the pass band of the used emission filter.

### 3.3.4. In vivo Fluorescence-labeled Organism Bioimaging Instrument (FOBI) measurements

In vivo experiments were performed in an adult male mouse under isoflurane anesthesia (5% for induction and 1.562% to maintain the appropriate level of anesthesia; Baxter, Arrane). Precisely, 300  $\mu$ L of IR820-labelled PBNP solution was administered intravenously into the tail vein. The biodistribution images were collected at two different time points (pre- and post the injection) with excitation of 680 nm corresponding to the excitation maximum of the dye (excitation: 690 nm; emission: 820 nm). The emission spectrum of the dye was in the pass band of the used emission filter. Image acquisition parameters were the following: exposure time: 1000 msec and gain: 1 (88, 89).

## 3.4 Output parameters of nanoparticle characterization methods

Many articles investigated the differences between the possible methods used for characterization of nano-sized objects, nanosuspensions and nanoparticles. Even though in the fields of materials science and chemical engineering, there is a strong need for different types of measurements of the same materials, however the interpretation and the proper understanding of each method is needed to achieve the desired goals. The most frequently used methods to describe a nano system are the DLS, the AFM and the TEM. These methods differ from each other regarding the mathematical basics, sensitivity and robustness. Therefore, a direct comparison is unattainable, hence in most studies, not only one size-range, but a size distribution in form of either a histogram or figure is found (90-92).



## 4. Results

### 4.1. PEGylated, fluorescent Prussian blue nanoparticles

Multiple approaches were made to determine the optimal PEG coating concentration. For that, different volume-percent compositions were formed and characterized. During the preformulation, DLS measurements were performed and combined with the macroscopic analysis of the samples (aggregation, visual evaluation, homogeneity, and homogenizability). We found that the optimal PEG concentration for the different types of PEG solutions is slightly different if the particle size and the PDI are the form factors for choice. For further inspections, PBNP-O D " u c o r n g u " e q p v c k p k p i " 7 " o i -" \* 3 2 " O D B R G I 5 2 2 2 a 3 2 N + . " 3 2 " o i " \* O D B R G I 5 2 2 2 a 3 2 N + . " 3 2 " o i " \* 12.5 mg (3 2 2 " N + " R G I " O : D B R G I \* R P D R 3 2 2 N + " y g t g " e j q u measurements and macroscopic inspections. The other samples showed either aggregation during the measurements or sedimented despite the optimal hydrodynamic diameter and low PDI value. The synthesized methylene-blue-labelled PEGylated PBNP-s (PBNP-MB@PEG) were stored at 268 °C.

Thus, not all samples were amenable to fluorescent imaging in vivo, furthermore, they lacked stability during the early inspections. The aggregation of the nanosystem along with fluorescent dye wash-off was noted.

Fluorescein labelling of PBNPs was not successful. Experimenting with other dyes we found that Rhodamine B, Eosine Y and Methylene blue sorption to PBNPs was feasible. However, Rhodamine B labelled PBNPs lacked stability: immediately after labelling, aggregation was visible. The long-term stability of Eosine Y and MB labelled PBNPs and their in vivo imaging signalling performance was thus further investigated.

#### 4.1.1. In vitro results

##### Atomic Force Microscopy

AFM images are shown in Figure 7. Rectangularity of the particles (together with their halo) was found to be  $0.7701 \pm 0.1041$  (mean  $\pm$  SD), indicating that PBNPs indeed represent rectangular topography. The height of the particles showed monomodal distribution with a mean  $\pm$  SD of  $17.790 \pm 0 ; 4 4 p \sigma$ " \* H k i w t g "

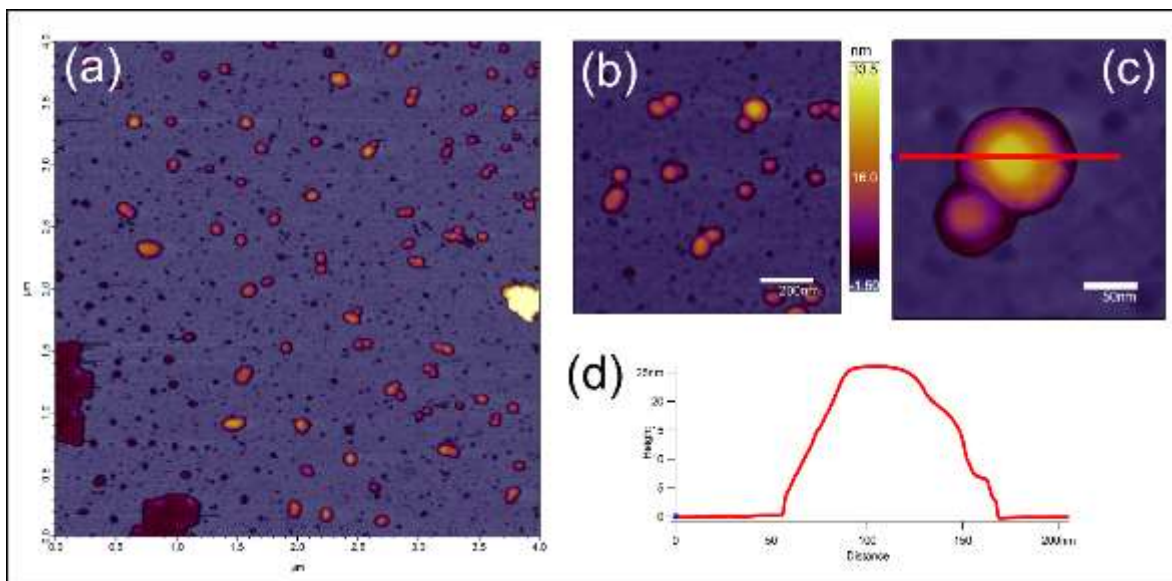


**Figure 7.** (a) Height-contrast AFM image of PBNPs on the mica surface (scale bar =  $4 \mu\text{m} \times 4 \mu\text{m}$ ). (b) Modified PBNPs on the mica surface; height-contrast AFM image (scale bar = 200 nm). (c) A modified PBNP nanoparticle (scale bar = 50 nm). (d) The cross-section graph of (c) PBNP nanoparticle (abscissa = 06200 nm; ordinate = 0625 nm).

#### Scanning Electron Microscopy (SEM) and Transmission Electron Microscopy (TEM)

Single particles were hard to distinguish from one another, however, their size did not exceed the 100 nm threshold (Figure 8a). The nonhydrated shape and size of the NPs were also analyzed with TEM (Figure 8b,c). The nanosystem was slightly aggregated (Figure 8c), however, single particles could be observed. The shape of the nanoparticles on TEM and AFM images was similar. PBNPs appeared as flat rectangular, dense objects in this case as well. The average length of the particles was  $28.080 \pm 6.690 \text{ nm}$  (mean  $\pm$  SD;  $n = 304$ ) (Figure 8d), along with an average surface area of  $582.20 \pm 269.750 \text{ nm}^2$  (mean  $\pm$  SD;  $n = 176$  particles) (Figure 8e).

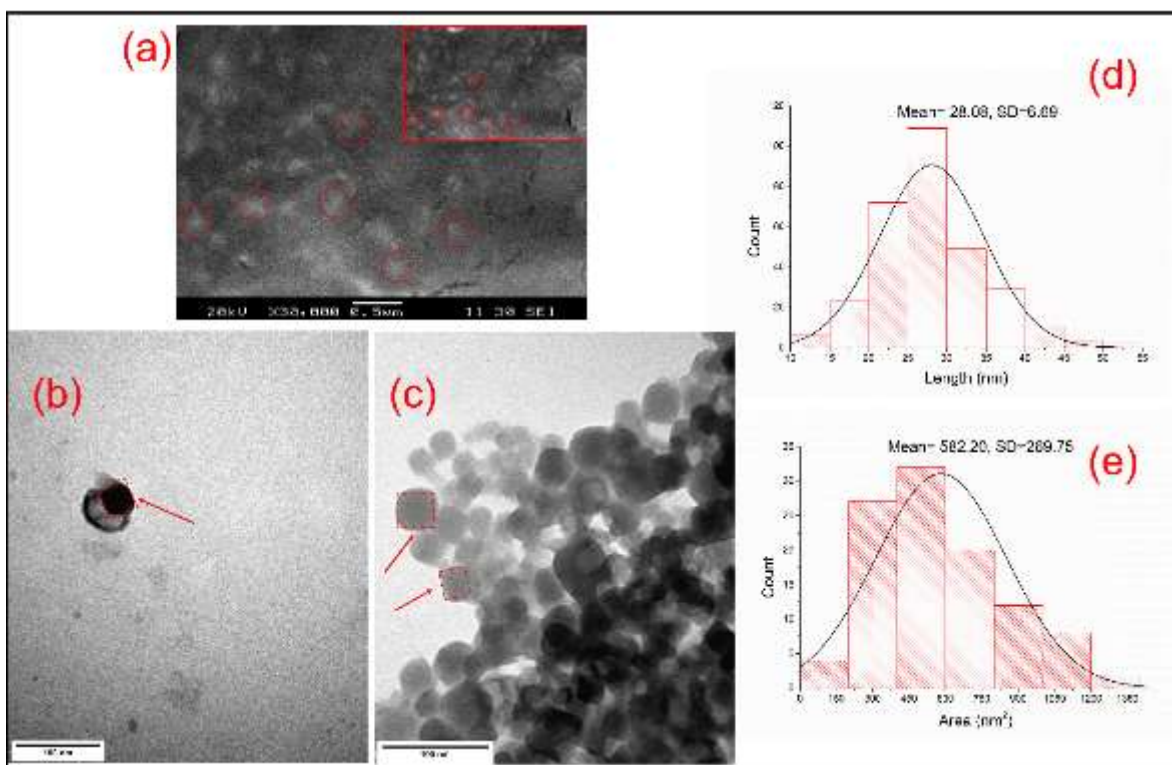


**Figure 8.** (a) The SEM micrograph of modified PBNPs (magnification: 30,000x, scale bar = 0.5  $\mu\text{m}$ ); the PBNPs are barely visible between the pores of the double-sided carbon tape (section of (a); magnification: 30,000 $\times$ ). (b)(c) The TEM micrograph of modified PBNPs (magnification = 250,000x; scale bar = 100 nm). (d) The mean length of PBNPs, determined by TEM images. (e) The average area of the modified PBNPs according to TEM images.

#### Fourier Transformation Infrared Spectroscopy (FT-IR)

Two main measurement methods were used: First, 7 2 " N " q h " v j g " w p f k n w v g f " u samples were dried to the detector, using compressed air. The measurements were executed under  $\text{N}_2$  atmosphere, to eliminate external humidity and water condensation at the detector (Figure 9/I).

Then, the samples were lyophilized, then the completely dry samples were measured in the diamond anvil cell (Figure 9/II). Second, the freeze-dried samples were resolved in  $\text{D}_2\text{O}$  (20

N + " c p f " v j g p " f t k g f " v q " v j g " f g v g e v q t . " w u k p i " e q under  $\text{N}_2$  atmosphere, to eliminate external humidity and water condensation at the detector (89).

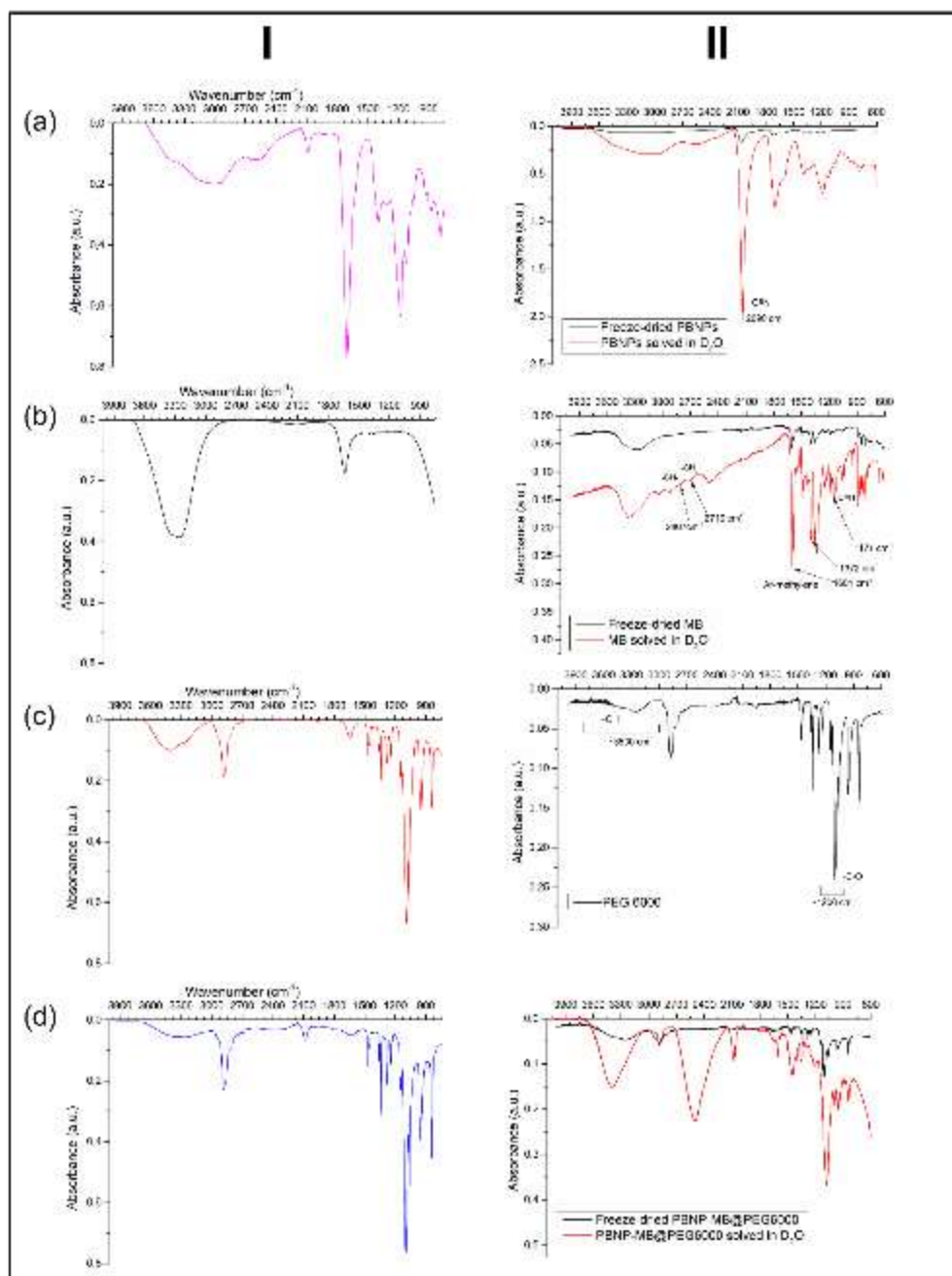


**Figure 9. I - FTIR measurement of PBNP solutions**(a) FT-IR spectra of unmodified PBNP (mid-IR region = 4,000-750  $\text{cm}^{-1}$ ). (b) FT-IR spectra of Methylene blue (mid-IR region = 4,000-750  $\text{cm}^{-1}$ ). (c) FT-IR spectra of PEG 6000 (mid-IR region = 4,000-750  $\text{cm}^{-1}$ ). (d) FT-IR spectra of pegylated, fluorescent PBNPs (mid-IR region = 4,000-750  $\text{cm}^{-1}$ ).

**Figure 9.** FTIR measurement of freeze dried PBNP solutions (a) the FT-IR spectra of unmodified PBNPs. (b) FT-IR spectra of Methylene blue. (c) FTIR spectra of PEG 6000. (d) FT-IR spectra of pegylated, fluorescent PBNPs.

#### X-Ray diffraction (XRD)

The two samples ((a) Prussian blue reference solution, which was used later for pegylation and methylene blue labelling and (b) pegylated, fluorescent labelled PBNPs) were measured.

The spectra (Fig. 10) which can be allocated to the Prussian blue phase crystal planes respectively.

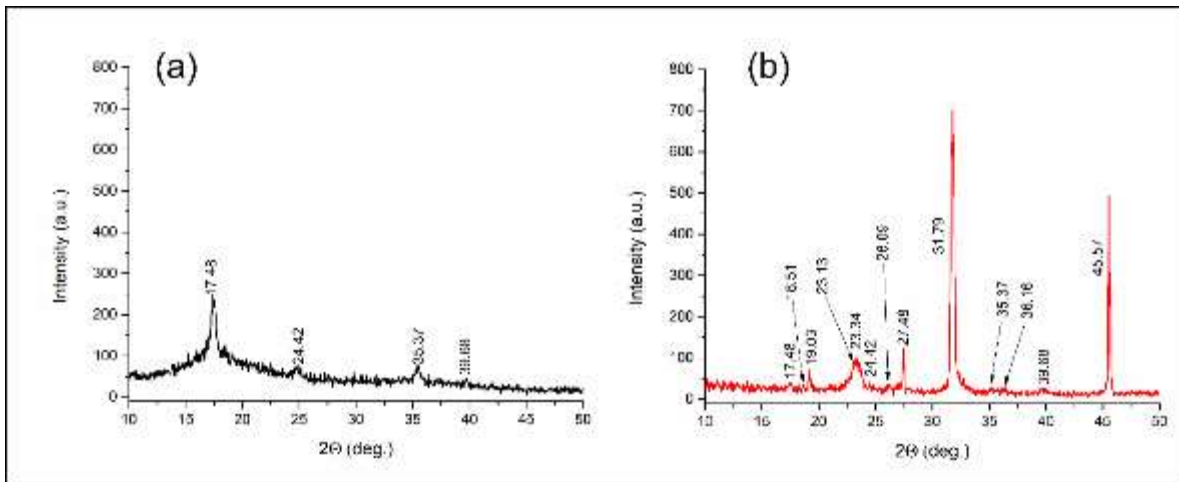


**Figure 10.** (a) The XRD diagram of the unmodified PBNPs. (b) The XRD diagram of the modified PBNPs. XRD: X-ray diffraction; PBNPs: Prussian Blue nanoparticles.

#### Measuring In Vitro Fluorescence

After the two main approaches of fluorescent labelling, PBNP-MB@PEGs were tested in vitro, to study whether the emitted signal is adequate for in vivo imaging. For that purpose, 20-fold diluted samples were produced and measured, along with the stock PBNP-MB@PEG solutions. The samples prepared according to method a showed lower intensity on the emitted light, on the other hand, method b provided a significantly better signal in emission, which made the sample a better choice for in vivo use (Figure 11a,b).

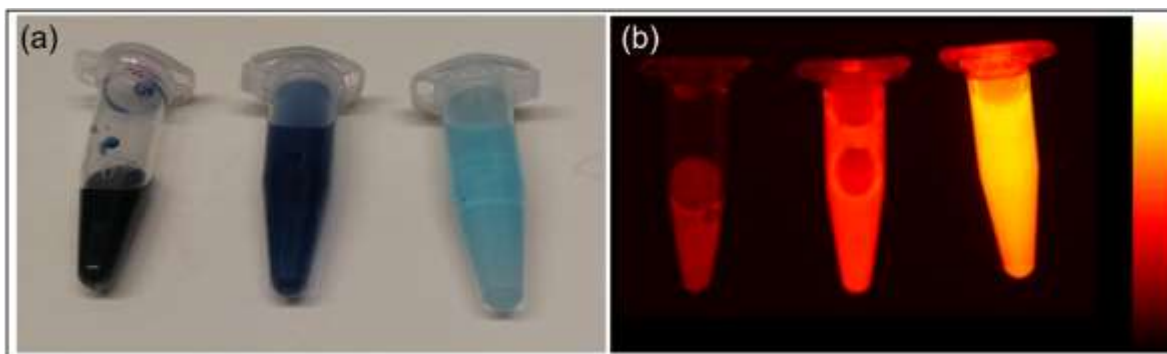


**Figure 11.** (a) PBNP-MB@PEG6000\_100µL (stock solution, 5× and 20× dilution left to right). (b) Fluorescent signal of PBNP-MB@PEG6000\_100µL dilutions in FOBI.

#### Stability Measurements of PBNP-MB@PEG Nanoparticles

The mean zeta potential of the measured samples (PBNP, PBNP-MB@PEG3000, PBNP-MB@PEG6000, and PBNP-O D B R G I : 2 2 2 + " y c u " p q v " d k i i g t " v j c p " samples had a net negative potential q h " 4 7 " o X " q t " i t g c v g t 0 " V j g " o g c p of the particles was measured as a part of a 4-week stability test. However, non-modified PBNPs size showed a slight change in the diameter, i.e., after the third week, all PEGylated particles started to aggregate. PBNP-MB@PEG6000 nanoparticles were the most stable, along with the lowest PDI and diameter. As the size (hydrodynamic diameter) of the other two particles (PBNP-MB@PEG3000 and PBNP-MB@PEG8000) doubled after 3 weeks, the PBNP-MB@PEG6000 particles kept a solid size of  $24.82 \pm 5.83$  nm (number-based particle size distribution). According to these results, PBNP-MB@PEG6000 particles remained stable for the longest time, thus made them the best candidate for further inspections. However, aggregation was detected in the majority of the samples after 4 weeks of investigation.

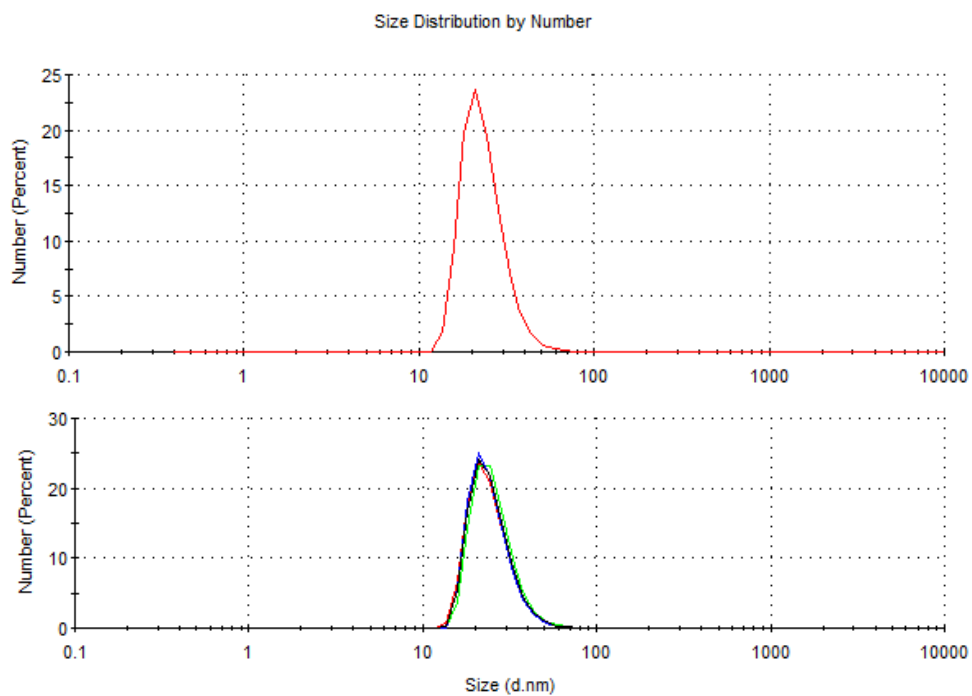


**Figure 12.** The size-distribution of PBNP-MB@PEG6000 nanoparticles, measured with DLS, after 1 week (top) and 3 weeks (bottom).

#### 4.1.2. In Vivo and Ex Vivo Measurements

Other approaches for fluorescent labelling and imaging; preformulation

In vivo, SNR of Eosine Y labelled nanoparticles proved to be insufficient for evaluable result; however, Figure 13 shows the ex vivo distribution of the particles. Hyperintense changes, mainly due to the PBNP treatment are visible in the liver and gastro-intestinal tract; the autofluorescence of the skin is also seen at this dye's main emission wavelength, further impeding the use of Eosine Y.

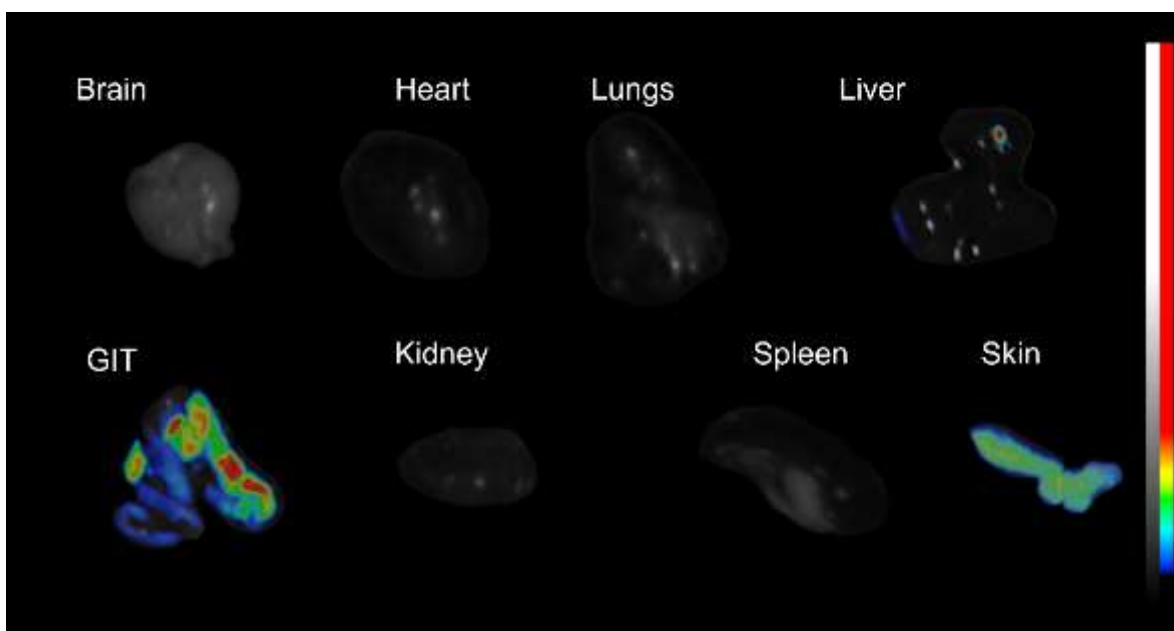


**Figure 13.** Ex vivo results of Eosine Y labelled PBNPs. (FOBI image, excitation 460-520 nm; cut off filter was permeable to the emission spectrum of the dye; exposure time: 1,000 msec; gain: 1.

Non-pegylated PBNPs had a good imageable contrast but eliminating them too fast did not prove to be advantageous for in vivo applications (Figure 14.).



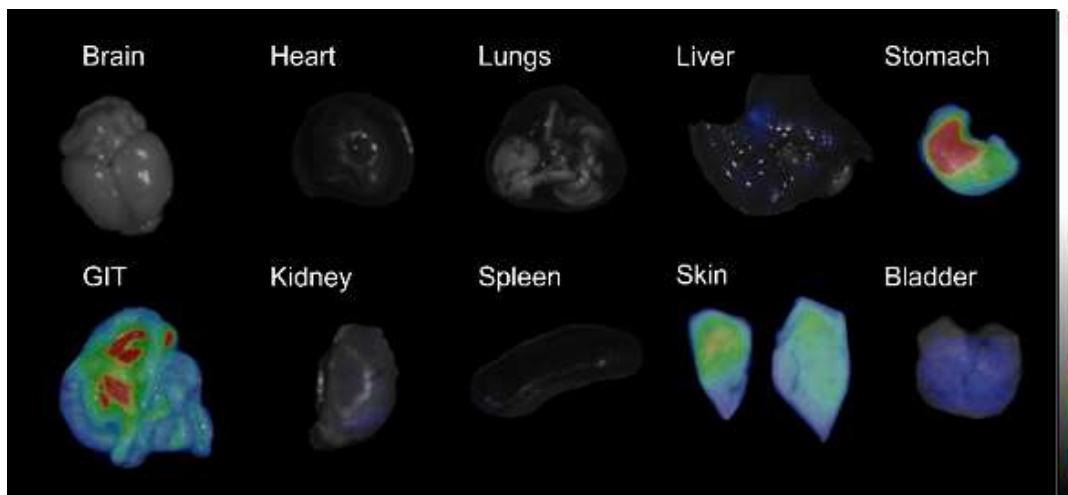


**Figure 14.** Methylene blue labelled non-pegylated PBNPs, in vivo. (FOBI image; excitation 630-680 nm; cut off filter was permeable to the emission spectrum of the dye; exposure time: 1,000 msec; gain: 1).

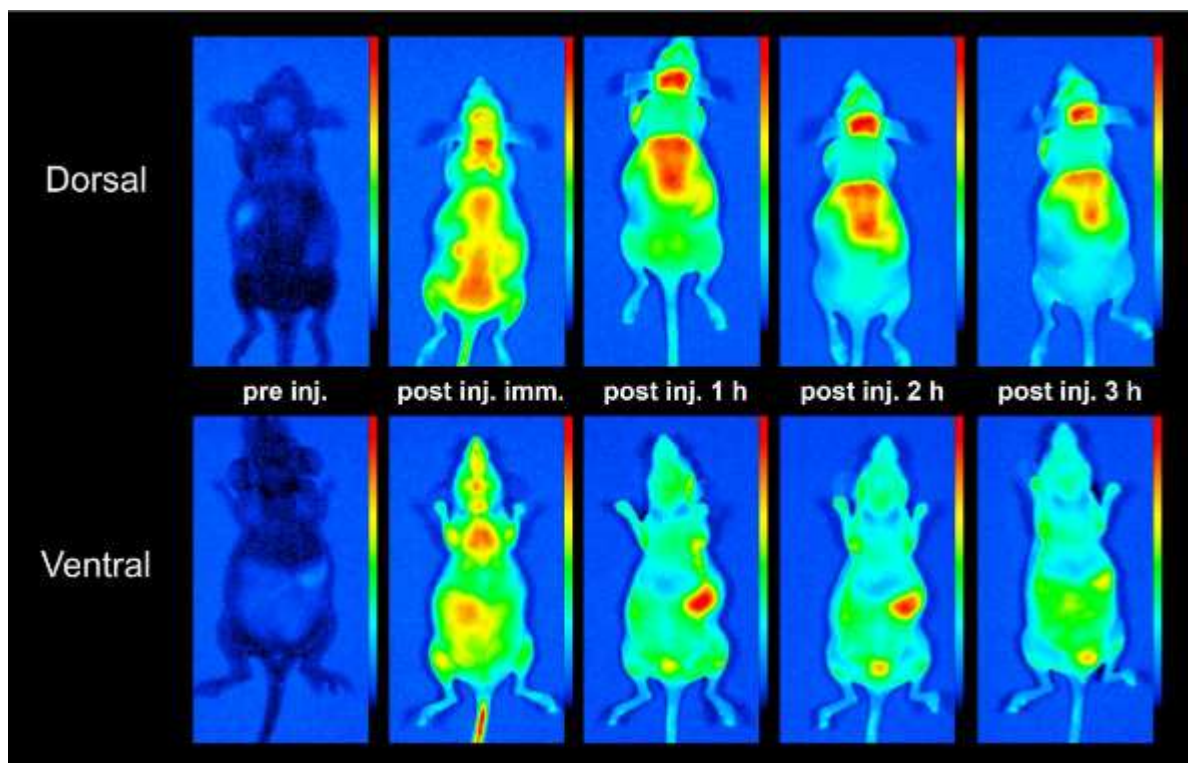


**Figure 15.** Methylene blue labelled PBNPs, ex vivo (FOBI image; excitation 630-680 nm; exposure time: 1,000 msec; gain: 1). Nanoparticles are present in the liver, stomach, gastrointestinal tract and skin.

A series of fluorescent distribution measurements was executed 1, 2 and 3 hours after intravenous administration of MB labelled PBNPs respectively (Figure 15.).

The fluorescent labelling and imaging: Methylene blue labelled Prussian blue nanoparticles

Due to the strong visible fluorescent signal of PBNP-O D B R G I 8 2 2 2 u . " 4 2 2 " N " suspension of nanoparticles was injected into the lateral tail vein of C57BL/6 male mice (Figure 16 (A, B)). The semiquantitative distribution of the labelled PBNPs was determined based on their normalized mean fluorescent intensity. On the ex vivo images (Figure 16 (B), taken 3 h after the first injection, PBNP-MB@PEG6000 accumulation can be observed in the gastrointestinal tract, kidneys, spleen, liver, and heart. The distribution of the particles on Figure 15. shows similar patterns as Figure 16 (B): Nanoparticles are present in the liver, stomach, gastro-intestinal tract and skin.

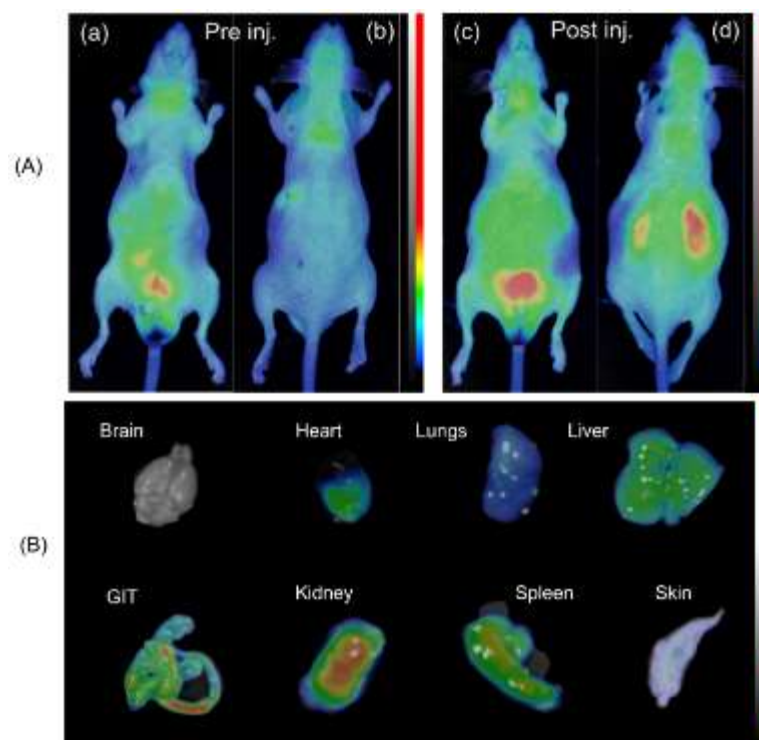


**Figure 16.** (A) (a,b) C57BL/6 mice before intravenous treatment from anterior and posterior planes. (c,d) C57BL/6 mice pre-PBNP treatment (anterior and posterior planes). (a) anterior, preinjection; (b) posterior, preinjection; (c) anterior, postinjection; and (d) posterior, postinjection. Color scale equals mean fluorescent intensity (MFI) in arbitrary units (A.U.)

Figure 16 (B) ex vivo images, 3 h post injection

## 4.2. Prussian blue-based dual fluorescent and magnetic contrast agent

### 4.2.1. In vitro results

#### DLS and zeta potential

The mean hydrodynamic diameter (intensity-based harmonic average) of complex PBNPs was  $82.91 \pm 1.21$  nm (average  $\pm$  SD), as determined by DLS (Figure 18.). This had only changed slightly with time. There was no significant colloidal alteration during the 4-week duration of the study, as the calculated  $0.244 \pm 0.014$  polydispersity index (PDI) shows the PBNPs did not flocculate or aggregate during this time. The mean zeta potential of PBNPs  $\pm 3.8$  mV (n=3) (88).

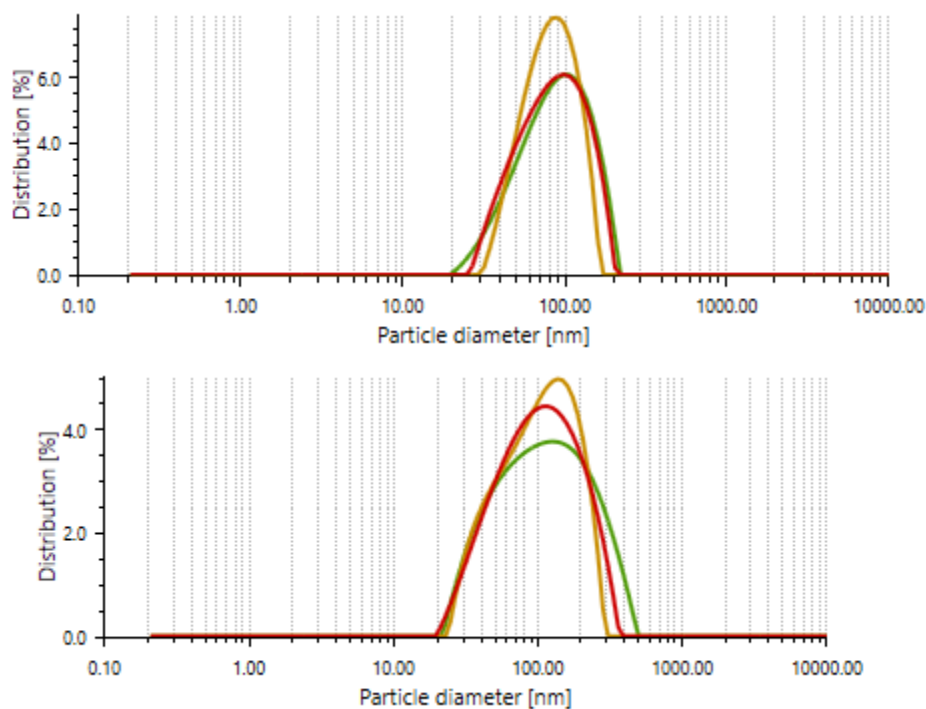


**Figure 17.** The size-distribution of PBNP-complex nanoparticles, measured with DLS, after 1 week and 3 weeks. The curves with different colors represent the 3 measurement series, conducted for each sample.

## Atomic Force Microscopy

The measured width of the particles was influenced by tip convolution. Figure 19a shows PBNPs on AFM images as objects with a flat rectangular surface protruding from a rounded halo. Rectangularity of the particles (together with their halo) was found to be  $0.774 \pm 0.111$  (mean  $\pm$  SD), indicating that PBNPs indeed represent rectangular topography. The height of the particles was  $36.457 \pm 0.68$  nm (mean  $\pm$  SD).

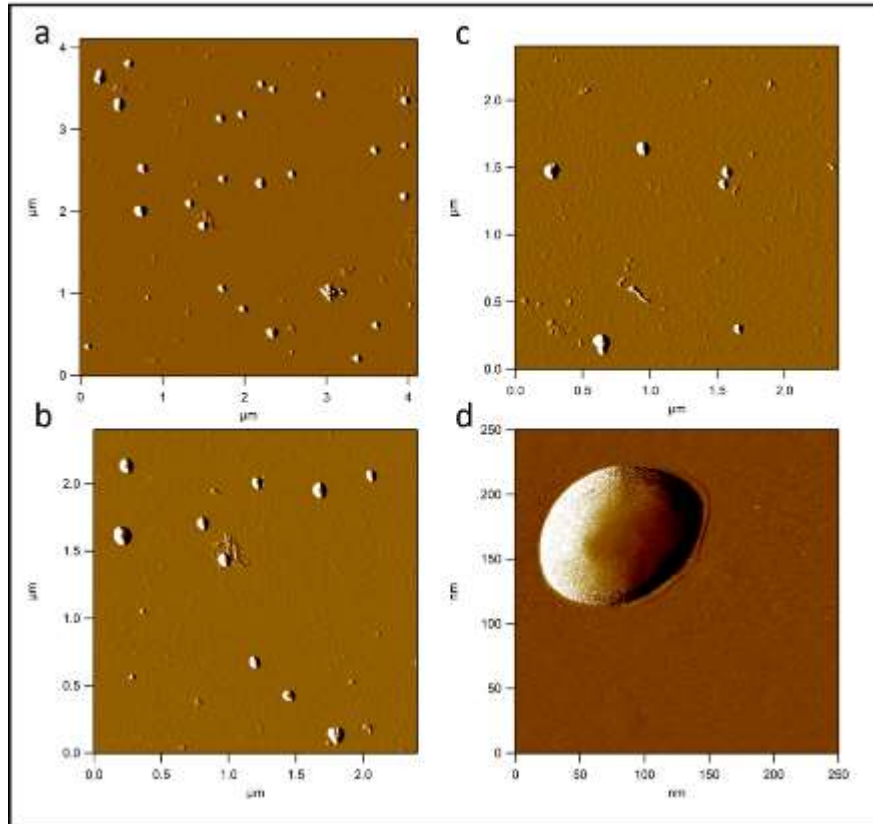


**Figure 18.** Atomic force microscopy (AFM) amplitude-contrast images with different magnification of PBNPs on mica surface.. The size of the images are  $4.125 \mu\text{m} \times 4.125 \mu\text{m}$  (Figure 18a.),  $2.5 \mu\text{m} \times 2.5 \mu\text{m}$  (Figure 18b. and c.) and  $250 \text{ nm} \times 250 \text{ nm}$  (Figure 18d.) respectively (88). Figure 18 b. and c. are different areas of the measured sample.

### Transmission Electron Microscopy

The non-hydrated shape and size of the PBNPs were investigated with TEM. PBNPs appeared flat rectangular, dense objects in this case as well. The mean diameter of the particles was  $19.2 \pm 1.9$  nm, along with an average surface area of  $579.257 \pm 398.983$  nm<sup>2</sup> (mean  $\pm$  SD; n = 1059 particles).

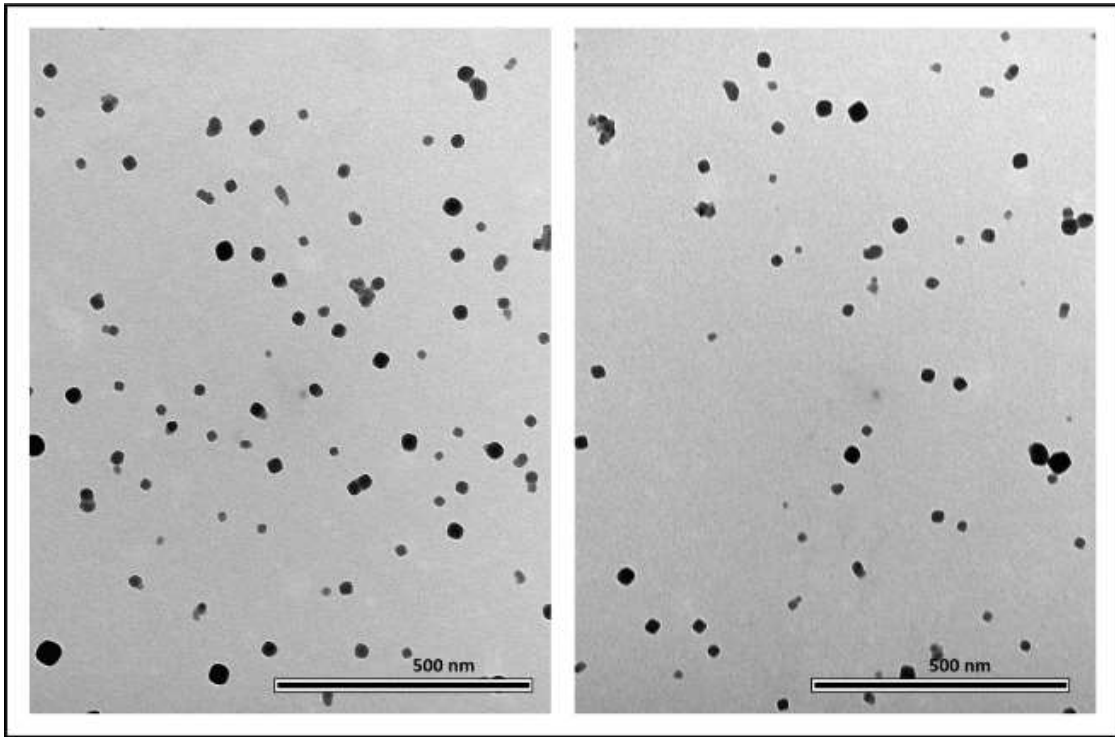


**Figure 19.** TEM images of PBNPs on different parts of the carbon-coated copper grid. PBNPs appeared flat rectangular, dense objects. The smaller objects on the image are individual PBNP particles which are not conjugated into the final PBNP complex (88).

#### 4.2.2. In vivo results

##### Magnetic resonance imaging

To demonstrate the positive MR contrast enhancing property of our PBNP sample, T1-weighted images of a phantom (containing three different Fe(Fe (III)) concentrations (13.75 mM, 41.25 mM, and 82.5 mM) containing PBNP solutions) were scanned to visually evaluate the signal enhancement on T1-weighted image. Based on the inversion prepared gradient echo scan and the multislice multiecho scan T1 relaxations rate were calculated. Afterward

the T1 relaxation time was calculated.

Nanoparticles without any conjugated specific in vivo targeting agent are initially dispersed in the circulation system and started to accumulate mainly in the reticuloendothelial system (RES; e.g. liver, spleen)(93, 94). To investigate the PBNP uptake efficiency, especially in RES, the PBNP distribution was determined on T1-weighted MR images (Figure 20). Enhanced signal intensities were registered in the lungs, liver, kidneys, and abdominal vein (Figure 20.) (88, 95).



**Figure 20.** Axial T1-weighted MR images of a mouse (A) before and (B) 30 minutes after intravenous administration of Prussian blue. Red arrows indicate that regions where signal intensity changes happened. Enhanced signal intensities were registered in the lungs, liver, kidneys, and abdominal vessel, which supports the results of a previous publication (88, 95).



### Optical imaging

Figure 21A illustrates the autofluorescence signal from the animal at pre-injection condition at 690 nm, while Figure 21B shows the fluorescent signal after the PBNP administration. Enhanced dye concentration was registered in the head and thoracic region based on the high dye content of the circulation system, furthermore the images illustrated the liver of the animal. According to the studies of Zhang et. al. and Huang et. al., IR820 connected to different types of carrier systems shows great photo- and pH stability, as well as in aqueous media (88, 96, 97).

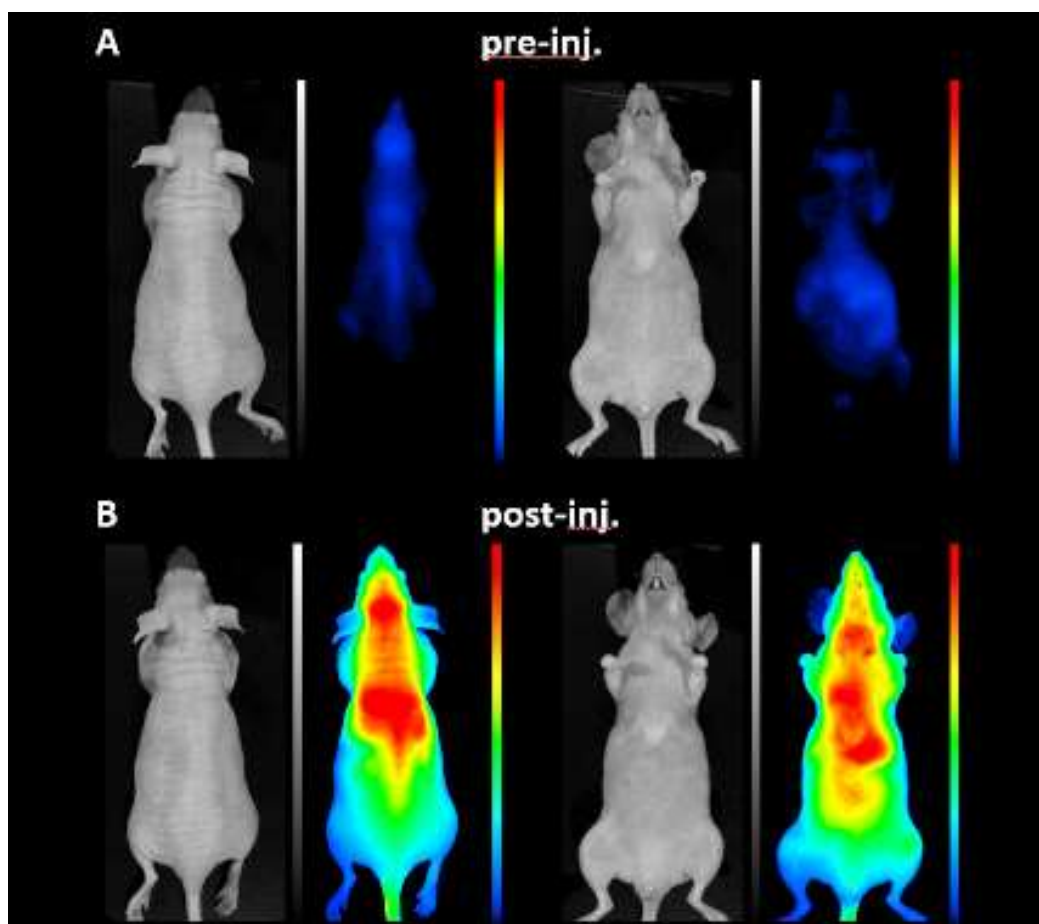


**Figure 21.** Non-excitated and fluorescent images of a mouse (A) before and (B) after intravenous administration of Prussian Blue (images from left to right: prone white, prone fluorescent, supine white, supine fluorescent images) at 690 nm. The images are highlighted on the same dynamic color look-up table, which illustrates the signal intensity with different tone from cold to hot colors (88).

## 5. Discussion

### 5.1. PEGylated, fluorescent Prussian blue nanoparticles

#### 5.1.1. In vitro measurements

##### Preformulation

The main concept of preformulation gained relevance along with the widespread use of the Qbd concept, in the late 60s, namely to generate information regarding the product, in order to achieve a stable, bioavailable dosage form, for possible mass production (98). Preformulation studies include but are not limited to only physico chemical and analytical investigations of a previously known material, but also the investigation of the need of possible excipients, biopharmaceutical and therapeutic availability studies (99).

The main goal in our study was to produce a stable nanosystem in a well-defined size-range and optimal fluorescent pigment concentration, which would also help to reduce the possible absorption of the fluorescently labelled PBNPs, leading to an increased fluorescent signal and reduced toxic effects, during the imaging steps. In order to achieve this, we used our previous knowledge, for the temperature dependence of the PBNP formulation, and investigated the surface charge and size-distribution of each sample, in every formulation (56, 89).

##### Atomic Force Microscopy (AFM)

Atomic force microscopy is considered a powerful reference tool for the scanning and characterization of nano-sized samples, by observing a NP population directly, creating a direct, non-calculated connection between the particle size and dimension, based on the SI units system (100-102). During a measurement only the height of the particles could be determined due to the tip convolution which leads to artificially modified lateral dimensions on the images (103). On Figure 7. PBNPs appeared as objects with a flat rectangular surface protruding from a rounded halo (Figure 7a). The rectangular surface represents the real geometry of the particles (Figure 7c) while their halo is the consequence of tip convolution, i.e., the effect of imaging a rectangular prism by a tetrahedral AFM tip.



### Scanning Electron Microscopy (SEM) and Transmission Electron Microscopy (TEM)

The electron microscopy, regardless of the type scanning or transmission, is a powerful tool for the characterization of great varieties of materials. Having exceedingly high spatial resolution and versatility is often a great advantage during the development of novel substances (104-106). Nevertheless, Transmission Electron Microscopy (TEM) is providing information from inside of the pico-sized scanned probes, while Scanning Electron Microscopy (SEM) can provide valuable information about its nano-sized topographical features (107, 108). Due to the sample preparation process, SEM images show an aggregated nanosystem where the particles appear as rectangular objects. Single particles were hard to distinguish from one another, however, their size did not exceed the 100 nm threshold (Figure 8a). The nonhydrated shape and size of the NPs were also analyzed with TEM (Figure 8b,c). The nanosystem was slightly aggregated (Figure 8c), however, single particles could be observed. The results of SEM and TEM measurements support the results of the AFM measurements, which suggests the PBNPs as rather rectangular solid objects, within the sub-50 nm size-range.

### Fourier Transformation Infrared Spectroscopy (FT-IR)

As a solid dispersion measuring method, Fourier Transform Infrared spectroscopy (FT-IR), is a commonly used technique in pharmaceutical research to determine the molecular composition and interactions in solid, liquid or gas-phase samples (109). This method reveals the lengths of the bonds, the molecular mass changes and the band-order of molecules. Hypsochromic shifts (shifts to lower wavenumbers) suggest that the mass of the corresponding molecule has been increased; the frequency of vibration is inversely proportional to mass of vibrating molecule. In the sample, the absorption bands near 3,415 and 1,610  $\text{cm}^{-1}$  refer to the O-H stretching mode and H-O-H bending mode, respectively, indicating the presence of interstitial water in the samples (Figure 9 (a-d)) (110-112).

The FTIR absorption spectra (Figure 9/I) give a comparison between unmodified PBNPs (Figure 9/I (a)) and the PEG 6000 and Methylene blue modified PBNPs (Figure 9/I (d)). In addition, the spectra of PEG 6000 (c) and MB (b) are shown, ranging from 400  $\text{cm}^{-1}$  to 4,000  $\text{cm}^{-1}$ . On the spectra of the pure and modified PBNPs, the peaks at 2,090  $\text{cm}^{-1}$  and 494  $\text{cm}^{-1}$

e q t t g u r q p f " v q " v j g " u v t g - C N e F e , w h i c h a r e t h e t y p i c a l s i g n a l s p " q h " E  
 of PB. Typically, peaks over  $3,200\text{ cm}^{-1}$  are ascribed to O-H group, indicating the presence  
 of interstitial water in the PB. (Figure 9/I (a-d)). Figure 9/I (d) shows that the bands shift to  
 lower wavenumbers. Furthermore, the peaks of PEG 6000 (c) and MB (d) could be identified,  
 indeed, after the hypsochromic shift. Figure 9/I (c) shows the absorption spectrum of PEG  
 6000. A broad band at  $3,300\text{ cm}^{-1}$  is present, which can be related to an O-H stretching mode  
 while the band at  $1,650\text{ cm}^{-1}$  is a H-O-H bending vibration. A characteristic peak can be  
 determined at  $1,100\text{ cm}^{-1}$ , which shows the C-O bonds. Figure 9 (b) represents the absorption  
 spectra of Methylene blue. Characteristic peaks can be observed at 3,265, 2,114, 1,633 and  
 585  $\text{cm}^{-1}$ . On Figure 9/II (a), characteristic peak of PBNPs are present at  $2,090\text{ cm}^{-1}$ , which  
 c q t t g u r q p f u " v j g " u v t g v e j k p i " x k d t c v k o q n p i e h " E P 0 "  
 a peak is present above  $2,7000\text{ cm}^{-1}$ , which is related O-H (or O-D) stretching mode while  
 the wider band (compared to the completely dry sample) at  $1,650\text{ cm}^{-1}$  is a H-O-H (or D-O-  
 D) bending vibration. Aromatic groups and methly groups are visible on Figure 9/II (b).  
 Aromatic groups and methyl groups are visible at  $2807$  and  $2710\text{ cm}^{-1}$  represent the stretching  
 vibration of -CH- and -CH<sub>3</sub>, aromatic vibrations are present from  $1601$ - $1372\text{ cm}^{-1}$ , while the  
 vibrations of the C=C skeleton of the dye are present at  $1171\text{ cm}^{-1}$  (Figure 9 (b)). The spectra  
 of PEG 6000 (Figure 9/II (c)) shows wide bands at  $\sim 3500\text{ cm}^{-1}$ ; these are related to the -OH,  
 and the -C-O stretching is clearly visible  $\sim 1200\text{ cm}^{-1}$ . On the other hand, Figure 9 (d) has a  
 visible vibration band around  $1170\text{ cm}^{-1}$ , which could represent the C=C skeleton of the  
 c t q o c v k e " t k p i 0 " C n u q . " u k i p u l , " a n d t h e b a n d o f - O H f u " c t g "  
 around  $3500\text{ cm}^{-1}$  and -C-O stretching around  $1200\text{ cm}^{-1}$ . The vibration and stretching bands  
 can be related to both citric acid and PEG, as well was PB itself.

#### X-Ray diffraction (XRD)

X-t c { " r q y f g t " f k h h t c e v k q p " k u " p q v " q p n { " e c r c d n g "  
 u v q p g u ö " q h " c " p c p q u v t w e v w t g = " w u k p i " D t c i i ø u " c p  
 shape can be also determined (Equation 1. and Equation 2.). Nevertheless, the limitations of  
 XRD data should be also acknowledged, this characterization method could offer key  
 information about for the identification, quantification and characterization of nanomaterials,  
 in the designing and development phase (113).

$$n\lambda = 2d \sin\theta$$

**Equation 1.**  $d$  is the distance of the crystal planes,  $n$  is the diffraction order,  $\lambda$  is the wavelength of the incident X-ray, and  $\theta$  is the angle of diffraction.

$$\tau = \frac{K\lambda}{\beta \cos\theta}$$

**Equation 2.**  $K$  is the Scherrer constant,  $\lambda$  is the wavelength of the incident X-ray,  $\beta$  is the full width at half maximum (FWHM) of the diffraction peak, and  $\theta$  is the angle of diffraction.

X-ray diffraction is based on the elastic scattering of x-rays from structures that have a longrange order. It discovers the geometry or shape of a molecule.

The two samples ((a)Prussian blue reference solution, which was used later for pegylation and methylene blue labelling and (b) pegylated, fluorescent labelled PBNPs) were measured.

The XRD patterns of the Prussian blue reference solution and the pegylated, fluorescent labelled PBNPs are shown in Figure 10 (a) and (b) respectively. The diffraction peaks of the Prussian blue reference solution are indexed to the face-centered cubic structure of PB with space group Fm3m. The diffraction peaks of the pegylated, fluorescent labelled PBNPs are indexed to the face-centered cubic structure of PB with space group Fm3m. The diffraction peaks of the Prussian blue reference solution are indexed to the face-centered cubic structure of PB with space group Fm3m. The diffraction peaks of the pegylated, fluorescent labelled PBNPs are indexed to the face-centered cubic structure of PB with space group Fm3m. This shows unmodified PBNP crystals in the sample, as well as the proved the presence MB crystals.

### Measuring In Vitro Fluorescence

Before administering fluorescently labelled nanoparticles to laboratory animals, it is essential to measure their in vitro fluorescence because it gives insight into their stability, brightness, and photostability. Additionally, it can help establish the ideal nanoparticle injection concentration and confirm the labeling's specificity. Based on Figure 11. Different dilutions of fluorescently labelled PBNPs were measured, to simulate the possible twenty-fold dilution within the body of the examined animals. As a proof-of-concept, this dilution produces optimal fluorescent signal for the fluorescnet imaging, suggesting an optimal result in vivo.

### Stability Measurements of PBNP-MB@PEG Nanoparticles

The applied citric acid as surface-capping agent controlled the size and the biocompatibility of the synthesized particles and seemed an appropriate agent to avoid aggregation (92). The reported PEGylated MB-labelled PBNPs remained stable for about 3 weeks, while the previously reported, citrate-coated PBNPs did not aggregate in a biologically relevant manner after 4 weeks (38, 118). This lets us conclude that the increased complexity on the nanoparticle surface leads to a shorter stability and usability. Based on the studies of Namazi et al. and Naeini et al., over time, citric acid and PEG are forming a self-aggregating system in our samples (36, 58). These dendrimers would offer a protective layer for PBNPs while encapsulating them along with the fluorescent dye MB. Our results suggest that further improvement would be necessary to synthesize a more stable PBNP platform for multimodal use as, e.g., MR-CA, radiotracer or therapeutic functions.

#### 5.1.2. In Vivo and Ex Vivo Measurements

In medical imaging, the safety and discomfort of patients are important; therefore, a significantly faster and safer method used for lengthy and repeated procedures could make a huge impact on both diagnostics and monitoring. Optical methods are peculiarly useful for visualizing soft tissues, which can be easily differentiated from each other based on their light-absorbing and -scattering capabilities. The dual modalities allow better chances for inspection, based on different kinds of imaging modalities, e.g., MRI and OI. Finally, if an acute intervention is required, the need of repeated CA administration could be preventable, if the half-life (and clearance) of the nanoteragnostic agent is adequate (22, 23, 119).

The total workings of the immune system play a significant role in the distribution, metabolism, and elimination of nanoparticles. As Diao et al. and Hong et al. used C57BL/6 mice of IR imaging, we also decided to test our nanosystem in C57BL/6 mice that have an intact immune system as opposed to immunocompromised nude mice (120, 121). This might have made our imaging signals more scattered, but increased the validity of the model towards, eventually, clinical translational studies.

The elimination and excretion of nanoparticles is, however, poorly investigated. Due to its mainly oral administration, only a few studies have been published data regarding I.V. PB

administration. As far as we know, ultrasmall PBNPs tend to be excreted via glomerular pathways, while after oral administration, PBNPs are excreted via fecal and urine routes (56, 61, 122). The few available reports dealing with biodistribution and elimination of PBNPs after intravenous injection are not conclusive. It would seem, though, that in those studies, kidney excretion was not relevant despite smaller PBNP deposits in the mesangium and the peritubular vessels of (56, 58). Our findings with the new coating and dye-adsorbed-modified PBNPs suggest that both kidney and biliary elimination routes play a major role in the excretion of this nanoparticle system. Shortly after iv. administration, the particles could be found in the urinary tract, showing an enhanced fluorescent signal 3 h after the admission. This, along with our previous observations obtained with irreversibly  $^{201}\text{Tl}$ -isotope-labelled PBNPs passing through the kidney to the urinary excretion route, suggests a portion- of kidney excretion via fenestrae of the kidney endothelium and podocytes, especially in our measured hydrodynamic size range below 40 nm (56).

In order to account for eventual dissociation of the MB dye from PBNP surfaces, we compare the known elimination routes and dynamics of MB dye solution to our MB-labelled PBNPs. Peter et al. reported that while MB alone accumulates in the brain and bile, mainly urinary excretion is significant 1 h after IV administration. The maximal concentration during urinary excretion was reached 264 h after administration (123). In this context, our results suggest that MB stayed bound to PBNPs as both renal clearances are prolonged while the PEG shell alone did not significantly increase the renal excretion speed. The fluorescent intensity in the heart, liver, and spleen suggest a prolonged circulation time. Significant uptake can be observed in the lungs ( $501\% \pm 85\%$ ; 2 h post injection  $156\% \pm 60\%$ ) and spleen ( $163\% \pm 18\%$ ), while a slight increase in fluorescent intensity in the intestines ( $107\% \pm 5\%$ ), along with the urinary excretion ( $272\% \pm 32\%$ ; 3 h post injection  $177\% \pm 20\%$ ) (percent values based on normalized fluorescent intensities preinjection  $\pm$  SD). These results suggest that the MB and PBNPs were connected, and their clearance followed the both characteristic pathways for MB and PBNP; furthermore, the PEG shell alone did not promote the renal excretion significantly. The fluorescent intensity in the heart, liver, and spleen suggest a prolonged circulation time (Figure 16.). In contrast to this, non-pegylated samples were also

investigated (Figure 14 and 15.). The ex vivo images, in contrast to Figure 16 show hyperintense signals mainly in the GIT and kidneys, along with a moderate fluorescent signal in the skin. In this context, a part of PBNPs were labelled, not all the excretion routes are displayed in comparison to Figure 16. Furthermore, this also lets us conclude the crucial role of PEG for the fluorescent labelling. As a control, Eosine Y was also investigated and found not to be capable of producing sufficient fluorescent signal neither in the animals, nor on the ex vivo images (Figure 13).

The ex vivo images confirm that the application of PEG led to an increased biological half-life and slowed excretion rate, both biliary and urinary, compared to previous studies (124-126). Even if other studies emphasize the connection between filtration and negative surface charge and larger particle size, PEGs are known as rather neutrally charged stabilizers. According to Liu et al. and Souris et al., complete clearance of PEG-modified nanoparticles last for 2 months, and thus, show a tendency of hepatic and renal accumulation causing local inflammation and necrotizing tissue (127, 128).

Chen et al. investigated the acute and subchronic toxicological properties of Prussian blue nanoparticles after exposure of mice. PBNPs accumulated mainly in the spleen and liver. They found that, however, PBNPs induced acute damage in the liver (based on the liver functions), the long-term effects of PBNP-treatment cannot be called negative. All monitored parameters returned to normal levels, 60 days after the first IV PBNP administration (129). Our results also confirm the claims of Chen et al.; in the ex vivo images (Figure 16), PBNPs were present in the spleen and the liver; biliary functions resulted in PBNP presence in the gastrointestinal tract.

## 5.2. Prussian blue-based dual fluorescent and magnetic contrast agent

The final PBNP complex nano structure was prepared by the combination of Shokouhimeht  $\phi$  u " method (57) and our previously published one-step citrate coated PBNP procedure (56). The synthesis of PBNPs with and without coating resulted in two different types of PBNP solutions, which were mixed. During the incubation and mixing period, the particles were able to connect to each other via carboxyl groups of citric acid and a form a bigger and iron-

richer formula. The porous surface of the nanoparticles assured the conjugation points for the fluorescent IR820 dye (Figure 22) (88).

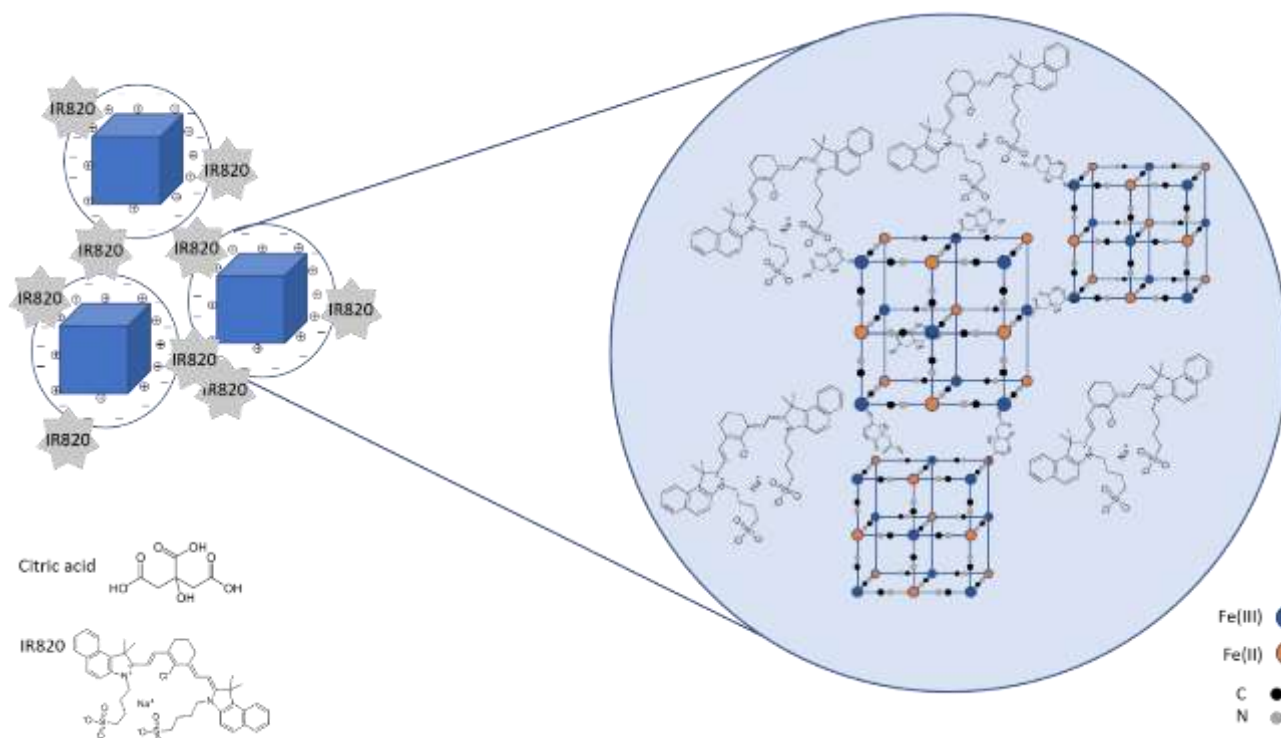


**Figure 22.** Schematic illustration of the presumed connection of Prussian blue nanoparticles (PBNPs) with and without coating and the particle conjugation by IR820. The blue halo around the PBNPs represent the non-biocompatible PBNP-species (PB-HCl) acting as a coating surface. The colors represent the following ions or atoms, respectively: blue: Fe(III); orange: Fe(II); black: C; gray: N (88).

### 5.2.1. In vitro results

#### DLS and zeta potential

The mean hydrodynamic diameter (intensity-based harmonic average) of complex PBNPs was  $82.91 \pm 1.21$  nm (average  $\pm$  SD), as determined by DLS (Figure 18.). This had only changed slightly with time. There was no significant colloidal alteration during the 4-week duration of the study, as the calculated  $0.244 \pm 0.014$  polydispersity index (PDI) shows the PBNPs did not flocculate or aggregate during this time. The mean zeta potential of PBNPs was  $-38.5 \pm 3.8$  mV (n=3) (88).

### Atomic Force Microscopy and

The measured width of the particles was influenced by tip convolution. Figure 19a shows PBNPs on AFM images as objects with a flat rectangular surface protruding from a rounded halo. The rectangular surface represents the real geometry of the particles while their halo is the consequence of tip convolution, i.e., the effect of imaging a rectangular prism by a tetrahedral AFM tip. Rectangularity of the particles (together with their halo) was found to be  $0.774 \pm 0.111$  (mean  $\pm$  SD), indicating that PBNPs indeed represent rectangular

### Transmission Electron Microscopy

The non-hydrated shape and size of the PBNPs were investigated with TEM. PBNPs appeared flat rectangular, dense objects in this case as well. The mean diameter of the particles was  $520.36 \pm 320.878$  nm (mean  $\pm$  SD; n = 1059 particles). The measured surface area of  $579.257 \pm 398.983$  nm<sup>2</sup> (mean  $\pm$  SD; n = 1059 particles). The measured height by TEM was in good correlation with the results of AFM measurements describing the shape of non-hydrated particles. By both cases, the flat rectangular objects represent the real geometry of the particles (88).

### 5.2.2. In vivo results

#### Magnetic resonance imaging

To demonstrate the positive MR contrast enhancing property of our PBNP sample, T1-weighted images of a phantom (containing three different Fe(Fe (III) concentrations (13.75 mM, 41.25 mM, and 82.5 mM) containing PBNP solutions) were scanned to visually evaluate the signal enhancement on T1-weighted image. Based on the inversion prepared gradient echo scan and the multislice multiecho scan T1 relaxations rate were calculated. Afterward the T1 relaxation time (ms) was calculated. The more significant T1 shortening effect for PBNPs could be explained by a carbon-bound and low-spin of Fe<sup>2+</sup> in the PB structure, in contrast to the high spin nitrogen-bound Fe<sup>3+</sup> (57). Our result demonstrates that PBNPs have substantial T1 MRI contrast compared to other T1 CAs (130, 131). Nanoparticles without any conjugated specific in vivo targeting agent are initially dispersed in the circulation system and started to accumulate mainly in the



reticuloendothelial system (RES; e.g. liver, spleen)(93, 94). To investigate the PBNP uptake efficiency, especially in RES, the PBNP distribution was determined on T1-weighted MR images (Figure 20). In the case of in vivo MRI scans, we were able to register contrast changes between the pre- and post-injection scans immediately after the PBNP administration. Enhanced signal intensities were registered in the lungs, liver, kidneys, and abdominal vein (Figure 20.), which supports the results of previous publication (88, 95).

#### Optical imaging

Due to the strong visible fluorescent signal of IR820 conjugated PBNPs the semiquantitative distribution of the particles was determined based on their normalized mean fluorescent intensity. Figure 21A illustrates the autofluorescence signal from the animal at pre-injection condition at 690 nm, while Figure 21B shows the fluorescent signal after the PBNP administration. Enhanced dye concentration was registered in the head and thoracic region based on the high dye content of the circulation system, furthermore the images illustrated the liver of the animal. According to the studies of Zhang et. al. and Huang et. al., IR820 connected to different types of carrier systems shows great photo- and pH stability, as well as in aqueous media (88, 96, 97).

## 6. Conclusion

In this study the synthesis and modification of biocompatible, stealth, fluorescent and MRI contrast capability of PBNPs were demonstrated.

The PEGylated, MB labelled PBNPs offer a novel synthesis method to produce contrast material for the classical fluorescent measurement methodology. The MB-labelled PB nano-objects were investigated in vivo after intravenous administration, whereas the hepatobiliary and renal uptake and excretion were detected.

The synthesized NIR-820 conjugated PBNP nanoparticles appear to be an appropriate MRI and optical contrast material. By application of surface modification of citrate coated PBNPs with coatless nanoparticles, a slightly enlarged, iron rich complex nano system was produced. The obtained nanofiber was observed to possess an enhanced in vitro and in vivo T1-weighted MR contrast. The further conjugation with NIR-820 dye resulted in an optically active complex nano material for in vivo use. The nano system exhibited high colloidal stability and monodispersity after each modification step. The relaxivity constant in this investigation demonstrated that produced nano material is an appropriate candidate for further MRI and OI investigation.

With both PEGylation and fluorescent labelling PB nanoparticles are able to be conferred with advanced technological properties in order to offer a finely tuned platform for clinical application after further development. The optimal aim is implementing clinical translation as well as the application of MB and NIR wavelength. As fluorescent detection and imaging in a suboptimal in vivo system are more convincing if extended towards human clinical trials, the use of standard are more clinically relevant black mice might have been a preferred choice for validity and detection of our studies. However, the rather transparent nude mice are a less clinically translatable yet easily imageable.

Therefore, c r r n { k p i " v j g " e q p e g r v " q h " õ S d F ö " f w t k p i nanoparticles, for the detection of the critical synthesis parameters, as well as measuring the nanosystem in two imaging modalities were an optimal choice for this study, resulting in further development and towards the clinical implementation.

### 6.1. Achievements

- I. A stable nanoparticle platform was created, which held its stability for the 4 weeks period of examination.
  - The system emitted fluorescent signal, which was detected during in vivo imaging
  - The possible clearance routes were observed, clearance was facilitated with the addition of PEG
- II. Prussian blue nanoparticles were successfully labelled with methylene blue
- III. The connection of the fluorophore was facilitated by the fluorescent coating
- IV. In vivo fluorescent imaging was executed and fluorescent images were captured over the examination time of 3 hours.

Based on the fluorescent labelling experience,

- V. A stable Prussian blue-based T1 MRI contrast-capable nanoparticle was developed and it was successfully labelled with fluorescent dye,
  - Characterization was executed in vitro with DLS, AFM, TEM, and Zeta-potential measurements
- VI. In vivo T1 MRI contrast was obtained,
- VII. And NIR fluorescent contrast was measured in vivo.

## 7. Summary

In the presented work, we studied the possibilities of using biocompatible Berlin blue nanoparticles (PBNP) as a multimodal contrast agent with different physical-chemical investigation methods. We added various fluorescent dyes to nanoparticle suspensions and examined their stability. Although particles labeled with Eosin Y and methylene blue dye were suitable for in vivo imaging, the application of the former was not possible due to experienced aggregation problems. The characteristics of the particles were examined by DLS, zeta-potential measurement, SEM, TEM, AFM, XRD, and FTIR measurements. Both physical and structural measurements confirmed successful labeling and optimal stability for in vivo use. The particles' presence in the animals' organs was confirmed by in vivo measurements. In the second part of the experiments, we produced non-biocompatible PBNPs, which we combined with biocompatible PBNP and infrared dye solutions. We used IR820 dye for fluorescent labeling based on previous the precious experiments. The physico-chemical investigations were carried out as described before. We determined the average particle size and size-distribution of the nanosystem. In vivo measurements showed hyperintense changes on T1-weighted MRI images in several organs, resulting from the PBNP complex.

In the case of fluorescent labeling, MB proved to be a suitable fluorescent dye for the labelling of PBNPs. To achieve optimal stability, we needed to add PEG 6000 sterically stabilizing agent. In addition, infrared labeling with IR820 was also successfully feasible. Contrast enhancement on MRI images was only possible with the combination of two PBNP species. Based on the results of the study, we determined the critical parameters of PBNP production. Based on these, PBNPs can be implemented and well-suited for optical and MRI multimodal imaging.

The synthesized particles have excellent stability in aqueous solutions, and their physical shape and size can be determined as part of quality control. Further optimization of the system, such as increasing T1 contrast, drug molecule incorporation, and using PBNPs as a drug carrier system, could further increase the chances of such a system entering the market.

## 8. Összefoglalás (Summary in Hungarian)

A bemutatott munkában a biokompatibilis Berliini kék nanorészecskék (PBNP) multimodális

kémiai vizsgáló módszerekkel. A nanorészecskék ultrahangos, röntgen, elektronmikroszkopikus, UV-Vis, fluoreszcens, DLS, TEM, AFM, XRD és FTIR mérésekkel vizsgáljuk. A nanorészecskék ultrahangos, röntgen, elektronmikroszkopikus, UV-Vis, fluoreszcens, DLS, TEM, AFM, XRD és FTIR mérésekkel vizsgáljuk. Ugyan az Eozin Y és a metilénkék festékekkel jelölt részecskék alkalmasnak bizonyultak az in vivo képalkotásra. A fluoreszcens, TEM, AFM, XRD és FTIR mérések segítségével vizsgáltuk. A fizikai és a szerkezeti mérések is sikeres jelölést, valamint az in vivo felhasználás szempontjából optimális stabilitást igazoltak. Az in vivo mérésekkel megvizsgáltuk a PBNP-k biokompatibilitását. A fluoreszcens jelölés esetében az MB o g i g fluoreszcens festéknek bizonyult a PBNP jelzésére. Az optimális stabilitás eléréséhez PEG 6000 sztérikus stabilizáló hozzáadására volt szükség. Emellett az IR820-csúszó, vörös, UV-Vis, fluoreszcens, DLS, TEM, AFM, XRD és FTIR mérésekkel vizsgáljuk. A fluoreszcens jelzés során korábbi tapasztalataink alapján IR820 festéket használtunk. A fizikai-mechanikai mérésekkel vizsgáltuk a PBNP-k stabilitását. Meghatároztuk a nanorendszer átlagos részecskeméretét, méreteloszlását. Az in vivo mérések a T1 súlyozott MRI-felvételeken intenzitás-növekedést mutattak több szervben is, melyet az ott található PBNP komplex eredményezett.

A fluoreszcens jelölés esetében az MB o g i g fluoreszcens festéknek bizonyult a PBNP jelzésére. Az optimális stabilitás eléréséhez PEG 6000 sztérikus stabilizáló hozzáadására volt szükség. Emellett az IR820-csúszó, vörös, UV-Vis, fluoreszcens, DLS, TEM, AFM, XRD és FTIR mérésekkel vizsgáljuk. A fluoreszcens jelzés során korábbi tapasztalataink alapján IR820 festéket használtunk. A fizikai-mechanikai mérésekkel vizsgáltuk a PBNP-k stabilitását. Meghatároztuk a nanorendszer átlagos részecskeméretét, méreteloszlását. Az in vivo mérések a T1 súlyozott MRI-felvételeken intenzitás-növekedést mutattak több szervben is, melyet az ott található PBNP komplex eredményezett.

A rendszer további optimalizálása úgy mint a T1 kontraszt további növelése valamint gyógyszermolekula inkorporációja és a PBNPk gyógyszerhordozó rendszerként való felhasználása tovább növelheti egy ilyen rendszer piacára kerülésének esélyeit

## 9. Bibliography

1. N. Politis S, Colombo P, Colombo G, M. Rekkas D. (2017) Design of experiments (DoE) in pharmaceutical development. Drug development and industrial pharmacy, 43: 889-901.
2. Juran JM. Juran on quality by design: the new steps for planning quality into goods and services. Simon and Schuster 1992.
3. Shewhart WA. Economic control of quality of manufactured product. Macmillan And Co Ltd, London 1931.
4. Guideline IHT. (2009) Pharmaceutical development. Q8 (2R). As revised in August.
5. Box GE, Wilson KB. On the experimental attainment of optimum conditions. In: Breakthroughs in statistics. Springer, 1992: 270-310.
6. Eriksson L, Byrne T, Johansson E, Trygg J, Vikström C. Multi-and megavariate data analysis basic principles and applications Vol. 1. Umetrics Academy 2013.
7. Group BC, Tollman P. A Revolution in R & D: How Genomics and Genetics are Transforming the Biopharmaceutical Industry. Boston Consulting Group 2001.
8. Máthé D, Mkuu D. "Ran { k " D. " Mkuu " \ . " H q t i ^ a e j " N. " Karlinger K, Kellermayer MS. (2021) The 3M Concept: Biomedical Translational Imaging from Molecules to Mouse to Man. The EuroBiotech Journal, 5: 155-160.
9. Staton CA, Reed MW, Brown NJ. (2009) A critical analysis of current in vitro and in vivo angiogenesis assays. International journal of experimental pathology, 90: 195-221.
10. Shatillo A, Koponen J, Miettinen T, Karkkainen A-M, Nurmi A. (2019) Functional Ultrasound: Charles River Laboratot k g u ø " p q x g n " k p " x k x q " k o c i l preclinical CNS drug discovery. Genetic Engineering & Biotechnology News, 39: 52-54.
11. Rosar F, Buchholz H-G, Michels S, Hoffmann MA, Piel M, Waldmann CM, Rösch F, Reuss S, Schreckenberger M. (2020) Image quality analysis of 44Sc on two preclinical PET scanners: A comparison to 68Ga. EJNMMI physics, 7: 1-17.
12. Marchant S, Yvon-Leroux J, Ouellet ÉB. (2020) IN VIVO NIR-II IMAGING.

13. Fø U q w | c " O U . " J q y g n n " G P . " T c { " U F 0 " T c f k q n  
radiopharmaceuticals. In: Side Effects of Drugs Annual Vol. 41. Elsevier, 2019: 531-547.
14. Chen D, Dougherty CA, Yang D, Wu H, Hong H. (2016) Radioactive nanomaterials for multimodality imaging. *Tomography*, 2: 3-16.
15. Ge J, Zhang Q, Zeng J, Gu Z, Gao M. (2020) Radiolabeling nanomaterials for multimodality imaging: New insights into nuclear medicine and cancer diagnosis. *Biomaterials*, 228: 119553.
16. Wang S, Zhao Y, Xu Y. (2020) Recent advances in applications of multimodal ultrasound-guided photoacoustic imaging technology. *Visual Computing for Industry, Biomedicine, and Art*, 3: 1-12.
17. Baldrick P. (2021) Nonclinical safety testing of imaging agents, contrast agents and radiopharmaceuticals. *Journal of Applied Toxicology*, 41: 95-104.
18. I q u n k p i " R 0 " \* 4 Illustrated Medical Dictionary. Australasian Chiropractic & Osteopathy, 11: 65.
19. Federle MP, Jaffe TA, Davis PL, Al-Hawary MM, Levine MS. (2017) Contrast media for fluoroscopic examinations of the GI and GU tracts: current challenges and recommendations. *Abdominal Radiology*, 42: 90-100.
20. Xiao Y-D, Paudel R, Liu J, Ma C, Zhang Z-S, Zhou S-K. (2016) MRI contrast agents: Classification and application. *International journal of molecular medicine*, 38: 1319-1326.
21. Muskula PR, Main ML. (2017) Safety with echocardiographic contrast agents. *Circulation: Cardiovascular Imaging*, 10: e005459.
22. Zheng J, Jaffray DA, Allen C. Nanosystems for multimodality in vivo imaging. In: *Multifunctional Pharmaceutical Nanocarriers*. Springer, 2008: 409-430.
23. Key J, Leary JF. (2014) Nanoparticles for multimodal in vivo imaging in nanomedicine. *International journal of nanomedicine*, 9: 711.
24. Chance B. (1991) Optical method. *Annu Rev Biophys Biophys Chem*, 20: 1-28.

25. Wang C, Wang Z, Zhao T, Li Y, Huang G, Sumer BD, Gao J. (2018) Optical molecular imaging for tumor detection and image-guided surgery. *Biomaterials*, 157: 62-75.
26. Demos SG, Gandour-Edwards R, Ramsamooj R, de Vere White R. (2004) Near-infrared autofluorescence imaging for detection of cancer. *Journal of biomedical optics*, 9: 587-592.
27. Van de Ven SM, Elias SG, Wiethoff AJ, Van der Voort M, Nielsen T, Brendel B, Bontus C, Uhlemann F, Nachabe R, Harbers R. (2009) Diffuse optical tomography of the breast: preliminary findings of a new prototype and comparison with magnetic resonance imaging. *European radiology*, 19: 1108-1113.
28. Kosaka N, Ogawa M, Choyke PL, Kobayashi H. (2009) Clinical implications of near-infrared fluorescence imaging in cancer. *Future Oncol*, 5: 1501-1511.
29. Welzel J. (2001) Optical coherence tomography in dermatology: a review. *Skin Research and Technology: Review article*, 7: 1-9.
30. Ntziachristos V, Bremer C, Weissleder R. (2003) Fluorescence imaging with near-infrared light: new technological advances that enable in vivo molecular imaging. *European radiology*, 13: 195-208.
31. FDA U. (2006) guidance for industry, investigators and reviewers: exploratory IND studies. US Department of Health and Human Services [www.fda.gov/downloads/Drugs/GuidanceComplianceRegulatoryInformation/Guidances/UCM078933.pdf](http://www.fda.gov/downloads/Drugs/GuidanceComplianceRegulatoryInformation/Guidances/UCM078933.pdf) (Accessed March 2010).
32. Vahrmeijer AL, Hutteman M, Van Der Vorst JR, Van De Velde CJ, Frangioni JV. (2013) Image-guided cancer surgery using near-infrared fluorescence. *Nature reviews Clinical oncology*, 10: 507-518.
33. Nguyen QT, Tsien RY. (2013) Fluorescence-guided surgery with live molecular navigation: a new cutting edge. *Nature reviews cancer*, 13: 653-662.
34. Pellico J, Gawne PJ, de Rosales RT. (2021) Radiolabelling of nanomaterials for medical imaging and therapy. *Chemical Society Reviews*, 50: 3355-3423.
35. Xu W, Riikonen J, Nissinen T, Suvanto M, Rilla K, Li B, Wang Q, Deng F, Lehto V-P. (2012) Amine surface modifications and fluorescent labeling of thermally



- stabilized mesoporous silicon nanoparticles. *The Journal of Physical Chemistry C*, 116: 22307-22314.
36. Naeini AT, Adeli M, Vossoughi M. (2010) Poly (citric acid)-block-poly (ethylene glycol) copolymers: new biocompatible hybrid materials for nanomedicine. *Nanomedicine: Nanotechnology, Biology and Medicine*, 6: 556-562.
  37. Zhang L, Wang Y, Tang Y, Jiao Z, Xie C, Zhang H, Gu P, Wei X, Yang G-Y, Gu H. (2013) High MRI performance fluorescent mesoporous silica-coated magnetic nanoparticles for tracking neural progenitor cells in an ischemic mouse model. *Nanoscale*, 5: 4506-4516.
  38. Di W, Ren X, Zhao H, Shirahata N, Sakka Y, Qin W. (2011) Single-phased luminescent mesoporous nanoparticles for simultaneous cell imaging and anticancer drug delivery. *Biomaterials*, 32: 7226-7233.
  39. Guo Z, Cui Z. (2021) *Fluorescent nanotechnology for in vivo imaging*. Wiley Interdisciplinary Reviews: Nanomedicine and Nanobiotechnology, 13: e1705.
  40. Horobin R, Kiernan J. *Conn's biological stains: a handbook of dyes, stains and fluorochromes for use in biology and medicine*. Taylor & Francis 2020.
  41. Bancroft JD, Gamble M. *Theory and practice of histological techniques*. Elsevier health sciences 2008.
  42. Kathiravan A, Anbazhagan V, Jhonsi MA, Renganathan R. (2008) A study on the fluorescence quenching of Eosin by certain organic dyes. *Zeitschrift für Physikalische Chemie*, 222: 1013-1021.
  43. Kathiravan A, Anbazhagan V, Jhonsi MA, Renganathan R. (2007) Fluorescence quenching of xanthene dyes by TiO<sub>2</sub>. *Zeitschrift für Physikalische Chemie*, 221: 941-948.
  44. Birtalan E, Rudat B, Kölmel DK, Fritz D, Vollrath SB, Schepers U, Bräse S. (2011) K p x g u v k i c v k p i " t j q f c o k p g " D n c d g n g f " r g r v q k applications. *Peptide Science*, 96: 694-701.
  45. Lakhil L, Acha V, Aussenac T. (2014) Resolution of fluorophore mixtures in biological media using fluorescence spectroscopy and Monte Carlo simulation. *Applied spectroscopy*, 68: 697-711.

46. Fisher P. (1999) Review of using Rhodamine B as a marker for wildlife studies. *Wildlife Society Bulletin*: 318-329.
47. E y c n k p u m k " V . " R q n q o " Y . " O c t c A p C w a l i n a . N , T q x k g n m  
Matuszewski M, Roviello F, Jaskiewicz J, Polom K. (2020) Methylene blueô current knowledge, fluorescent properties, and its future use. *Journal of Clinical Medicine*, 9: 3538.
48. Pahang F, Parvin P, Ghafoori-Fard H, Bavali A, Moafi A. (2020) Fluorescence properties of methylene blue molecules coupled with metal oxide nanoparticles. *OSA Continuum*, 3: 688-697.
49. WHO. (2019) World Health Organization model list of essential medicines, 21st list, 2019. Geneva: World Health Organization; 2019. Licence: CC BY-NC-SA 3.0 IGO.
50. Wagner M, Suarez E, Theodoro T, Machado Filho C, Gama M, Tardivo J, Paschoal F, Pinhal M. (2012) Methylene blue photodynamic therapy in malignant melanoma decreases expression of proliferating cell nuclear antigen and heparanases. *Clinical and Experimental Dermatology: Experimental dermatology*, 37: 527-533.
51. Fernandez-Fernandez A, Manchanda R, Lei T, Carvajal DA, Tang Y, Kazmi SZR, McGoron AJ. (2012) Comparative study of the optical and heat generation properties of IR820 and indocyanine green. *Molecular imaging*, 11: 7290.2011. 00031.
52. Topaloglu N, Gulsoy M, Yuksel S. (2013) Antimicrobial photodynamic therapy of resistant bacterial strains by indocyanine green and 809-nm diode laser. *Photomedicine and laser surgery*, 31: 155-162.
53. Kaur M, Mandl GA, Maurizio SL, Tessitore G, Capobianco JA. (2022) On the photostability and luminescence of dye-sensitized upconverting nanoparticles using modified IR820 dyes. *Nanoscale Advances*, 4: 608-618.
54. Prajapati SI, Martinez CO, Bahadur AN, Wu IQ, Zheng W, Lechleiter JD, McManus LM, Chisholm GB, Michalek JE, Shireman PK. (2009) Near-infrared imaging of injured tissue in living subjects using IR-820. *Molecular imaging*, 8: 7290.2009. 00005.
55. Gupta RC. *Handbook of toxicology of chemical warfare agents*. Academic Press 2015.

56. Szigeti K, Hegedus N, Racz K, Horvath I, Veres DS, Szollosi D, Futo I, Modos K, Bozo T, Karlinger K, Kovacs N, Varga Z, Babos M, Budan F, Padmanabhan P, Gulyas B, Mathe D. (2018) Thallium Labeled Citrate-Coated Prussian Blue Nanoparticles as Potential Imaging Agent. *Contrast Media Mol Imaging*, 2018: 2023604.
57. Shokouhimehr M, Soehnen ES, Hao J, Griswold M, Flask C, Fan X, Basilion JP, Basu S, Huang SD. (2010) Dual purpose Prussian blue nanoparticles for cellular imaging and drug delivery: a new generation of T1-weighted MRI contrast and small molecule delivery agents. *Journal of Materials Chemistry*, 20: 5251-5259.
58. Namazi H, Adeli M. (2005) Dendrimers of citric acid and poly (ethylene glycol) as the new drug-delivery agents. *Biomaterials*, 26: 1175-1183.
59. Perrier M, Busson M, Massasso G, Long J, Boudousq V, Pouget J-P, Peyrottes S, Perigaud C, Porredon-Guarch C, de Lapuente J. (2014) 201 Tl+-labelled Prussian blue nanoparticles as contrast agents for SPECT scintigraphy. *Nanoscale*, 6: 13425-13429.
60. Moorthy MS, Hoang G, Subramanian B, Bui NQ, Panchanathan M, Mondal S, Tuong VPT, Kim H, Oh J. (2018) Prussian blue decorated mesoporous silica hybrid nanocarriers for photoacoustic imaging-guided synergistic chemo-photothermal combination therapy. *Journal of Materials Chemistry B*, 6: 5220-5233.
61. Long J, Guari Y, Guerin C, Larionova J. (2016) Prussian blue type nanoparticles for biomedical applications. *Dalton Trans*, 45: 17581-17587.
62. Peng J, Dong M, Ran B, Lk " Y . " J c q " [ . " [ c p i " S . " V c p -" N . " U j k ' for-c n-työ, biodegradable prussian blue/manganese dioxide hybrid nanocrystal for trimodal imaging-guided photothermal therapy and oxygen regulation of breast cancer. *ACS applied materials & interfaces*, 9: 13875-13886.
63. Cook JR, Dumani DS, Kubelick KP, Luci J, Emelianov SY. Prussian blue nanocubes: multi-functional nanoparticles for multimodal imaging and image-guided therapy (Conference Presentation). In: *Photons Plus Ultrasound: Imaging and Sensing 2017* Vol. 10064. SPIE, 2017: 269-269.

64. Jing L, Liang X, Deng Z, Feng S, Li X, Huang M, Li C, Dai Z. (2014) Prussian blue coated gold nanoparticles for simultaneous photoacoustic/CT bimodal imaging and photothermal ablation of cancer. *Biomaterials*, 35: 5814-5821.
65. Bhavesh R, Lechuga-Vieco AV, Ruiz-Cabello J, Herranz F. (2015) T1-MRI fluorescent iron oxide nanoparticles by microwave assisted synthesis. *Nanomaterials*, 5: 1880-1890.
66. Rosado-de-Castro PH, Morales MdP, Pimentel-Coelho PM, Mendez-Otero R, Herranz F. Development and application of nanoparticles in biomedical imaging. Vol. 2018. Hindawi, 2018.
67. Westbrook C, Talbot J. MRI in Practice. John Wiley & Sons 2018.
68. Bulte JW, Kraitchman DL. (2004) Iron oxide MR contrast agents for molecular and cellular imaging. *NMR in Biomedicine: An International Journal Devoted to the Development and Application of Magnetic Resonance In Vivo*, 17: 484-499.
69. Babes L, Denizot B, Tanguy G, Le Jeune JJ, Jallet P. (1999) Synthesis of iron oxide nanoparticles used as MRI contrast agents: a parametric study. *Journal of colloid and interface science*, 212: 474-482.
70. Pöhlert E, Kloust H, Tromsdorf U, Janschel M, Hahn C, Maßlo C, Weller H. (2012) Relaxivity optimization of a PEGylated iron-oxide-based negative magnetic resonance contrast agent for T2-weighted spin-echo imaging. *ACS Nano*, 6: 1619-1624.
71. Cunningham CH, Arai T, Yang PC, McConnell MV, Pauly JM, Conolly SM. (2005) Positive contrast magnetic resonance imaging of cells labeled with magnetic nanoparticles. *Magnetic Resonance in Medicine: An Official Journal of the International Society for Magnetic Resonance in Medicine*, 53: 999-1005.
72. Xiao N, Gu W, Wang H, Deng Y, Shi X, Ye L. (2014) T1/T2 dual-modal MRI of brain gliomas using PEGylated Gd-doped iron oxide nanoparticles. *Journal of colloid and interface science*, 417: 159-165.
73. Hu F, Zhao YS. (2012) Inorganic nanoparticle-based T1 and T1/T2 magnetic resonance contrast probes. *Nanoscale*, 4: 6235-6243.

74. \ j q w " \ . " N w " \ T 0 " \* 4 2 contrast agents for magnetic resonance cancer imaging. Wiley Interdisciplinary Reviews: Nanomedicine and Nanobiotechnology, 5: 1-18.
75. Aime S, Botta M, Terreno E. (2005) Gd (III)-based contrast agents for MRI. Adv Inorg Chem, 57: 173-237.
76. Merbach AS, Helm L, Toth E. The chemistry of contrast agents in medical magnetic resonance imaging. John Wiley & Sons 2013.
77. Rogosnitzky M, Branch S. (2016) Gadolinium-based contrast agent toxicity: a review of known and proposed mechanisms. Biometals, 29: 365-376.
78. Ventola CL. (2012) The nanomedicine revolution: part 1: emerging concepts. P T, 37: 512-525.
79. Buser H, Schwarzenbach D, Petter W, Ludi AJIC. (1977) The crystal structure of Prussian blue:  $\text{Fe}_4 [\text{Fe} (\text{CN})_6]_3 \cdot x\text{H}_2\text{O}$ . 16: 2704-2710.
80. Gautam M, Poudel K, Yong CS, Kim JO. (2018) Prussian blue nanoparticles: Synthesis, surface modification, and application in cancer treatment. Int J Pharm, 549: 31-49.
81. Liang X, Deng Z, Jing L, Li X, Dai Z, Li C, Huang M. (2013) Prussian blue nanoparticles operate as a contrast agent for enhanced photoacoustic imaging. Chemical communications, 49: 11029-11031.
82. Wu Y, Yang H, Shin HJ. (2014) Encapsulation and crystallization of Prussian blue nanoparticles by cowpea chlorotic mottle virus capsids. Biotechnol Lett, 36: 515-521.
83. Samain L, Grandjean F, Long GJ, Martinetto P, Bordet P, Strivay DJTJoPCC. (2013) Relationship between the synthesis of Prussian blue pigments, their color, physical properties, and their behavior in paint layers. 117: 9693-9712.
84. Adhikamsetty R, Jonnalagadda SJBotCSoE. (2009) Kinetics and mechanism of prussian blue formation. 23: 47-54.
85. Fernandes R, Dumont MF, Sze RW, Conklin LS, Hoffman HA, Jaiswal JK. Prussian blue-inspired constructs for multimodal imaging and therapy. Google Patents, 2017.

86. Fu G, Liu W, Feng S, Yue X. (2012) Prussian blue nanoparticles operate as a new generation of photothermal ablation agents for cancer therapy. *Chem Commun (Camb)*, 48: 11567-11569.
87. Máthé D, Szigeti K. Prussian blue based nanoparticle as multimodal imaging contrast material. Google Patents, 2014.
88. J g i g f u " P . " H q t i a e j " N . " M k u u " D . " X c t i c " \ . " L g Padmanabhan P, Gulyás B. (2022) Synthesis and preclinical application of a Prussian blue-based dual fluorescent and magnetic contrast agent (CA). *PloS one*, 17: e0264554.
89. H q t i a e j " N . " J g i g f u " P . " J q t x a v j " K . " M k u u " D . " Padmanabhan P, Szigeti K. (2020) Fluorescent, Prussian Blue-Based Biocompatible Nanoparticle System for Multimodal Imaging Contrast. *Nanomaterials*, 10: 1732.
90. Hoo CM, Starostin N, West P, Mecartney ML. (2008) A comparison of atomic force microscopy (AFM) and dynamic light scattering (DLS) methods to characterize nanoparticle size distributions. *Journal of Nanoparticle Research*, 10: 89-96.
91. Eaton P, Quaresma P, Soares C, Neves C, De Almeida M, Pereira E, West P. (2017) A direct comparison of experimental methods to measure dimensions of synthetic nanoparticles. *Ultramicroscopy*, 182: 179-190.
92. Walker HK, Hall WD, Hurst JW. (1990) *Clinical methods: the history, physical, and laboratory examinations*.
93. Rohrer M, Bauer H, Mintorovitch J, Requardt M, Weinmann H-J. (2005) Comparison of magnetic properties of MRI contrast media solutions at different magnetic field strengths. *Investigative radiology*, 40: 715-724.
94. Zhang Y-N, Poon W, Tavares AJ, McGilvray ID, Chan WC. (2016) Nanoparticle liver interactions: cellular uptake and hepatobiliary elimination. *Journal of controlled release*, 240: 332-348.
95. Quini CC, Próspero AG, Calabresi MF, Moretto GM, Zufelato N, Krishnan S, Pina DR, Oliveira RB, Baffa O, Bakuzis AF. (2017) Real-time liver uptake and biodistribution of magnetic nanoparticles determined by AC biosusceptometry. *Nanomedicine: Nanotechnology, Biology and Medicine*, 13: 1519-1529.

96. Zhang D, Zhang J, Li Q, Tian H, Zhang N, Li Z, Luan Y. (2018) pH-and enzyme-sensitive IR8206paclitaxel conjugate self-assembled nanovehicles for near-infrared fluorescence imaging-guided chemoóphotothermal therapy. *ACS applied materials & interfaces*, 10: 30092-30102.
97. Huang C, Hu X, Hou Z, Ji J, Li Z, Luan Y. (2019) Tailored graphene oxide-doxorubicin nanovehicles via near-infrared dye-lactobionic acid conjugates for chemo-photothermal therapy. *Journal of colloid and interface science*, 545: 172-183.
98. Chaurasia G. (2016) A review on pharmaceutical preformulation studies in formulation and development of new drug molecules. *International journal of Pharmaceutical sciences and research*, 7: 2313-2320.
99. Lau E. (2001) Preformulation studies. *Handbook of modern pharmaceutical analysis*, 3: 173-224.
100. Delvallée A, Feltin N, Ducourtieux S, Trabelsi M, Hocheplid J. (2015) Toward an uncertainty budget for measuring nanoparticles by AFM. *Metrologia*, 53: 41.
101. ADELINA B, Olivier C, KATRIN F, Vikram K, Gert R, ANDREE LM, Thomas L. (2011) Validation of Dynamic Light Scattering and Centrifugal Liquid Sedimentation Methods for Nanoparticle Characterisation.
102. Crouzier L, Delvallée A, Ducourtieux S, Devoille L, Noircler G, Ulysse C, Taché O, Barruet E, Tromas C, Feltin N. (2019) Development of a new hybrid approach combining AFM and SEM for the nanoparticle dimensional metrology. *Beilstein Journal of Nanotechnology*, 10: 1523-1536.
103. Baalousha M, Lead J. (2013) Characterization of natural and manufactured nanoparticles by atomic force microscopy: Effect of analysis mode, environment and sample preparation. *Colloids and Surfaces A: Physicochemical and Engineering Aspects*, 419: 238-247.
104. Horisberger M, Rosset J. (1977) Colloidal gold, a useful marker for transmission and scanning electron microscopy. *Journal of Histochemistry & Cytochemistry*, 25: 295-305.
105. Pennycook SJ, Nellist PD. *Scanning transmission electron microscopy: imaging and analysis*. Springer Science & Business Media2011.

106. Spence JC. High-resolution electron microscopy. OUP Oxford 2013.
107. Inkson BJ. Scanning electron microscopy (SEM) and transmission electron microscopy (TEM) for materials characterization. In: Materials characterization using nondestructive evaluation (NDE) methods. Elsevier, 2016: 17-43.
108. Kirk S, Skepper J, Donald A. (2009) Application of environmental scanning electron microscopy to determine biological surface structure. *Journal of Microscopy*, 233: 205-224.
109. Griffiths PR, James A. De Haseth. Fourier transform infrared spectrometry. Vol. 171. John Wiley & Sons, 2007.
110. Harris DC, Bertolucci MD. Symmetry and spectroscopy: an introduction to vibrational and electronic spectroscopy. Courier Corporation 1989.
111. Christian GD, Dasgupta PK, Schug KA. Analytical chemistry. John Wiley & Sons 2013.
112. Skoog DA, West DM, Holler FJ, Crouch SR. Fundamentals of analytical chemistry. Cengage learning 2013.
113. Holder CF, Schaak RE. Tutorial on powder X-ray diffraction for characterizing nanoscale materials. Vol. 13. ACS Publications, 2019: 7359-7365.
114. File PD. (2001) International Centre for Diffraction Data (ICDD): Newtown Square, PA, USA.
115. Ok n q – g x k " O F . " N N q i c t t " O C O X . " R L q c j m – t k e " P N 0 " \* 4 2 3 5  
Optical Polarized Spectra (380-900 nm) of Methylene Blue Crystals on a Glass Surface. *International Journal of Spectroscopy*.
116. Canossa S, Bacchi A, Graiff C, Pelagatti P, Predieri G. Structural investigation by X-ray diffraction analysis on the behaviour of methylene blue towards transition metal anions.
117. Prasanthi D, Jagadish G, Aishwarya KL. (2019) Solid dispersions of fenofibrate: Comparison of natural and synthetic carriers. *Pharm Innov J*, 8: 42-50.
118. Cheng L, Gong H, Zhu W, Liu J, Wang X, Liu G, Liu Z. (2014) PEGylated Prussian blue nanocubes as a theranostic agent for simultaneous cancer imaging and photothermal therapy. *Biomaterials*, 35: 9844-9852.



119. Tempany CM, Jayender J, Kapur T, Bueno R, Golby A, Agar N, Jolesz FA. (2015) Multimodal imaging for improved diagnosis and treatment of cancers. *Cancer*, 121: 817-827.
120. Diao S, Blackburn JL, Hong G, Antaris AL, Chang J, Wu JZ, Zhang B, Cheng K, Kuo CJ, Dai H. (2015) Fluorescence imaging in vivo at wavelengths beyond 1500 nm. *Angewandte Chemie*, 127: 14971-14975.
121. Hong G, Zou Y, Antaris AL, Diao S, Wu D, Cheng K, Zhang X, Chen C, Liu B, He Y. (2014) Ultrafast fluorescence imaging in vivo with conjugated polymer fluorophores in the second near-infrared window. *Nature communications*, 5: 4206.
122. Timchalk C, Creim JA, Sukwarotwat V, Wiacek R, Addleman RS, Fryxell GE, Yantasee W. (2010) In Vitro and In Vivo Evaluation of a Novel Ferrocyanide Functionalized Nanoporous Silica Decorporation Agent for Cesium (Cs) in Rats. *Health physics*, 99: 420.
123. Peter C, Hongwan D, K pfer A, Lauterburg B. (2000) Pharmacokinetics and organ distribution of intravenous and oral methylene blue. *European journal of clinical pharmacology*, 56: 247-250.
124. Brady III CE, DiPalma JA, Morawski SG, Santa Ana CA, Fordtran JS. (1986) Urinary excretion of polyethylene glycol 3350 and sulfate after gut lavage with a polyethylene glycol electrolyte lavage solution. *Gastroenterology*, 90: 1914-1918.
125. Baumann A, Piel I, Hucke F, Sandmann S, Hetzel T, Schwarz T. (2019) Pharmacokinetics, excretion, distribution, and metabolism of 60-kDa polyethylene glycol used in BAY 94-9027 in rats and its value for human prediction. *European Journal of Pharmaceutical Sciences*, 130: 11-20.
126. Perrier M, Gallud A, Ayadi A, Kennouche S, Porredon C, Gary-Bobo M, Larionova J, Goze-Bac C, Zanca M, Garcia M, Basile I, Long J, de Lapuente J, Borr s M, Guari Y. (2015) Investigation of cyano-bridged coordination nanoparticles Gd(3+)/[Fe(CN)6](3-)/D-mannitol as T1-weighted MRI contrast agents. *Nanoscale*, 7: 11899-11903.

127. Souris JS, Lee CH, Cheng SH, Chen CT, Yang CS, Ho JA, Mou CY, Lo LW. (2010) Surface charge-mediated rapid hepatobiliary excretion of mesoporous silica nanoparticles. *Biomaterials*, 31: 5564-5574.
128. Liu Z, Davis C, Cai W, He L, Chen X, Dai H. (2008) Circulation and long-term fate of functionalized, biocompatible single-walled carbon nanotubes in mice probed by Raman spectroscopy. *Proc Natl Acad Sci U S A*, 105: 1410-1415.
129. Chen Y, Wu L, Wang Q, Wu M, Xu B, Liu X, Liu J. (2016) Toxicological evaluation of Prussian blue nanoparticles after short exposure of mice. *Human & experimental toxicology*, 35: 1123-1132.
130. Sitterberg J, Özçetin A, Ehrhardt C, Bakowsky U. (2010) Utilising atomic force microscopy for the characterisation of nanoscale drug delivery systems. *European Journal of Pharmaceutics and Biopharmaceutics*, 74: 2-13.
131. Noebauer-Huhmann IM, Szomolanyi P, Juras V, Kraff O, Ladd ME, Trattnig S. (2010) Gadolinium-Based Magnetic Resonance Contrast Agents at 7 Tesla: In Vitro T: 1: Relaxivities in Human Blood Plasma. *Investigative radiology*, 45: 554-558.

100 " D k d n k q i t c r j { " q h " v j g " e c p f k f c v g ø u " r w d n k e c v k

I. Publications related to the topic of the Ph.D. thesis

H q t i <sup>a</sup> e j " N <sup>a</sup> u | n » . " J g i g f u " P k m q n g v N<sup>o</sup>émi," Vargat x <sup>a</sup> v j " K

Zoltán, Jakab Géza, Kovács Tibor, Padmanabhan Parasuraman, Szigeti Krisztián, Máthé Domokos Fluorescent, Prussian Blue-Based Biocompatible Nanoparticle System for Multimodal Imaging Contrast NANOMATERIALS 10: 9 Paper: 1732, 15 p. (2020) Szakcikk (Folyóiratcikk) | Tudományos Scopus - Chemical Engineering (miscellaneous) SJR indikátor: Q1 Scopus - Materials Science (miscellaneous) SJR indikátor: Q1 IF: 5,076

J g i g f u <sup>h</sup>, F~~org~~ách László<sup>l</sup>, Kiss Bálint<sup>l</sup>, Varga Zoltán<sup>l</sup>, Jezsó Bálint<sup>l</sup>, Horváth Ildikó, Kovács Noémi<sup>l</sup>, Hajdrik Polett<sup>l</sup>, Padmanabhan Parasuraman, Gulyás Balázs, Szigeti Krisztián, Máthé Domokos Synthesis and preclinical application of a Prussian blue-based dual fluorescent and magnetic contrast agent (CA) PLOS ONE 17: 7 Paper: e0264554, 15 p. (2022) Szakcikk (Folyóiratcikk) | Tudományos Scopus - Multidisciplinary SJR indikátor: Q1 3 O g i q u | v q v v " u | g t | m " K H < " 5 . 9 7 4 ,

Forgách László, Kiss-Hegedus Nikolett, Horváth Ildikó, Szigeti Krisztián, Máthé Domokos Prussian blue nanoparticles: an advanced platform for multimodal imaging BIOPHYSICAL JOURNAL 121: 3 pp. 425a-426a. (2022) Absztrakt / Kivonat (Folyóiratcikk) | Tudományos

II.. Publications not related to the top of the Ph.D. thesis

Mathe Domokos, Kiss Balint, Palyi Bernadett, Kis Zoltan, Forgach Laszlo, Hegedus Nikolett, Varga Zoltan, Szigeti Krisztian, Karlinger Kinga, Kellermayer Miklos S. Z. The 3M Concept: Biomedical Translational Imaging from Molecules to Mouse to Man EUROBIOTECH JOURNAL 5: 3 pp. 155-160. (2021) Szakcikk (Folyóiratcikk) | Tudományos

Omer Safaa, Forgách László, Zelkó Romána, Sebe István Scale-up of Electrospinning: Market Overview of Products and Devices for Pharmaceutical and Biomedical Purposes PHARMACEUTICS 13: 2 Paper: 286, 21 p. (2021) Összefoglaló cikk (Folyóiratcikk) | Tudományos IF: 6,525

Központi Könyvtár igazolása:

I. Az értekezés témájában megjelent eredeti közlemények összesített impaktfaktor

értéke: 8,828

II. Egyéb ó nem az értekezés témájában megjelent ó eredeti közlemények összesített

impaktfaktor értéke: 6,525

I.+II. A könyvtári adatlapon feltüntetett közlemények összesített impaktfaktor értéke:

15,353

## 11. Acknowledgements

Foremost, I would like to express my sincere gratitude to my supervisor, Dr Krisztián Szigeti, who guided me throughout this project

A debt of gratitude is also owed to Dr. Nikolett Kiss-J g i g and Dr. Domokos Máthé; without their help this study would not have been successfully completed.

This disquisition would not have been possible without the kind and generous support of the Head of the Department, Miklós Kellermayer. Without his contribution, most of my measurements have not been possible.

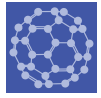
I would like to thank the following people for helping with this research project:

Zoltán Varga for his help with TEM measurements and Ildikó Horváth for the help and assistance during the in vivo measurements and imaging.

Representatives from Department of Pharmacy of Semmelweis University, for their willingness to impart their knowledge Co-workers, at the Department of Biophysics and Radiation Biology, for their help, guidance, comments, which helped the formation of a supportive and productive environment for all the research and scientific work, formulating a real scientific workshop, for me, as a young researcher.



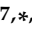
For the useful, thought-provoking questions and detailed suggestions to my reviewers and Teachers, to Levente Herényi and István Voszka.

Last but not the least I would like to thank my friends and family who supported me and encouraged me gathering deep insight into the study.



Article

# Fluorescent, Prussian Blue-Based Biocompatible Nanoparticle System for Multimodal Imaging Contrast

László Forgách <sup>1,\*</sup>, Nikolett Hegedűs <sup>1</sup>, Ildikó Horváth <sup>1</sup>, Bálint Kiss <sup>1</sup>, Noémi Kovács <sup>1</sup>, Zoltán Varga <sup>1,2</sup>, Géza Jakab <sup>3</sup>, Tibor Kovács <sup>4</sup>, Parasuraman Padmanabhan <sup>5</sup> , Krisztián Szigeti <sup>1,\*</sup>  and Domokos Máthé <sup>1,6,7,\*</sup> 

- <sup>1</sup> Department of Biophysics and Radiation Biology, Semmelweis University, 1085 Budapest, Hungary; hegedus.nikolett@med.semmelweis-univ.hu (N.H.); horvath.ildiko@med.semmelweis-univ.hu (I.H.); kiss.balint@med.semmelweis-univ.hu (B.K.); kovacsnoi@hotmail.com (N.K.); varga.zoltan@ttk.mta.hu (Z.V.)
- <sup>2</sup> Institute of Materials and Environmental Chemistry, Research Centre for Natural Sciences, 1117 Budapest, Hungary
- <sup>3</sup> Department of Pharmaceutics, Semmelweis University, 1085 Budapest, Hungary; jakab.geza@pharma.semmelweis-univ.hu
- <sup>4</sup> Institute of Radiochemistry and Radioecology, University of Pannonia, 8200 Veszprém, Hungary; kt@almos.vein.hu
- <sup>5</sup> Lee Kong Chian School of Medicine, Nanyang Technological University, Singapore 636921, Singapore; ppadmanabhan@ntu.edu.sg
- <sup>6</sup> In Vivo Imaging Advanced Core Facility, Hungarian Centre of Excellence for Molecular Medicine, 6723 Szeged, Hungary
- <sup>7</sup> CROmed Translational Research Centers, 1047 Budapest, Hungary
- \* Correspondence: forgach.laszlo@med.semmelweis-univ.hu (L.F.); szigeti.krisztian@med.semmelweis-univ.hu (K.S.); mathe.domokos@med.semmelweis-univ.hu (D.M.); Tel.: +36-1-459-1500 (ext. 60164) (L.F.); +36-1-459-1500 (ext. 60210) (D.M.)
- † These authors contributed equally to this work.

Received: 16 July 2020; Accepted: 27 August 2020; Published: 31 August 2020



**Abstract:** (1) Background. The main goal of this work was to develop a fluorescent dye-labelling technique for our previously described nanosized platform, citrate-coated Prussian blue (PB) nanoparticles (PBNPs). In addition, characteristics and stability of the PB nanoparticles labelled with fluorescent dyes were determined. (2) Methods. We adsorbed the fluorescent dyes Eosin Y and Rhodamine B and methylene blue (MB) to PB-nanoparticle systems. The physicochemical properties of these fluorescent dye-labeled PBNPs (iron(II);iron(III);octadecacyanide) were determined using atomic force microscopy, dynamic light scattering, zeta potential measurements, scanning- and transmission electron microscopy, X-ray diffraction, and Fourier-transformation infrared spectroscopy. A methylene-blue (MB) labelled, polyethylene-glycol stabilized PBNP platform was selected for further assessment of in vivo distribution and fluorescent imaging after intravenous administration in mice. (3) Results. The MB-labelled particles emitted a strong fluorescent signal at 662 nm. We found that the fluorescent light emission and steric stabilization made this PBNP-MB particle platform applicable for in vivo optical imaging. (4) Conclusion. We successfully produced a fluorescent and stable, Prussian blue-based nanosystem. The particles can be used as a platform for imaging contrast enhancement. In vivo stability and biodistribution studies revealed new aspects of the use of PBNPs.

**Keywords:** Prussian blue nanoparticles; fluorescent imaging; optical imaging; biocompatible

## 1. Introduction

Optical methods are simple and easy ways of imaging in biomedical research. They offer opportunities from simple observation of subjects to advanced methods for the imaging of tumors and different metabolic pathways using different kinds of spectroscopy and microscopy [1]. The major drawback of this method lies in the properties of light: tissue absorption and scatter strongly depend on the wavelength of light as well as the tissues themselves. Strong autofluorescence of the highly perfused tissues, e.g., muscles, skin, and hair scatter limit the tissue penetration and contrast of optical methods. Fluorophores, emitting light at higher wavelengths can potentially result in a better signal-to-noise ratio and a better image [2–4]. On the other hand, fluorophores alone are not able to mark specific tissues; their premature metabolism after intravenous administration often leads to decreased uptake in the target tissue or tumor. Yet, their toxicity to the healthy tissues is another issue. To overcome these drawbacks, chemical or physicochemical solutions would connect these NIR fluorophores to other structures, e.g., nanoparticles or proteins, which could solve the toxicity and sensitivity issues, allowing the microdosing of these agents [4,5].

Mesoporous nanoparticles have been reported, capable of fluorescent optical imaging [6–9]. The mesoporous structure itself could lend the particle absorbing properties of ions, anticancer drug, or even fluorescent dyes to the corresponding particles [6–10]. However, the synthesis of such particles can range from a very wide range of chemical synthesis techniques from the polycondensation process to thermal oxidation to thermal condensation; the basics of nanoparticle separation via centrifugation, rinsing the samples using ethanol to remove “unwanted,” unreacted contaminants along with dialyzing the samples could be easily translated and implemented into any synthesis process [6,9].

Methylene blue, with its excitation wavelength at 633 nm and emission at 662 nm could be a potential candidate for fluorescent imaging. Its emission wavelength is in the diagnostic window (650–900 nm), where the extinction coefficients of oxyhemoglobin, deoxyhemoglobin, and water are the lowest [4]. Furthermore, methylene blue is on the World Health Organization List of Essential Medicines, the safest and most effective medicines needed in a health system and has been used widely in clinical and basic research [10,11]. Its properties and widespread global use make it a promising candidate for the fluorescent labelling of a multimodal imaging system, a Prussian blue nanoparticle-based nanoteragnostic agent (Prussian blue (PB) nanoparticles (PBNPs)).

Previous studies prove that PBNPs could possibly act as zeolitic and porous structures, absorbing metallic cations and gases in their pores, although the exact binding mechanisms were not fully described and published [12–14]. It was also previously reported that PBNPs could have a great potential as multimodal contrast agents as well as potential drugs for photodynamic therapy [7,13,15,16]. Equipped with a suitable biocompatible citrate layer would help to stabilize the particles and render them capable to form surface dendrimers when polyethylene glycols are added to the PBNP solution [7,12]. Just like with PEGylation, these surface dendrimers would prevent the aggregation of the nanosystem and provide long-term stability in physiological conditions [17,18].

Our main goal was to create a fluorescently labeled Prussian blue nanoparticle (PBNP) (iron(II); iron(III);octadecacyanide)-based nanosystem for preclinical fluorescent imaging. The crucial quality of the platform should be as follows: first, it should be a stable nanosystem, which does not aggregate over long periods of time; second, the emission of a fluorescent signal that could be detected in living organisms to make the particle suitable for *in vivo* imaging; and third, a clearance mechanism to reduce possible side effects but also to slow down accumulation in the monocyte-macrophage system, the liver and spleen. We wished to also take advantage of the biocompatible coating of the particle, thus connecting the potential fluorescent dyes and stabilizers to PBNPs. To this end, we selected and tested the fluorescent dyes eosin Y, rhodamine B, and methylene blue for further sorption to the PB nanoparticles, both with and without further (or preceding) PEGylation. We selected a 3-h imaging time point evaluation in order to model a clinically also relevant situation as in the case of currently running image-guided surgery clinical studies of fluorescent contrast materials.

## 2. Materials and Methods

### 2.1. Synthesis of PBNPs

Citrate-coated PBNPs were synthesized by following the method published by Shokouhimehr and colleagues with some modifications. [14]. Briefly, PBNPs were prepared by slowly adding 20 mL of 1.0 mM Fe(III) chloride anhydrous ( $\text{FeCl}_3$ ; Sigma-Aldrich, Budapest, Hungary) solution with 0.5 mmol of citric acid (Sigma-Aldrich) to a solution containing an equimolar amount of potassium ferrocyanide anhydrous ( $\text{K}_4[\text{Fe}(\text{CN})_6]$ ; Sigma-Aldrich, Budapest, Hungary) under vigorous stirring for 15 min at 40 °C. The products were isolated with centrifugation at 21,130 rcf (Eppendorf 5424R centrifuge) at 4 °C.

### 2.2. Fluorescent Labelling

Eosin Y and rhodamine B were adsorbed to the particles as reported in Supplementary Information (Table S1). For fluorescent labelling, the concentrated methylene blue (MB; Sigma-Aldrich) stock solution was diluted twofold and filtered through a 0.22  $\mu\text{m}$  membrane filter (MILLEX GP 0.22  $\mu\text{m}$ ; Merck Millipore Ltd., Budapest, Hungary). Further, 200  $\mu\text{L}$  of this filtered solution was added to 2 mL of the PBNP solution. This would result in adsorbed MB on the mesoporous surface of the biocompatible PBNPs. After that, two main approaches were made:

- a. The synthesized PBNPs were labelled after centrifugation of “bare” PBNPs at 4 °C, using 21,130 rcf. Thereafter, the PEGylation process was performed and the solution was dialyzed against phosphate buffer saline solution (pH = 6.8; Ph.Eur. 8.).
- b. The PBNP-MB mixture was centrifuged at 21,130 rcf (Eppendorf 5424R centrifuge) at 4 °C. Then, the PBNP-MBs were PEGylated, dialyzed, and stored at 2–8 °C until further use.

### 2.3. PEGylation of PBNPs

For the PEGylation, PEG 3000 (for molecular biology; Sigma Aldrich, Darmstadt, Germany) was available in monodisperse solution, while PEG 6000 (for synthesis) and PEG 8000 (for synthesis) (Sigma Aldrich, Budapest, Hungary) were commercially sold in solid form. At first, these power-based agents were dissolved in 50% ethanol–water mixture the final PEG content was set to 10 w/w%.

PBNP-MB solutions (2 mg/mL) were prepared by adding distilled water (Milli-Q) to the stock MB-labelled PBNP solution. After 15 min incubation time at room temperature, different PEG solutions (PEG 3000, PEG 6000, and PEG 8000) were added to the PBNP-MB solutions and dialyzed for 24 h (14 kDa filter) (Sigma-Aldrich, Budapest, Hungary) in phosphate buffer saline solution (pH = 6.8; Ph.Eur. 8.). Different v/v% concentration compositions (PEG 3000: 1.47-1.96-2.44-3.85-9.09, PEG 6000: 1.47-1.96-2.44-3.85, and PEG 8000: 1.47-1.96-2.44) were prepared and characterized in the following with DLS and Zetasizer instruments. Other details are available in the Supplemental Information.

### 2.4. DLS and Zeta Measurements

The absorbance of the samples was measured at 633 nm with a Model 8453 UV–VIS spectrophotometer (Agilent Technologies, Santa Clara, CA, USA). The surface charge and hydrodynamic diameter of the particles were determined using a Zetasizer Nano ZS (Malvern Instruments Ltd., Worcestershire, UK). DLS measurement was performed at 37 °C in backscattering mode (detector fixed at 173°) using a 633 nm He-Ne laser. Samples were measured in a reusable quartz cuvette (type PCS1115 6G; Malvern Instruments Ltd., Worcestershire, UK). Measurement of zeta potential was performed under similar conditions. DTS1070 disposable cuvettes were used (Malvern Instruments Ltd., Worcestershire, UK). The measurement data were evaluated using software provided by the manufacturer, and statistical data and graphs were created and evaluated with Origin 9.0 (OriginLab) and Microsoft Excel 2013 software. DLS measurements were performed weekly for a period of 6 weeks to determine colloidal stability. Samples were stored at 2–8 °C.



### 2.5. Atomic Force Microscopy (AFM)

After a 10 min incubation time, mica surface was dried in N<sub>2</sub> stream. AFM images were collected in noncontact mode with a Cypher S instrument (Asylum Research, Santa Barbara, CA, USA) at 1 Hz line-scanning rate in air, using a silicon cantilever (OMCL AC-160TS, Olympus, Tokyo, Japan) oscillated at its resonance frequency (300–320 MHz). Temperature during the measurements was  $25 \pm 1$  °C. AFM amplitude-contrast images are shown in this paper. The filter used on the images enhances the details of the height contrast images (violet, orange, yellow). AFM images were analyzed by using the built-in algorithms of the AFM driver software (Igor Pro, Wave Metrics Inc., Lake Oswego, OR, USA). Particle statistics was done by analyzing a  $4 \mu\text{m} \times 4 \mu\text{m}$  height-contrast image with ( $n = 95$ ) particles. Maximum height values were taken as the height of particles, and rectangularity was calculated as the ratio of the particle area to the area of a nonrotated inscribing rectangle. The closer a particle is to a rectangle, the closer this value is to unity. Detailed data is available in Supplemental Information Figure S5.

### 2.6. Scanning Electron Microscopy (SEM)

The nanoparticle suspension was diluted with distilled water (1:2) and applied to a metallic sample plate, which was covered with a double-sided carbon tape. The sample was dried under vacuum, metallized with gold and investigated with a field emission EM, JEOL JSM 6380LA SEM (Jeol Ltd., Tokyo, Japan), at 15 kV and a working distance of 15 mm. The morphology of the nanoparticles was observed.

### 2.7. Transmission Electron Microscopy (TEM)

Morphological investigations of the NPs were carried out on a JEOL JEM 1200EX (Jeol Ltd., Tokyo, Japan) transmission electron microscope. The diluted sample was dropped and dried on a carbon-coated copper grid. The length (along multiple axes) and the area of the particles were determined by manually measuring the diameter ( $n = 304$ ) and circumference ( $n = 176$ ) of the nanoparticles, using ImageJ software.

### 2.8. Animals

In vivo fluorescent imaging tests of MB-PBNP nanosystems were carried out in C57BL/6 male mice (Janvier, France). Animals had ad libitum access to food and water and were housed under temperature-, humidity-, and light-controlled conditions. All procedures were conducted in accordance with the ARRIVE guidelines and the guidelines set by the European Communities Council Directive (86/609 EEC) and approved by the Animal Care and Use Committee of Semmelweis University (protocol number: XIV-I-001/29-7/2012). Mice were 10–12 weeks old with an average body weight of  $28 \pm 5$  g. During imaging, animals were kept under anesthesia using a mixture of 2.5% isoflurane gas and medical oxygen. Their body temperature was maintained at 37 °C throughout imaging. For the most humane termination of the animals, intravenous Euthasol (pentobarbital/phenytoin) injection was used.

### 2.9. In Vivo Fluorescent Imaging

The fluorescent labelled PBNPs were imaged using a two-dimensional epifluorescent optical imaging instrument. (FOBITM, Fluorescent Organism Bioimaging Instrument; Neoscience Co., Ltd., Suwon-si, Korea). Mice were anesthetized with isoflurane (5% for induction and 1.5–2% to maintain the appropriate level of anesthesia; Baxter, AErrane). Precisely, 200  $\mu\text{L}$  of MB-labelled PBNP solution containing 224  $\mu\text{g}$  of Fe(III) in a 2 mg/mL concentration PBNP solution was administered intravenously into the tail vein. The images were collected (after shaving to remove hair) at 4 different time points (pre- and postinjection, 3 h postinjection, and ex vivo post the 3 h in vivo time) with excitation of 630–680 nm corresponding to the excitation maximum of the dye (ex: 664 nm; em: 687 nm).

The emission spectrum of the dye was in the pass band of the used emission filter. Image acquisition parameters were the following: exposure time: 1000 msec and gain: 1. The images were evaluated with VivoQuant software (Invicro, 27 Drydock Avenue, Boston, MA, USA).

### 3. Results

#### 3.1. Preformulation of PEGylated PBNPs

Multiple approaches were made to determine the optimal PEG coating concentration. For that, different volume-percent compositions were formed and characterized. During the preformulation, DLS measurements were performed and combined with the macroscopic analysis of the samples (aggregation, visual evaluation, homogeneity, and homogenizability) (Table S2).

We found that the optimal PEG concentration for the different types of PEG solutions is slightly different if the particle size and the PDI are the form factors for choice. For further inspections, PBNP-MB samples containing 5 mg (10  $\mu$ L) PEG 3000 (PNBP-MB@PEG3000\_10 $\mu$ L), 10 mg (100  $\mu$ L) PEG 6000 (PNBP-MB@PEG6000\_100 $\mu$ L), and 12.5 mg (100  $\mu$ L) PEG 8000 (PNBP-MB@PEG8000\_100 $\mu$ L) were chosen after DLS measurements and macroscopic inspections. The other samples showed either aggregation during the measurements or sedimented despite the optimal hydrodynamic diameter and low PDI value. The synthesized methylene-blue-labelled PEGylated PBNP-s (PBNP-MB@PEG) were stored at 2–8 °C.

#### 3.2. In Vitro Measurements

##### 3.2.1. DLS and Zeta Potential of Fluorescently Labelled PBNPs

MB labelled, PEGylated PBNPs were measured first to determine the optimal size. These measurements were part of a preformulation study, which included mainly macroscopic inspections along with DLS and zeta potential measurements (Supplemental Information, Table S2).

##### 3.2.2. Atomic Force Microscopy (AFM)

AFM images are shown in Figure 1. PBNPs appeared as objects with a flat rectangular surface protruding from a rounded halo (Figure 1a). The rectangular surface represents the real geometry of the particles (Figure 1c) while their halo is the consequence of tip convolution, i.e., the effect of imaging a rectangular prism by a tetrahedral AFM tip. Rectangularity of the particles (together with their halo) was found to be  $0.7701 \pm 0.1041$  (mean  $\pm$  SD), indicating that PBNPs indeed represent rectangular topography. The height of the particles showed monomodal distribution with a mean  $\pm$  SD of  $17.790 \pm 8.922$  nm (Figure 1).

##### 3.2.3. Scanning Electron Microscopy (SEM) and Transmission Electron Microscopy

Due to the sample preparation process, SEM images show an aggregated nanosystem where the particles appear as rectangular objects. Single particles were hard to distinguish from one another, however, their size did not exceed the 100 nm threshold (Figure 2a).

The nonhydrated shape and size of the NPs were also analyzed with TEM (Figure 2b,c). The nanosystem was slightly aggregated (Figure 2c), however, single particles could be observed. The shape of the nanoparticles on TEM and AFM images was similar. PBNPs appeared as flat rectangular, dense objects in this case as well. The average length of the particles was  $28.080 \pm 6.690$  (mean  $\pm$  SD;  $n = 304$ ) (Figure 2d), along with an average surface area of  $582.20 \pm 269.750$  nm<sup>2</sup> (mean  $\pm$  SD;  $n = 176$  particles) (Figure 2e).

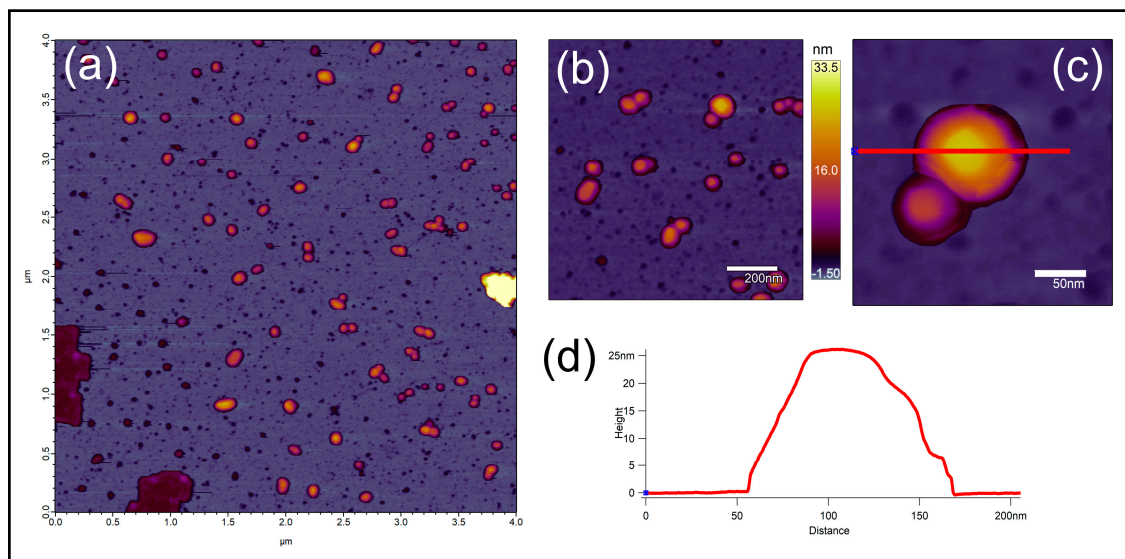


**Figure 1.** (a) Height-contrast AFM image of PBNPs on the mica surface (scale bar = 4  $\mu\text{m}$   $\times$  4  $\mu\text{m}$ ). (b) Modified PBNPs on the mica surface; height-contrast AFM image (scale bar = 200 nm). (c) A modified PBNP nanoparticle (scale bar = 50 nm). (d) The cross-section graph of (c) PBNP nanoparticle (abscissa = 0–200 nm; ordinate = 0–25 nm). AFM: atomic force microscopy; PBNPs: Prussian blue nanoparticles.

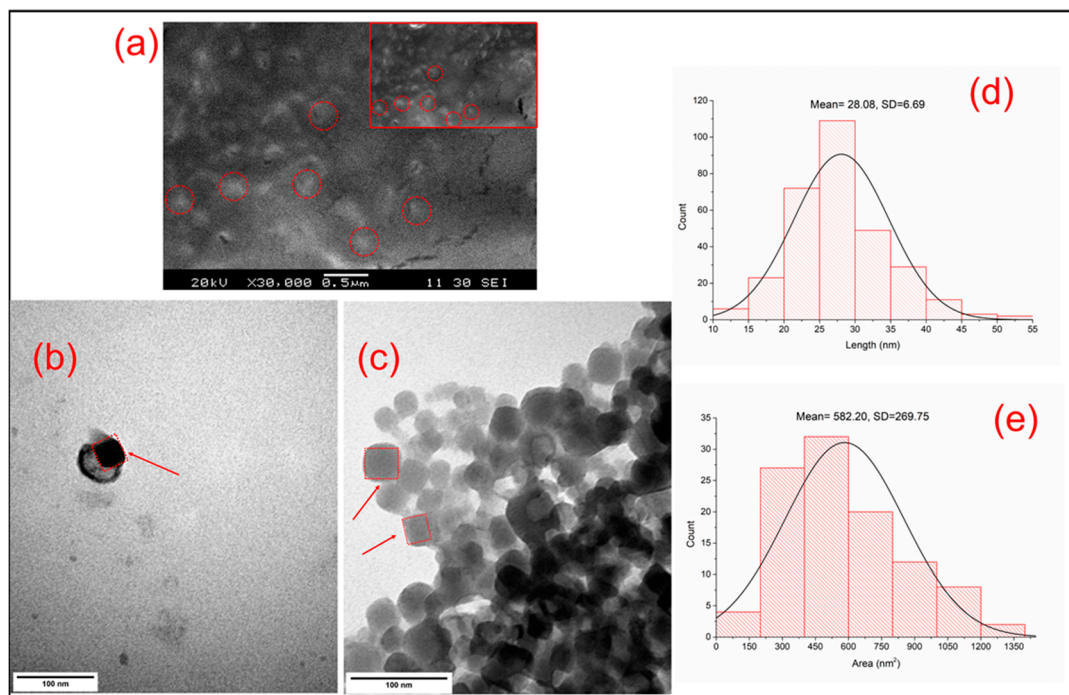


**Figure 2.** (a) The SEM micrograph of modified PBNPs (magnification: 30,000 $\times$ , scale bar = 0.5  $\mu\text{m}$ ); the PBNPs are barely visible between the pores of the double-sided carbon tape (section of (a); magnification: 30,000 $\times$ ). (b–c) The TEM micrograph of modified PBNPs (magnification = 250,000 $\times$ ; scale bar = 100 nm). (d) The mean length of PBNPs, determined by TEM images. (e) The average area of the modified PBNPs according to TEM images. SEM: scanning electron microscopy; PBNPs: Prussian blue nanoparticles; TEM transmission electron microscopy.

### 3.2.4. Measuring In Vitro Fluorescence

After the two main approaches of fluorescent labelling, PBNP-MB@PEGs were tested in vitro, to study whether the emitted signal is adequate for in vivo imaging. For that purpose, 20-fold diluted samples were produced and measured, along with the stock PBNP-MB@PEG solutions.

The samples prepared according to method a showed lower intensity on the emitted light, on the other hand, method b provided a significantly better signal in emission, which made the sample a better choice for in vivo use (Figure 3a,b).

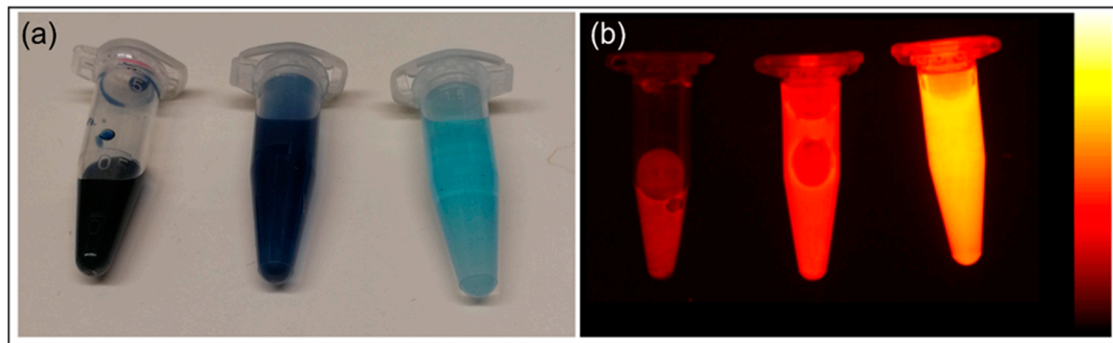


**Figure 3.** (a) PBNP-MB@PEG6000\_100µL (stock solution  $\times$  and 20 $\times$  dilution left to right). (b) Fluorescent signal of PBNP-MB@PEG6000\_100µL dilutions in FOBI. PBNP-MB@PEG6000\_100µL: Methylene blue-labelled (100 µL Methylene blue) PEG 6000 stabilized Prussian blue nanoparticles; FOBI: Fluorescent Organism Bioimaging Instrument.

### 3.2.5. Stability Measurements of PBNP-MB@PEG Nanoparticles

The mean zeta potential of the measured samples (PBNP, PBNP-MB@PEG3000, PBNP-MB@PEG6000, and PBNP-MB@PEG8000) was not bigger than  $-20$  mV, moreover, all the samples had a net negative charge of  $-25$  mV or greater.

The mean hydrodynamic diameter of the particles was measured as a part of a 4-week stability test. However, non-modified PBNPs size showed a slight change in the diameter, i.e., after the third week, all PEGylated particles started to aggregate. PBNP-MB@PEG6000 nanoparticles were the most stable, along with the lowest PDI and diameter. As the size (hydrodynamic diameter) of the other two particles (PBNP-MB@PEG3000 and PBNP-MB@PEG8000) doubled after 3 weeks, the PBNP-MB@PEG6000 particles kept a solid size of  $24.82 \pm 5.83$  nm (number-based particle size distribution). According to these results, PBNP-MB@PEG6000 particles remained stable for the longest time, thus made them the best candidate for further inspections (Supplemental Information; Table S3 and Figure S6)

### 3.3. In Vivo and Ex Vivo Measurements

Due to the strong visible fluorescent signal of PBNP-MB@PEG6000s, 200 µL of the suspension of nanoparticles was injected into the lateral tail vein of C57BL/6 male mice Figure 4A,B. The semiquantitative distribution of the labelled PBNPs was determined based on their normalized mean fluorescent intensity (Figure S6). On the ex vivo images Figure 4B, taken 3 h after the first injection, PBNP-MB@PEG6000 accumulation can be observed in the gastrointestinal tract, kidneys, spleen, liver, and heart.

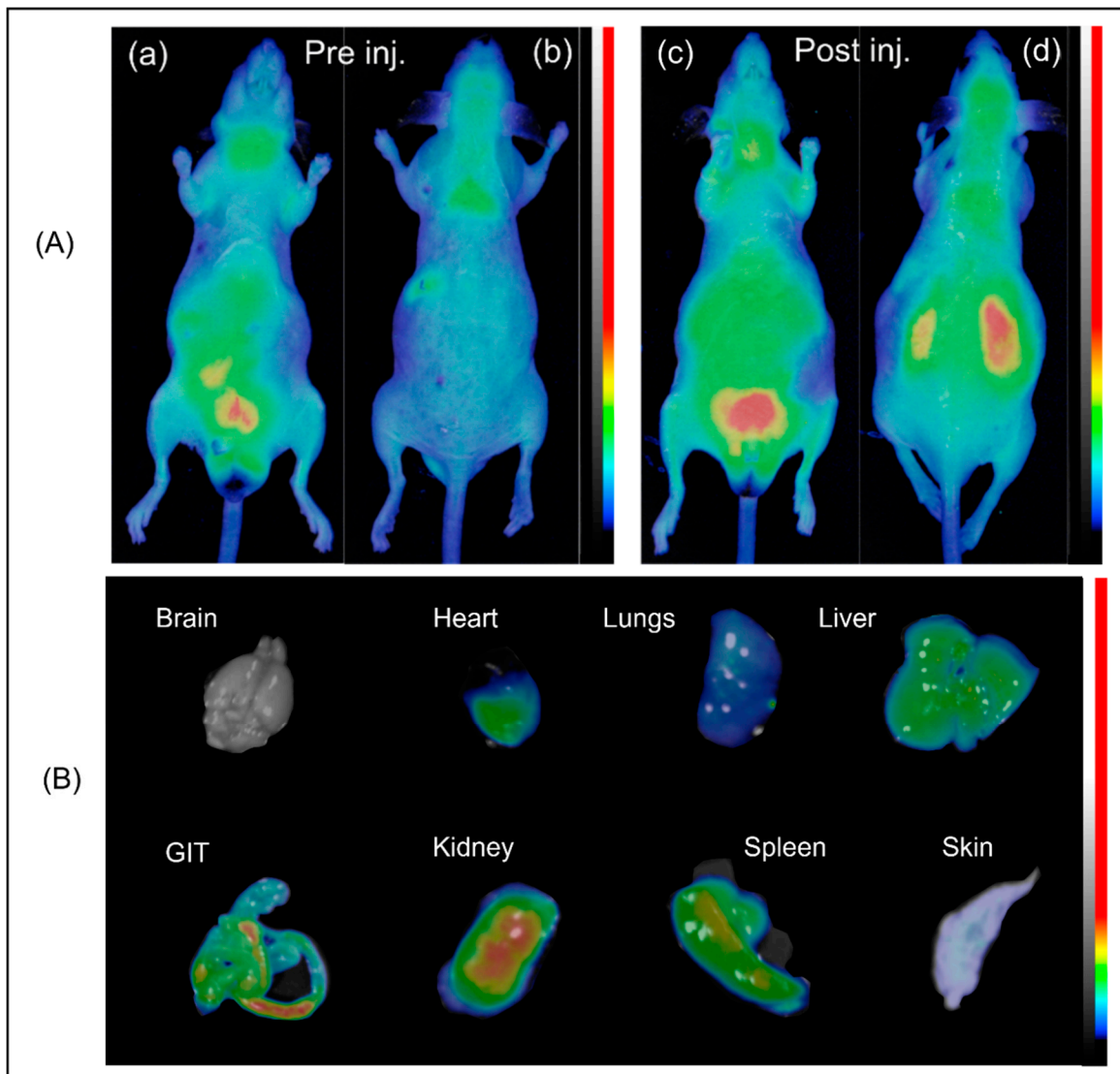


**Figure 4.** (A) (a,b) C57BL/6 mice before intravenous treatment from anterior and posterior planes. (c,d) C57BL/6 mice pre-PBNP treatment (anterior and posterior planes). (a) anterior, preinjection; (b) posterior, preinjection; (c) anterior, postinjection; and (d) posterior, postinjection. Color scale equals mean fluorescent intensity (MFI) in arbitrary units (A.U.) Figure 4 (B) ex vivo images, 3 h postinjection.

#### 4. Discussion

It has long been known that Prussian blue (PB) is capable of chelating toxic metals, e.g., cesium (Cs) and thallium (Tl), thus facilitating their clearance from the body. This property is the main reason PB is featured on the World Health Organization (WHO) Model List of Essential Medicines, as the specific category “Antidotes and other substances used in poisoning” PB has been approved for medical use in the United States (US) and in Europe for the abovementioned indication since 2003 [10,19]. Previous studies also described Prussian blue nanoparticles (PBNPs) as potential photothermal therapeutic agents [16], a promising candidate for different types of imaging [20], e.g., magnetic resonance-imaging (MRI) (as a T1 and T2 contrast agent) [12,21], optical imaging, and computed tomography [22]. The most widely used imaging modalities for follow-up studies are MRI and optical imaging (OI). MRI, based on the different relaxivities modulated by contrast agents (CA), is able to emphasize the structural (anatomical) differences between different types of tissues. MRI methods are noninvasive and can be easily translated from preclinical research to clinical applications, allowing the acquisition



of spatial as well as temporal information. However, MRI suffers from less than optimum sensitivity of detection of injected CAs [23].

Of the mentioned modalities, OI is, however, the least complicated and most versatile method in current preclinical imaging applications. OI is free from harmful effects of ionizing radiation—in fact, it replaces it with nonionizing radiation, which includes visible, ultraviolet, and infrared light [24].

Several approaches were made to synthesize multimodal nanoparticles, which were capable of optical imaging along with other imaging techniques or had notable therapeutic relevance. Dumont et al. described PBNP analogue Mn (II) containing fluorescent-labelled nanoparticles with pediatric brain tumor (PBT) specific antigens. These nanoparticles generated MRI contrast (in both T1 and T2) and showed specific uptake in PBTs due to their surface modifications. These modifications granted them biocompatibility and provided fluorescent signal in vivo [25].

Tu et al. has also described multimodal magnetic-resonance and optical-imaging contrast agent, which were sensitive to NADH. In the presence of NADH, the MRI signal enhanced, whereas the green fluorescence disappeared [26]. The contrast agent itself had a notable MR signal enhancement in vivo, the only drawback of its clinical application was the lack of specificity on a cellular level. Furthermore, the absorption peak of the molecule was found in the region of autofluorescence, which made it a less promising candidate for further use.

To overcome the weakness in OI, Shcherbo et al., in his work, has discussed a protein known as mKate/Katushka (monomer/polymer), which could be excited at 588 nm and emits at 635 nm. At the far-red emission wavelengths, neither the absorbance of hemoglobin and melanin at 620 nm nor the absorbance of water at 1100 nm is significant, thereby providing greater penetration depth for detection in vivo [27]. Due to the lack of selectivity in fluorescent signal, this technique could not succeed in preclinical drug research, notwithstanding its novelty in whole-body imaging and gene manipulation.

Despite other important results, Prussian blue nanoparticles were not yet been described as both fluorescent and PEGylated nanoscale platform for in vivo imaging. In our work, the fluorescence was provided with an adsorbed dye, namely, methylene blue (MB), which is a highly water-soluble fluorescent dye. MB is widely used in different fields of medicine: as the medication and treatment of methemoglobinemia and cyanide poisoning; as a part of combination of drugs in infection control, which covers the urinary tract; and as a stain or dye in different types of endoscopy [28–31].

In addition, the excitation of methylene blue is in the NIR region (above 630 nm). MB is also the most inexpensive of the commercially available NIR fluorescent dyes and has been widely used for bioanalysis [32]. Prussian blue nanoparticles were previously described as biosensors, based on their redox properties. Their peroxidase-like activity was in focus of the studies of Zhang et al. and Vázquez-González et al. Their studies suggest that the interaction of cells with PBNPs could enhance the effects of oxidative damage to cells, especially to the cells of the liver, which was observed in the work of Chen et al. [33–35]. To overcome the oxidative effects of PBNP administration, either reductive substance should be administered with the PBNPs or reductase-like activity should be attached to the surface of the PBNPs. Such reductive substances would prevent the effects of the PBNPs. MB is a strong antioxidant, which would prevent cellular oxidation damage as Zhang et al. describes, by preventing mitochondrial oxygen free radical formation and enhancing oxygen consumption [36]. Previous studies described MB as an encapsulated dye in different kinds of particles for fluorescent imaging [37,38]. In addition, Szigeti et al. and Chen et al. suggested that mesoporous PBNPs could act as “chemical sponges,” absorbing metal ions and drugs, depending on the pH conditions and properties of the PBNPs [13,39]. Our results suggest similar mechanisms for labelling. The two applied methods were mainly different: method a suggested a connection based on surface charges and secondary bonds, where PEG had an additional function as sealant, preventing MB leakage. In contrast, method b showed less fluorescence, which suggest less adsorbed dye and therefore, poor labelling efficacy. The surface of PBNPs was “sealed” before MB could connect to the particles, which resulted in increased dye-washout during dialysis.

Surface charge measurements have been concluded—they suggest a small decrease in the zeta potential after MB labelling (mean value before labelling  $<-30$  mV; mean value after the labelling  $<-25$  mV). In addition, additional surface charge measurements were concluded, on older samples. Their zeta potential did not exceed  $-20$  mV. Therefore, it is possible that the decreased surface charge is the result of the ionic interactions between the dye and the citrate surface. Nevertheless, it must not be forgotten, that the pH of the used buffer (Phosphate buffer saline pH 6.8) could also result a decreased zeta potential in the MB-labelled PBNP sample. Previous studies described citric acid-, PVP-, and PEG-coated PBNPs. These capping agents are biocompatible and act mainly as steric stabilizers, which enhance the colloidal stability of the particles and affect the size and shape of the nanoparticles [40–42].

Chelating properties of citric acid were previously reported; citrate forms complexes with metallic cations although, at physiological conditions, these complexes have no effect on the colloidal stability of the particles [43,44]. Both citric acid and PEG offer PBNPs biocompatibility, moreover, citrate as a capping agent could function as an anchor for different molecules due to its terminal carboxylic function. PEG and citric acid were reported to form aggregates, connected with  $\pi$ -bonds, depending on the concentration and the proportion of citric acid to PEG [17,18].

The reported PEGylated MB-labelled PBNPs remained stable for about 3 weeks, while the previously reported, citrate-coated PBNPs did not aggregate in a biologically relevant manner after 4 weeks [9,18]. This lets us conclude that the increased complexity on the nanoparticle surface leads to a shorter stability and usability. Based on the studies of Namazi et al. and Naeini et al., over time, citric acid and PEG are forming a self-aggregating system in our samples [7,15]. These dendrimers would offer a protective layer for PBNPs while encapsulating them along with the fluorescent dye MB. Our results suggest that further improvement would be necessary to synthesize a more stable PBNP platform for multimodal use as, e.g., MR-CA, radiotracer or therapeutic functions.

FTIR spectroscopy reveals the lengths of the bonds, the molecular mass changes, and the band-order of molecules. Hypsochromic shifts (shifts to lower wavenumbers) suggest that the mass of the corresponding molecule has been increased; the frequency of vibration is inversely proportional to mass of vibrating molecule. In addition, the absorption bands near  $3415$  and  $1610$   $\text{cm}^{-1}$  refer to the O–H stretching mode and H–O–H bending mode, respectively, indicating the presence of interstitial water in the samples (Figure S8a–d) [45–47].

In medical imaging, the safety and discomfort of patients are important; therefore, a significantly faster and safer method used for lengthy and repeated procedures could make a huge impact on both diagnostics and monitoring. Optical methods are peculiarly useful for visualizing soft tissues, which can be easily differentiated from each other based on their light-absorbing and -scattering capabilities. The dual modalities allow better chances for inspection, based on different kinds of imaging modalities, e.g., MRI and OI. Finally, if an acute intervention is required, the need of repeated CA administration could be preventable, if the half-life (and clearance) of the nanoteragnostic agent is adequate.

The total workings of the immune system play a significant role in the distribution, metabolism, and elimination of nanoparticles. As Diao et al. and Hong et al. used C57BL/6 mice of IR imaging, we also decided to test our nanosystem in C57BL/6 mice that have an intact immune system as opposed to immunocompromised nude mice [48,49]. This might have made our imaging signals more scattered, but increased the validity of the model towards, eventually, clinical translational studies.

The elimination and excretion of nanoparticles is, however, poorly investigated. Due to its mainly oral administration, only a few studies have been published data regarding I.V. PB administration. As far as we know, ultrasmall PBNPs tend to be excreted via glomerular pathways, while after oral administration, PBNPs are excreted via fecal and urine routes [13,50,51]. The few available reports dealing with biodistribution and elimination of PBNPs after intravenous injection are not conclusive. It would seem, though, that in those studies, kidney excretion was not relevant despite smaller PBNP deposits in the mesangium and the peritubular vessels of [13,15]. Our findings with the new coating and dye-adsorbed-modified PBNPs suggest that both kidney and biliary elimination routes play a

major role in the excretion of this nanoparticle system. Shortly after iv. administration, the particles could be found in the urinary tract, showing an enhanced fluorescent signal 3 h after the admission. This, along with our former data obtained with irreversibly  $^{201}\text{Tl}$ -isotope-labelled PBNPs passing through the kidney to the urinary excretion route, suggests a portion- of kidney excretion via fenestrae of the kidney endothelium and podocytes, especially in our measured hydrodynamic size range below 40 nm [13].

In order to account for eventual dissociation of the MB dye from PBNP surfaces, we compare the known elimination routes and dynamics of MB dye solution to our MB-labelled PBNPs. Peter et al. reported that while MB alone accumulates in the brain and bile, mainly urinary excretion is significant 1 h after IV administration. The maximal concentration during urinary excretion was reached 2–4 h after administration [52]. In this context, our results suggest that MB stayed bound to PBNPs as both renal clearances are prolonged while the PEG shell alone did not significantly increase the renal excretion speed. The fluorescent intensity in the heart, liver, and spleen suggest a prolonged circulation time. Significant uptake can be observed in the lungs ( $501\% \pm 85\%$ ; 2 h post injection  $156\% \pm 60\%$ ) and spleen ( $163\% \pm 18\%$ ), while a slight increase in fluorescent intensity in the intestines ( $107\% \pm 5\%$ ), along with the urinary excretion ( $272\% \pm 32\%$ ; 3 h post injection  $177\% \pm 20\%$ ) (percent values based on normalized fluorescent intensities preinjection  $\pm$  SD). These results suggest that the MB and PBNPs were connected, and their clearance followed the both characteristic pathways for MB and PBNP; furthermore, the PEG shell alone did not promote the renal excretion significantly. The fluorescent intensity in the heart, liver, and spleen suggest a prolonged circulation time (Figure S6).

The ex vivo images confirm that the application of PEG led to an increased biological half-life and slowed excretion rate, both biliary and urinary, compared to previous studies [53–55]. Even if other studies emphasize the connection between filtration and negative surface charge and larger particle size, PEGs are known as rather neutrally charged stabilizers. According to Liu et al. and Souris et al., complete clearance of PEG-modified nanoparticles last for 2 months, and thus, show a tendency of hepatic and renal accumulation causing local inflammation and necrotizing tissue [56,57].

Chen et al. investigated the acute and subchronic toxicological properties of Prussian blue nanoparticles after exposure of mice. PBNPs accumulated mainly in the spleen and liver. They found that, however, PBNPs induced acute damage in the liver (based on the liver functions), the long-term effects of PBNP-treatment cannot be called negative. All monitored parameters returned to normal levels, 60 days after the first IV PBNP administration [35]. Our results also confirm the claims of Chen et al.; in the ex vivo images (Figure 4), PBNPs were present in the spleen and the liver; biliary functions resulted in PBNP presence in the gastrointestinal tract.

The nontoxic properties of PBNPs were also confirmed by the study of Liang et al. Furthermore, they evince that no significant or fatal injury can be attributed to PBNP treatment, neither on histological nor on macroscopic matter. The vital organs were unharmed, no injuries were present on cellular levels 2 weeks and 4 weeks after the treatment [58].

Although fluorescent imaging capabilities of PBNPs were demonstrated in this work, further optimization and development of the platform is essential before any clinical implementation. Based on our work, the scale-up of PBNP-based CA is yet to be done while long-term studies for usability and effects in vivo are needed before human studies, too.

Our results suggest the use of PBNPs as a platform for the development of new-generation multimodal CAs, for OI and MRI imaging as well as therapeutic purposes. The biocompatible shell of the NPs is easy to modify due to the carboxylic groups, which would allow the cell or tissue targeted delivery. The targetable magnetic properties of the NPs would allow their theragnostic use, too, with proper selection of effector payload such as antibodies; thus, allowing a new type of topical infection-control method against bacterial and viral infections.

Such a NP system would act as CA in vivo as well as as a therapeutic agent for photothermal, isotope-based, biological or stem cell therapies, opening new aspects in the future of medicine.



## 5. Conclusions

In this work, we demonstrated a synthesis and modification methodology to biocompatible stealth fluorescent PBNPs. We created a novel nanoparticulate contrast material for the classical methodology of fluorescent measurements, e.g., using FOBI. Our results suggest that the stealth-liposome-like platform is suitable for fluorescent imaging.

We investigated the PB nanoobjects in vivo after intravenous admission and examined the elimination routes of these particles. We described the hepatobiliary and renal uptake and excretion to be both important in our system with in vivo intravenous application.

With both PEGylation and fluorescent labelling PB nanoparticles can be conferred with advanced technological properties to offer a finely tuned platform for clinical application after further development. We aim towards clinical translation hence the application of MB and NIR wavelength usage too. As fluorescent detection and imaging data in a suboptimal in vivo system are more convincing to extend towards human clinical trials, the use of standard and more clinically valid Black mice might have been a better choice for validity and detection studies than transparent but less clinically translatable nude mouse study.

**Supplementary Materials:** The following are available online at <http://www.mdpi.com/2079-4991/10/9/1732/s1>, Figure S1. (a) Fluorescein solution, imaged in the FOBI device. (b) Eosine Y solution, imaged in the FOBI device. (c) Rhodamine B solution, image in the FOBI device, Table S1. Previous approaches made for labelling PBNPs with fluorescent dyes, Figure S2. Ex vivo results of Eosine Y labelled PBNPs, Figure S3. Methylene blue labelled unpegylated PBNPs, in vivo, Figure S4. Methylene blue labelled PBNPs, ex vivo, Table S2. The detailed data of the preformulation measurements, Figure S5. The detailed data of AFM measurement, Figure S6. The kinetics of MB labelled pegylated PBNPs pre injection; post injection immediately; 1, 2, and 3 h post injection, Figure S7. (a) The XRD-diagram of the unmodified PBNPs ( $2\theta = 10\text{--}50^\circ$ ). (b) The XRD diagram of the modified PBNPs. XRD: X-ray diffraction; PBNPs: Prussian Blue nanoparticles, Figure S8/I (a) FT-IR spectra of unmodified PBNP (mid-IR region =  $4,000\text{--}750\text{ cm}^{-1}$ ). (b) FT-IR spectra of Methylene blue (mid-IR region =  $4,000\text{--}750\text{ cm}^{-1}$ ). (c) FT-IR spectra of PEG 6000 (mid-IR region =  $4,000\text{--}750\text{ cm}^{-1}$ ). (d) FT-IR spectra of pegylated, fluorescent PBNPs (mid-IR region =  $4,000\text{--}750\text{ cm}^{-1}$ ), Figure S8/II (a) the FT-IR spectra of unmodified PBNPs. (b) FT-IR spectra of Methylene blue. (c) FT-IR spectra of PEG 6000. (d) FT-IR spectra of pegylated, fluorescent PBNPs.

**Author Contributions:** Conceptualization, L.F.; methodology, L.F., N.H., K.S. and D.M.; software, L.F., N.H., I.H., B.K., G.J. and T.K.; validation, L.F., N.H., K.S. and D.M.; formal analysis, L.F.; investigation, L.F.; resources, N.H., I.H., B.K., N.K., G.J., K.S. and D.M.; data curation, L.F., N.H., I.H., B.K., N.K., Z.V., G.J. and T.K.; writing—original draft preparation, L.F.; writing—reviewing and editing, L.F., N.H., P.P., K.S. and D.M.; visualization, L.F. and I.H.; supervision, N.H., K.S. and D.M.; project administration, K.S. and D.M.; funding acquisition, L.F., N.H., T.K., K.S. and D.M. All authors have read and agreed to the published version of the manuscript.

**Funding:** The research leading to these results has received funding from the European Union's Seventh Framework Programme (FP7/2007–2013) under Grant Agreements HEALTH-F2-2011-278850 (INMiND), FP7 HEALTH-305311 (INSERT), and TÁMOP-4.2.1./B-09/1/KMR-2010-0001. K.S. was supported by the Janos Bolyai Research Fellowship Program of the Hungarian Academy of Sciences. T.J.K. acknowledges support from the Hungarian Government's Operative Programme of Economics and Innovation Support, grant number GINOP 2.3.2-15-2016-00016. Part of the research was financed by the Thematic Excellence Programme (TKP) of the Ministry of Innovation and Technology of Hungary, within the framework of the BIOImaging Excellence programme at Semmelweis University. COST Action CA16122 supported part of our work. Part of this study was supported by the National Research, Development and Innovation Office of Hungary (NKFI; NVKP-16-1-2016-0017 National Heart Program).

**Acknowledgments:** The authors acknowledge the helpful discussions with Miklós Kellermayer (Department of Biophysics and Radiation Biology, Semmelweis University).

**Conflicts of Interest:** The authors declare no conflict of interest.

## References

1. Chance, B. Optical method. *Annu. Rev. Biophys. Biophys. Chem.* **1991**, *20*, 1–30. [[CrossRef](#)] [[PubMed](#)]
2. Demos, S.G.; Gandour-Edwards, R.; Ramsamooj, R.; de Vere White, R. Near-infrared autofluorescence imaging for detection of cancer. *J. Biomed. Opt.* **2004**, *9*, 587–593. [[CrossRef](#)] [[PubMed](#)]
3. Van de Ven, S.M.; Elias, S.G.; Wiethoff, A.J.; Van der Voort, M.; Nielsen, T.; Brendel, B.; Van Beek, M. Diffuse optical tomography of the breast: Preliminary findings of a new prototype and comparison with magnetic resonance imaging. *Eur. Radiol.* **2009**, *19*, 1108. [[CrossRef](#)] [[PubMed](#)]

4. Kosaka, N.; Ogawa, M.; Choyke, P.L.; Kobayashi, H. Clinical implications of near-infrared fluorescence imaging in cancer. *Future Oncol.* **2009**, *5*, 1501–1511. [[CrossRef](#)] [[PubMed](#)]
5. US Food and Drug Administration. FDA Guidance for Industry, Investigators, and Reviewers. Exploratory IND Studies. 2006. Available online: <https://www.fda.gov/media/72325/download> (accessed on 24 August 2018).
6. Xu, W.; Riikonen, J.; Nissinen, T.; Suvanto, M.; Rilla, K.; Li, B.; Lehto, V.P. Amine surface modifications and fluorescent labeling of thermally stabilized mesoporous silicon nanoparticles. *J. Phys. Chem. C* **2012**, *116*, 22307–22314. [[CrossRef](#)]
7. Naeini, A.T.; Adeli, M.; Vossoughi, M. Poly (citric acid)-block-poly (ethylene glycol) copolymers—New biocompatible hybrid materials for nanomedicine. *Nanomed. Nanotechnol. Biol. Med.* **2010**, *6*, 556–562. [[CrossRef](#)]
8. Zhang, L.; Wang, Y.; Tang, Y.; Jiao, Z.; Xie, C.; Zhang, H.; Zhang, C. High MRI performance fluorescent mesoporous silica-coated magnetic nanoparticles for tracking neural progenitor cells in an ischemic mouse model. *Nanoscale* **2013**, *5*, 4506–4516. [[CrossRef](#)] [[PubMed](#)]
9. Di, W.; Ren, X.; Zhao, H.; Shirahata, N.; Sakka, Y.; Qin, W. Single-phased luminescent mesoporous nanoparticles for simultaneous cell imaging and anticancer drug delivery. *Biomaterials* **2011**, *32*, 7226–7233. [[CrossRef](#)]
10. World Health Organization. *World Health Organization Model List of Essential Medicines: 21st List 2019*; (No. WHO/MVP/EMP/IAU/2019.06); World Health Organization: Geneva, Switzerland, 2019.
11. Wagner, M.; Suarez, E.R.; Theodoro, T.R.; Machado Filho, C.D.A.S.; Gama, M.F.M.; Tardivo, J.P.; Pinhal, M.A.S. Methylene blue photodynamic therapy in malignant melanoma decreases expression of proliferating cell nuclear antigen and heparanases. *Clin. Exp. Dermatol. Exp. Dermatol.* **2012**, *37*, 527–533. [[CrossRef](#)]
12. Gupta, R.C. *Handbook of Toxicology of Chemical Warfare Agents*; Academic Press: Cambridge, MA, USA, 2015.
13. Szigeti, K.; Hegedűs, N.; Rácz, K.; Horváth, I.; Veres, D.S.; Szöllősi, D.; Kovács, N. Thallium labeled citrate-coated prussian blue nanoparticles as potential imaging agent. *Contrast Media Mol. Imaging* **2018**, *2018*. [[CrossRef](#)]
14. Shokouhimehr, M.; Soehnlén, E.S.; Khitrin, A.; Basu, S.; Huang, S.D. Biocompatible Prussian blue nanoparticles: Preparation, stability, cytotoxicity, and potential use as an MRI contrast agent. *Inorg. Chem. Commun.* **2010**, *13*, 58–61. [[CrossRef](#)]
15. Namazi, H.; Adeli, M. Dendrimers of citric acid and poly (ethylene glycol) as the new drug-delivery agents. *Biomaterials* **2005**, *26*, 1175–1183. [[CrossRef](#)] [[PubMed](#)]
16. Perrier, M.; Busson, M.; Massasso, G.; Long, J.; Boudousq, V.; Pouget, J.P.; Borrás, M. 201 Tl<sup>+</sup>-labelled Prussian blue nanoparticles as contrast agents for SPECT scintigraphy. *Nanoscale* **2014**, *6*, 13425–13429. [[CrossRef](#)] [[PubMed](#)]
17. Máthé, D.; Szigeti, K. Prussian Blue Based Nanoparticle as Multimodal Imaging Contrast Material. U.S. Patent Application No. 13/985,254, 15 February 2014.
18. Cheng, L.; Gong, H.; Zhu, W.; Liu, J.; Wang, X.; Liu, G.; Liu, Z. PEGylated Prussian blue nanocubes as a theranostic agent for simultaneous cancer imaging and photothermal therapy. *Biomaterials* **2014**, *35*, 9844–9852. [[CrossRef](#)] [[PubMed](#)]
19. US Food and Drug Administration. Radiogardase Prussian Blue Insoluble Capsules. 2008. Available online: [https://www.accessdata.fda.gov/drugsatfda\\_docs/label/2008/021626s007lbl.pdf](https://www.accessdata.fda.gov/drugsatfda_docs/label/2008/021626s007lbl.pdf) (accessed on 25 August 2008).
20. Phillips, E.; Penate-Medina, O.; Zanzonico, P.B.; Carvajal, R.D.; Mohan, P.; Ye, Y.; Strauss, H.W. Clinical translation of an ultrasmall inorganic optical-PET imaging nanoparticle probe. *Sci. Transl. Med.* **2014**, *6*, 260ra149. [[CrossRef](#)]
21. Shokouhimehr, M.; Soehnlén, E.S.; Hao, J.; Griswold, M.; Flask, C.; Fan, X.; Huang, S.D. Dual purpose Prussian blue nanoparticles for cellular imaging and drug delivery: A new generation of T1-weighted MRI contrast and small molecule delivery agents. *J. Mater. Chem.* **2010**, *20*, 5251–5259. [[CrossRef](#)]
22. Wang, D.; Zhou, J.; Chen, R.; Shi, R.; Zhao, G.; Xia, G.; Guo, Z. Controllable synthesis of dual-MOFs nanostructures for pH-responsive artemisinin delivery, magnetic resonance and optical dual-modal imaging-guided chemo/photothermal combinational cancer therapy. *Biomaterials* **2016**, *100*, 27–40. [[CrossRef](#)]
23. Penet, M.F.; Mikhaylova, M.; Li, C.; Krishnamachary, B.; Glunde, K.; Pathak, A.P.; Bhujwala, Z.M. Applications of molecular MRI and optical imaging in cancer. *Future Med. Chem.* **2010**, *2*, 975–988. [[CrossRef](#)]

24. National Institute of Biomedical Imaging and Engineering. 2016 Fact Sheet: Optical Imaging. Available online: [https://www.nibib.nih.gov/sites/default/files/Optical%20Imaging%202016-english\\_FINAL.pdf](https://www.nibib.nih.gov/sites/default/files/Optical%20Imaging%202016-english_FINAL.pdf) (accessed on 20 July 2016).
25. Dumont, M.F.; Yadavilli, S.; Sze, R.W.; Nazarian, J.; Fernandes, R. Manganese-containing Prussian blue nanoparticles for imaging of pediatric brain tumors. *Int. J. Nanomed.* **2014**, *9*, 2581. [[CrossRef](#)]
26. Tu, C.; Nagao, R.; Louie, A.Y. Multimodal magnetic-resonance/optical-imaging contrast agent sensitive to NADH. *Angew. Chem. Int. Ed.* **2009**, *48*, 6547–6551. [[CrossRef](#)]
27. Shcherbo, D.; Merzlyak, E.M.; Chepurnykh, T.V.; Fradkov, A.F.; Ermakova, G.V.; Solovieva, E.A.; Chudakov, D.M. Bright far-red fluorescent protein for whole-body imaging. *Nat. Methods* **2007**, *4*, 741–746. [[CrossRef](#)]
28. Kaplan, J.A. *Essentials of Cardiac Anesthesia E-Book: A Volume in Essentials of Anesthesia and Critical Care*; Elsevier Health Sciences: Amsterdam, The Netherlands, 2008.
29. Mondal, S.B.; Gao, S.; Zhu, N.; Liang, R.; Gruev, V.; Achilefu, S. Real-time fluorescence image-guided oncologic surgery. In *Advances in Cancer Research*; Academic Press: Cambridge, MA, USA, 2014; Volume 124, pp. 171–211. [[CrossRef](#)]
30. Canard, J.M.; Letard, J.C.; Palazzo, L.; Penman, I.D.; Lennon, A.M. *Gastrointestinal Endoscopy in Practice E-Book: Expert Consult: Online and Print*; Elsevier Health Sciences: Amsterdam, The Netherlands, 2011.
31. Shanks, G.D. Control and elimination of plasmodium vivax. In *Advances in Parasitology*; Academic Press: Cambridge, MA, USA, 2012; Volume 80, pp. 301–341. [[CrossRef](#)]
32. Deng, T.; Li, J.S.; Jiang, J.H.; Shen, G.L.; Yu, R.Q. Preparation of near-IR fluorescent nanoparticles for fluorescence-anisotropy-based immunoagglutination assay in whole blood. *Adv. Funct. Mater.* **2006**, *16*, 2147–2155. [[CrossRef](#)]
33. Zhang, W.; Ma, D.; Du, J. Prussian blue nanoparticles as peroxidase mimetics for sensitive colorimetric detection of hydrogen peroxide and glucose. *Talanta* **2014**, *120*, 362–367. [[CrossRef](#)] [[PubMed](#)]
34. Vázquez-González, M.; Torrente-Rodríguez, R.M.; Kozell, A.; Liao, W.C.; Ceconello, A.; Campuzano, S.; Willner, I. Mimicking peroxidase activities with prussian blue nanoparticles and their cyanometalate structural analogues. *Nano Lett.* **2017**, *17*, 4958–4963. [[CrossRef](#)] [[PubMed](#)]
35. Chen, Y.; Wu, L.; Wang, Q.; Wu, M.; Xu, B.; Liu, X.; Liu, J. Toxicological evaluation of Prussian blue nanoparticles after short exposure of mice. *Hum. Exp. Toxicol.* **2016**, *35*, 1123–1132. [[CrossRef](#)]
36. Zhang, X.; Rojas, J.C.; Gonzalez-Lima, F. Methylene blue prevents neurodegeneration caused by rotenone in the retina. *Neurotox. Res.* **2006**, *9*, 47–57. [[CrossRef](#)]
37. He, X.; Wu, X.; Wang, K.; Shi, B.; Hai, L. Methylene blue-encapsulated phosphonate-terminated silica nanoparticles for simultaneous in vivo imaging and photodynamic therapy. *Biomaterials* **2009**, *30*, 5601–5609. [[CrossRef](#)]
38. Seong, D.Y.; Kim, Y.J. Enhanced photodynamic therapy efficacy of methylene blue-loaded calcium phosphate nanoparticles. *J. Photochem. Photobiol. B Biol.* **2015**, *146*, 34–43. [[CrossRef](#)]
39. Chen, H.; Ma, Y.; Wang, X.; Zha, Z. Multifunctional phase-change hollow mesoporous Prussian blue nanoparticles as a NIR light responsive drug co-delivery system to overcome cancer therapeutic resistance. *J. Mater. Chem. B* **2017**, *5*, 7051–7058. [[CrossRef](#)]
40. Jolivet, J.P.; Gzara, M.; Mazieres, J.; Lefebvre, J. Physicochemical study of aggregation in silver colloids. *J. Colloid Interface Sci.* **1985**, *107*, 429–441. [[CrossRef](#)]
41. Siiman, O.; Bumm, L.A.; Callaghan, R.; Blatchford, C.G.; Kerker, M. Surface-enhanced Raman scattering by citrate on colloidal silver. *J. Phys. Chem.* **1983**, *87*, 1014–1023. [[CrossRef](#)]
42. Manson, J.; Kumar, D.; Meenan, B.J.; Dixon, D. Polyethylene glycol functionalized gold nanoparticles: The influence of capping density on stability in various media. *Gold Bull.* **2011**, *44*, 99–105. [[CrossRef](#)]
43. Costello, L.C.; Franklin, R.B. Plasma citrate homeostasis: How it is regulated; and Its physiological and clinical implications. An important, but neglected, relationship in medicine. *HSOA J. Hum. Endocrinol.* **2016**, *1*. [[CrossRef](#)]
44. Granchi, D.; Baldini, N.; Ulivieri, F.M.; Caudarella, R. Role of citrate in pathophysiology and medical management of bone diseases. *Nutrients* **2019**, *11*, 2576. [[CrossRef](#)]
45. Harris, D.C.; Bertolucci, M.D. *Symmetry and Spectroscopy: An Introduction to Vibrational and Electronic Spectroscopy*; Courier Corporation: Mineola, NY, USA, 1989.

46. Skoog, D.A.; West, D.M.; Holler, F.J.; Crouch, S.R. *Fundamentals of Analytical Chemistry*; Nelson Education: Scarborough, ON, Canada, 2013.
47. Christian, G.D. *Analytical Chemistry*; John Wiley & Sons: Hoboken, NJ, USA, 2007.
48. Diao, S.; Blackburn, J.L.; Hong, G.; Antaris, A.L.; Chang, J.; Wu, J.Z.; Dai, H. Fluorescence imaging in vivo at wavelengths beyond 1500 nm. *Angew. Chem.* **2015**, *127*, 14971–14975. [[CrossRef](#)]
49. Hong, G.; Zou, Y.; Antaris, A.L.; Diao, S.; Wu, D.; Cheng, K.; Wu, J.Z. Ultrafast fluorescence imaging in vivo with conjugated polymer fluorophores in the second near-infrared window. *Nat. Commun.* **2014**, *5*, 1–9. [[CrossRef](#)]
50. Long, J.; Guari, Y.; Guérin, C.; Larionova, J. Prussian blue type nanoparticles for biomedical applications. *Dalton Trans.* **2016**, *45*, 17581–17587. [[CrossRef](#)]
51. Timchalk, C.; Creim, J.A.; Sukwarotwat, V.; Wiacek, R.; Addleman, R.S.; Fryxell, G.E.; Yantasee, W. In vitro and in vivo evaluation of a novel ferrocyanide functionalized nanoporous silica decorporation agent for cesium (Cs) in rats. *Health Phys.* **2010**, *99*, 420. [[CrossRef](#)]
52. Peter, C.; Hongwan, D.; Küpfer, A.; Lauterburg, B.H. Pharmacokinetics and organ distribution of intravenous and oral methylene blue. *Eur. J. Clin. Pharmacol.* **2000**, *56*, 247–250. [[CrossRef](#)]
53. Brady, C.E., III; DiPalma, J.A.; Morawski, S.G.; Santa Ana, C.A.; Fordtran, J.S. Urinary excretion of polyethylene glycol 3350 and sulfate after gut lavage with a polyethylene glycol electrolyte lavage solution. *Gastroenterology* **1986**, *90*, 1914–1918. [[CrossRef](#)]
54. Baumann, A.; Piel, I.; Hucke, F.; Sandmann, S.; Hetzel, T.; Schwarz, T. Pharmacokinetics, excretion, distribution, and metabolism of 60-kDa polyethylene glycol used in BAY 94-9027 in rats and its value for human prediction. *Eur. J. Pharm. Sci.* **2019**, *130*, 11–20. [[CrossRef](#)] [[PubMed](#)]
55. Perrier, M.; Gallud, A.; Ayadi, A.; Kennouche, S.; Porredon, C.; Gary-Bobo, M.; Basile, I. Investigation of cyano-bridged coordination nanoparticles Gd 3+/[Fe (CN) 6] 3−/d-mannitol as T 1-weighted MRI contrast agents. *Nanoscale* **2015**, *7*, 11899–11903. [[CrossRef](#)] [[PubMed](#)]
56. Souris, J.S.; Lee, C.H.; Cheng, S.H.; Chen, C.T.; Yang, C.S.; Ja-an, A.H.; Lo, L.W. Surface charge-mediated rapid hepatobiliary excretion of mesoporous silica nanoparticles. *Biomaterials* **2010**, *31*, 5564–5574. [[CrossRef](#)]
57. Liu, Z.; Davis, C.; Cai, W.; He, L.; Chen, X.; Dai, H. Circulation and long-term fate of functionalized, biocompatible single-walled carbon nanotubes in mice probed by Raman spectroscopy. *Proc. Natl. Acad. Sci. USA* **2008**, *105*, 1410–1415. [[CrossRef](#)]
58. Liang, X.; Deng, Z.; Jing, L.; Li, X.; Dai, Z.; Li, C.; Huang, M. Prussian blue nanoparticles operate as a contrast agent for enhanced photoacoustic imaging. *Chem. Commun.* **2013**, *49*, 11029–11031. [[CrossRef](#)] [[PubMed](#)]



© 2020 by the authors. Licensee MDPI, Basel, Switzerland. This article is an open access article distributed under the terms and conditions of the Creative Commons Attribution (CC BY) license (<http://creativecommons.org/licenses/by/4.0/>).

## RESEARCH ARTICLE

# Synthesis and preclinical application of a Prussian blue-based dual fluorescent and magnetic contrast agent (CA)

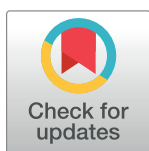
Nikolett Hegedűs<sup>1</sup>✉, László Forgách<sup>1</sup>✉\*, Bálint Kiss<sup>1</sup>‡, Zoltán Varga<sup>1,2</sup>‡, Bálint Jezsó<sup>2</sup>‡, Ildikó Horváth<sup>1</sup>, Noémi Kovács<sup>1</sup>‡, Polett Hajdrik<sup>1</sup>‡, Parasuraman Padmanabhan<sup>3,4</sup>, Balázs Gulyás<sup>3,4,5</sup>, Krisztián Szigeti<sup>1</sup>, Domokos Máthé<sup>1,6,7</sup>

**1** Department of Biophysics and Radiation Biology, Semmelweis University, Budapest, Hungary, **2** Institute of Science, Budapest, Hungary, **3** Lee Kong Chian School of Medicine, Nanyang Technological University, Singapore, Singapore, **4** Cognitive Neuroimaging Centre, Nanyang Technological University, Singapore, Singapore, **5** Department of Clinical Neuroscience, Karolinska Institute, Stockholm, Sweden, **6** CROmed Translational Research Centers, Budapest, Hungary, **7** In Vivo Imaging Advanced Core Facility, Hungarian Center of Excellence for Molecular Medicine (HCEMM), Budapest, Hungary

✉ These authors contributed equally to this work.

‡ BK, ZV, BJ, NK and PH also contributed equally to this work.

\* [forgach.laszlo@med.semmelweis-univ.hu](mailto:forgach.laszlo@med.semmelweis-univ.hu)



## OPEN ACCESS

**Citation:** Hegedűs N, Forgách L, Kiss B, Varga Z, Jezsó B, Horváth I, et al. (2022) Synthesis and preclinical application of a Prussian blue-based dual fluorescent and magnetic contrast agent (CA). PLoS ONE 17(7): e0264554. <https://doi.org/10.1371/journal.pone.0264554>

**Editor:** Kaisar Raza, Central University of Rajasthan, INDIA

**Received:** August 17, 2021

**Accepted:** February 12, 2022

**Published:** July 20, 2022

**Peer Review History:** PLOS recognizes the benefits of transparency in the peer review process; therefore, we enable the publication of all of the content of peer review and author responses alongside final, published articles. The editorial history of this article is available here: <https://doi.org/10.1371/journal.pone.0264554>

**Copyright:** © 2022 Hegedűs et al. This is an open access article distributed under the terms of the [Creative Commons Attribution License](https://creativecommons.org/licenses/by/4.0/), which permits unrestricted use, distribution, and reproduction in any medium, provided the original author and source are credited.

**Data Availability Statement:** Yes - all data are available without restriction. Supplemental information to the results presented in the study

## Abstract

The aim of this study was to develop and characterize a Prussian Blue based biocompatible and chemically stable T1 magnetic resonance imaging (MRI) contrast agent with near infrared (NIR) optical contrast for preclinical application. The physical properties of the Prussian blue nanoparticles (PBNPs) (iron (II); iron (III); octadecacyanide) were characterized with dynamic light scattering (DLS), zeta potential measurement, atomic force microscopy (AFM), and transmission electron microscopy (TEM). In vitro contrast enhancement properties of PBNPs were determined by MRI. In vivo T1-weighted contrast of the prepared PBNPs was investigated by MRI and optical imaging modality after intravenous administration into NMRI-Foxn1 nu/nu mice. The biodistribution studies showed the presence of PBNPs predominantly in the cardiovascular system. Briefly, in this paper we show a novel approach for the synthesis of PBNPs with enhanced iron content for T1 MRI contrast. This newly synthesized PBNP platform could lead to a new diagnostic agent, replacing the currently used Gadolinium based substances.

## Introduction

Magnetic resonance imaging (MRI) is widely used in the clinics as the pre-eminent whole body diagnostic tool to resolve morphology and functionality of the human body. Oftentimes the intrinsic MR contrasts of different biological tissues are not effective enough for high spatial resolution imaging. In these cases, the application of extrinsic contrast agents (CA) is mandatory. These materials are responsible for the shortening of transverse T2/T2\* (negative



are available from figshare at: <https://doi.org/10.6084/m9.figshare.17260385.v1>.

**Funding:** This study was funded by H2020 European Institute of Innovation and Technology in the form of a grant [739593], by the Semmelweis University in the form of funds to NH [STIA-KFI-2020], and by the János Bolyai Research Fellowship Program of the Hungarian Academy of Science in the form of funds to ZV and KS. This study was also funded in part by the Thematic Excellence Programme (TKP) of the Ministry of Innovation and Technology of Hungary, within the framework of the BIOImaging Excellence programme at Semmelweis University, in the form of funds to LF.

**Competing interests:** The authors have declared that no competing interests exist.

contrast), or the longitudinal T1 (positive contrast) relaxation times of water molecules, and their application leads to negative (dark contrast) or positive (enhanced light contrast) areas in images [1, 2].

Iron-based particles, as MR active CAs [3, 4] have been studied for well in the past [5–7]. Their known T2/T2\* shortening properties are translated into very large values for r2 (transverse relaxivity). This produces a negative contrast in MR images. Because of this, their clinical application is difficult as it is not always possible to differentiate if the signals come from the CA or a different biological tissue which is rich in blood, calcium, or other metals. It is also not convenient to medically report and monitor darkened areas in MR image instead of bright spots. Altogether, these factors contributed to the limited clinical application of iron based CAs and the intense research for positive T1 MR contrast materials [8–10].

Gadolinium (III)-containing CAs, as positive MR contrast materials seemed ideal T1 CA in the clinics during the 2000s [11, 12]. They cause hyperintense regions on the MR scans with excellent temporal and spatial resolution [13]. However, the European Commission has withdrawn all linear chelator-bound Gd-based contrast agents from the market in June 2018 based on the declaration of the European Medicines Agency (EMA; EMA/625317/2017) dated 19 December 2017. That declaration described those types of contrast agent might lead to severe toxic effects due to their accumulation in the brain. Further application of nonlinear, macrocyclic Gd contrast agents could be questioned as well due to their recently published adverse effects. It also can be assumed that the marketing authorizations of most of the presently applied Gd contrast agents could be cancelled.

In recent years, iron-based nanoparticle based T1 CAs became one of the most intensively researched domains in radiology [14]. They are built up from a magnetic core—it has size-dependent MR contrast property—and a biocompatible coat that reduces surface tension and ensures the colloidal stability of the sample. Their variable ultra-small size (1–500 nm), superparamagnetic behavior, biocompatibility, and chemical stability position them among the most frequently studied nanomaterials for biomedical applications. The final properties of their formulations depend on the combination of magnetic core and the coating. [2].

The blue nano-sized iron-based Prussian Blue precipitate (Prussian blue nanoparticles, PBNPs) seems to be an ideal CA base for T1 magnetic imaging. It has been used for nearly 300 years in electrochemical and biochemical experiments [15, 16]. In 2003 Prussian blue nanoparticle has been authorized and released (Radiogardase®) by the Food and Drug Administration (FDA) for human use. Originally, this compound was used for the treatment of heavy metal poisoning relying on the complexing property of Prussian blue [17]. Several methods are known for the synthesis (e.g., direct, or indirect) of Prussian blue nanoparticles with different shapes, sizes and stability depending on the applied method [18–20]. Due to the associated biocompatible shell comprising of organic acids and polymers, nanoparticles can be hidden from the immune cells and their biological half-life can be increased in the circulation [21, 22].

One of the widely used capping agents is citric acid, which directly affects the particle size. The higher the citric acid concentration, the smaller the particle size due to an increased reduction rate of the solution. This finding suggests that pH plays a crucial role during the synthesis of PBNPs [23].

Native Prussian blue nanoparticles show very weak contrast in T1 and T2-enhanced in vitro MRI images. Their measured relaxation times did not allow their application for in vivo studies. But it is known from the literature that both the size and the content of the particles and the ordered structure of nearby water molecules have significant effects on the MR contrast-enhancing properties of nanoparticles [24].

In pre-clinical routine, anatomical MR scans are often coupled with some higher functional contrast providing imaging modalities. Optical imaging (OI) could be an appropriate modality

associated with the MR technique for diagnostic and molecular imaging purposes due to their safety, relatively low cost as well as the high spatial resolution and real-time imaging capability. The only minor disadvantage of this technique is the limit of penetration depth of the applied light due to its scattering and absorption. However, this weakness is less of an issue by intraoperative guidance when tumors are directly revealed by the surgeon [25]. Furthermore, the application of near infrared light (NIR; 650–900 nm) for OI excitation could increase the light penetration into tissue up to 0.5–1.5 mm due to the weakened absorption of tissue chromophores, including oxyhemoglobin, deoxyhemoglobin, and melanin, while the scattering of the applied excitation light is negligible [26, 27]. Based on these features, OI is on its way to become a widely adopted method for tumor detection and image-guided surgery in the clinics [28–30].

Furthermore, with theragnostic outlook, PBNPs with their strong optical absorbance in the above-mentioned NIR window and excellent thermal conversion capability have been considered [31] as efficient photoacoustic contrast agents and they could act as an ideal imaging agent [17, 32–35].

For these reasons, our aim was to highly improve the T1 MR signal of Prussian blue particles with appropriate particle sizing and coating, while we also wished to eliminate the T2 contrast from the system. Additionally, the conjugated IR820 NIR fluorescent dye ensures higher tissue contrast in superficial regions even at lower concentration of dye. We aimed at a synthesis method that leads to a stable PB-CA for dual in vivo imaging.

## Materials and methods

### Citrate coated PB production

Citrate-coated PBNPs were produced with the process as described by Shokouhimehr [36]. A two-step PBNP preparation was made. Reactant solutions were made first, Solution A containing 20 mL of 1.0 mM Fe (III) chloride anhydrous ( $\text{FeCl}_3$ ; Merck KGaA, Darmstadt, Germany) with 0.5 mmol of citric acid (Merck KGaA), while Solution B contained 20 mL of 1.0 mM anhydrous potassium ferrocyanide ( $\text{K}_4[\text{Fe}(\text{CN})_6]$ ; Merck KGaA, Darmstadt, Germany) with 0.5 mmol citric acid (Merck KGaA) solution. Next, these solutions were mixed using fast stirring for 10 min at 60°C.

### Production of uncoated PBNPs

Native PBNPs were synthesized again according to as described by Shokouhimehr [36], with modifications. As first step, the reactant solutions were made with Solution A contains 20 mL of 1.0 mM Fe(III) chloride anhydrous ( $\text{FeCl}_3$ ; Merck KGaA, Darmstadt, Germany) with 6 drops of 1 N HCl (Merck KGaA), while Solution B contained 20 mL of 1.0 mM potassium ferrocyanide anhydrous ( $\text{K}_4[\text{Fe}(\text{CN})_6]$ ; Merck KGaA, Darmstadt, Germany) with 6 drops of 1 N HCl (Merck KGaA). Secondly, these solutions were mixed slowly under vigorous stirring for 10 min at 60°C.

### Preparation of fluorescent PBNP nanoparticle complexes

Following the coated and uncoated particle syntheses, the two different types of PBNPs were mixed under vigorous stirring for 10 min at 60°C. With 10 minutes passed, 5 g Chelex 100 (chelating ion exchange resin, Merck KGaA, Darmstadt, Germany)/100 mL solution was applied to eliminate the superfluous metal or alkali metal ions from the system [37]. This suspension was stirred and incubated for one hour, whereby the styrene divinylbenzene copolymer beads were separated from the PBNP solution. In the next step, PBNPs were isolated from the complex suspension using ultracentrifugation (Eppendorf 5424R centrifuge, 21130 rcf) at 4°C for 30 min.

We also produced a batch of uncoated PBNPs and fluorescent PBNP complexes, using the same method with a slight modification. Subsequently the production of reaction solutions of uncoated and complex PBNPs, we included an additional step of differential velocity centrifugation in the synthesis. The reaction of uncoated PBNP solutions were sedimented (Eppendorf 5424R centrifuge) 2 at times 1000 rcf and 2 times at 2000 rcf for 10 minutes consecutively. The PBNP complexes were centrifuged (Eppendorf 5424R centrifuge) 2 times at 2000 rcf for 10 minutes; one batch was filtered through a 0.22  $\mu\text{m}$  membrane filter (MILLEX GP 0.22  $\mu\text{m}$ ; Merck KGaA, Darmstadt, Germany) and centrifuged at 2000 rcf for 10 minutes. As a final step, we isolated the particles by ultracentrifugation (Eppendorf 5424R centrifuge, 21130 rcf) at 4°C for 30 minutes. To achieve fluorescence in the PBNPs, 0.1 mg/mL IR820 NIR dye was filtered through a 0.22  $\mu\text{m}$  membrane filter (MILLEX GP 0.22  $\mu\text{m}$ ; Merck KGaA, Darmstadt, Germany). 10  $\mu\text{L}$  of this filtered dye solution was adsorbed to the particles in 300  $\mu\text{L}$  PBNP solution for a one-hour incubation.

### Dynamic light scattering (DLS) and Zeta measurement

The surface charge and hydrodynamic diameter of the particles were determined using a Litesizer 500 (Anton Paar, Hamburg, Germany). DLS measurement was performed at 25°C in automatic mode (for backscatter detector fixed at 175°; for side scatter 90° detector angle; for front scatter 15° detector angle) using a 633 nm He-Ne laser. Samples were measured in Omega cuvettes (Anton Paar, Hamburg, Germany). Measurement of zeta potential was performed under similar conditions. The measurement data were evaluated using software provided by the manufacturer, and statistical data and graphs were created and evaluated with Origin 9.0 (OriginLab) and Microsoft Excel 2013 software. DLS measurements were performed weekly for a period of 4 weeks to determine colloidal stability. Samples were stored at 4°C.

### Transmission Electron Microscopy (TEM)

Morphological investigations of the NPs were carried out on a JEOL TEM 1011 TEM (JEOL, Peabody, MA, USA) operated at 80 kV. The camera used for image acquisition was a Morada TEM 11 MPixel from Olympus (Olympus, Tokyo, Japan) using iTEM5.1 software for metadata analysis. Diluted sample was dropped and dried on a carbon-coated copper grid. Size distribution was determined by manually measuring the diameter of 1059 particles on the images, using a software custom designed for this purpose (tem\_circlefind by András Wacha, MTA TTK, Hungary).

### Atomic Force Microscopy (AFM)

For imaging PBNP complexes, two-fold diluted samples were applied onto poly-L-lysine (PLL)-coated surfaces. PLL-coated substrate surface was prepared by pipetting 100  $\mu\text{L}$  of PLL (0.1% w/v) onto freshly cleaved mica, followed by incubation for 20 min, repeated rinsing with purified water, and drying with a stream of high-purity nitrogen gas. AFM images were collected in noncontact mode with a Cypher S instrument (Asylum Research, Santa Barbara, CA, USA) at 1 Hz line-scanning rate in air, using a silicon cantilever (OMCL AC-160TS, Olympus, Tokyo, Japan) oscillated at its resonance frequency (270–300 MHz). Temperature during the measurements was  $25 \pm 1^\circ\text{C}$ . AFM amplitude-contrast images are shown in this paper. The filter used on the images enhances the details of the amplitude contrast images (mud). AFM images were analyzed by using the built-in algorithms of the AFM driver software (Igor Pro, Wave Metrics Inc., Lake Oswego, OR, USA). Particle statistics was done by analyzing a  $2 \mu\text{m} \times 2 \mu\text{m}$  height-contrast image with ( $n = 178$ ) particles. Maximum height values were taken as the height of particles, and rectangularity was calculated as the ratio of the particle



area to the area of a nonrotated inscribing rectangle. The closer a particle is to a rectangle, the closer this value is to unity.

## Animals

*In vivo* imaging tests of the PBNP nano systems were carried out in NMRI FOXN nu/nu male mice (Janvier, France). Animals had ad libitum access to food and water and were housed under temperature-, humidity-, and light-controlled conditions. All procedures were conducted in accordance with the ARRIVE guidelines and the guidelines set by the European Communities Council Directive (86/609 EEC) and approved by the Animal Care and Use Committee of Semmelweis University (protocol number: PE/EA/1468-8/2019). Mice were 10–12 weeks old with an average body weight of  $27 \pm 7$  g. During imaging, animals were kept under anesthesia using a mixture of 2.5% isoflurane gas and medical oxygen. Their body temperature was maintained at 37°C throughout imaging. For the most humane termination of the animals, intravenous Euthasol (pentobarbital/phenytoin) injection was used.

## *In vitro* and *in vivo* MRI measurements

MRI measurements were performed *in vitro* with a nanoScan® PET/MR system (Mediso, Hungary), having a 1 T permanent magnetic field, 450 mT/m gradient system using a volume transmit/receive coil with a diameter of 60 mm. MRI T1 relaxation rates and r1 relaxivity were calculated from inversion prepared snapshot gradient echo (T1 map, IR GRE SNAP 2D) images acquired with 60 x 90 mm FOV (field of view), plane resolution of 1 mm, slice thickness of 5 mm, 6 averages, TR/TE 4005/1.7, TI 10, 60, 100, 150, 200, 250, 300, 350, 400, 500, 700, 900, 1200, 2500, 4000 ms. MRI-signal enhancement of PBNPs was measured for three different Fe (III) concentrations (13.75 mM, 41.25 mM, and 82.5 mM) in 1.5 mL Eppendorf tubes. After scanning, the concentration dependent signal changes were calculated and compared to the signal of saline.

Experiments were performed in an adult male mouse under isoflurane anesthesia (5% for induction and 1.5–2% to maintain the appropriate level of anesthesia; Baxter, Arrane). Precisely, 300 µL of IR820-labelled PBNP solution containing 3 mg of Fe (III) in a 30 mg/mL concentration PBNP solution was administered intravenously into the tail. The T1-weighted MRI biodistribution images were collected at two different time points (pre- and post-injection) The MRI scans were performed with gradient echo (T1 GRE 3D) images acquired with 100 mm x 40 mm FOV, matrix size 200 x 80, slice thickness of 0.5 mm, 4 averages, TR/TE 75/4, dwell time 25 ms. Images were further analyzed with Fusion (Mediso Ltd., Hungary) and VivoQuant (inviCRO LLC, US) dedicated image analysis software.

## *In vitro* and *in vivo* Fluorescence-labeled Organism Bioimaging Instrument (FOBI) measurements

The fluorescent labelled PBNPs were imaged using a two-dimensional epifluorescent optical imaging instrument. (FOBI, Neoscience Co. Ltd., Suwon-si, Korea). For *in vitro* scans, 0.5 mL of samples were tested with the following imaging parameters: excitation at 680 nm corresponding to the excitation maximum of the dye (excitation: 690 nm; emission: 820 nm), exposure time: 1000 msec and gain: 1. The emission spectrum of the dye was in the pass band of the used emission filter.

Experiments were performed in an adult male mouse under isoflurane anesthesia (5% for induction and 1.5–2% to maintain the appropriate level of anesthesia; Baxter, Arrane). Precisely, 300 µL of IR820-labelled PBNP solution was administered intravenously into the tail vein. The biodistribution images were collected at two different time points (pre- and post-

injection) with excitation of 680 nm corresponding to the excitation maximum of the dye (excitation: 690 nm; emission: 820 nm). The emission spectrum of the dye was in the pass band of the used emission filter. Image acquisition parameters were the following: exposure time: 1000 msec and gain: 1. The images were evaluated with VivoQuant software (Invivo, 27 Drydock Avenue, Boston, MA, USA).

## Results and discussion

### The structure of PBNPs

The final PBNP complex nano structure was prepared by the combination of Shokouhimehr's method [36] and our previously published one-step citrate coated PBNP procedure [22]. The synthesis of PBNPs with and without coating resulted in two different types of PBNP solutions, which were mixed. During the incubation and mixing period, the particles were able to connect to each other via carboxyl groups of citric acid and a form a bigger and iron-rich formula. The porous surface of the nanoparticles assured the conjugation points for the fluorescent IR820 dye (Fig 1).

### Output parameters of nanoparticle characterization methods

Many articles investigated the differences between the possible methods used for characterization of nano-sized objects, nanosuspensions and nanoparticles. Even though in the fields of

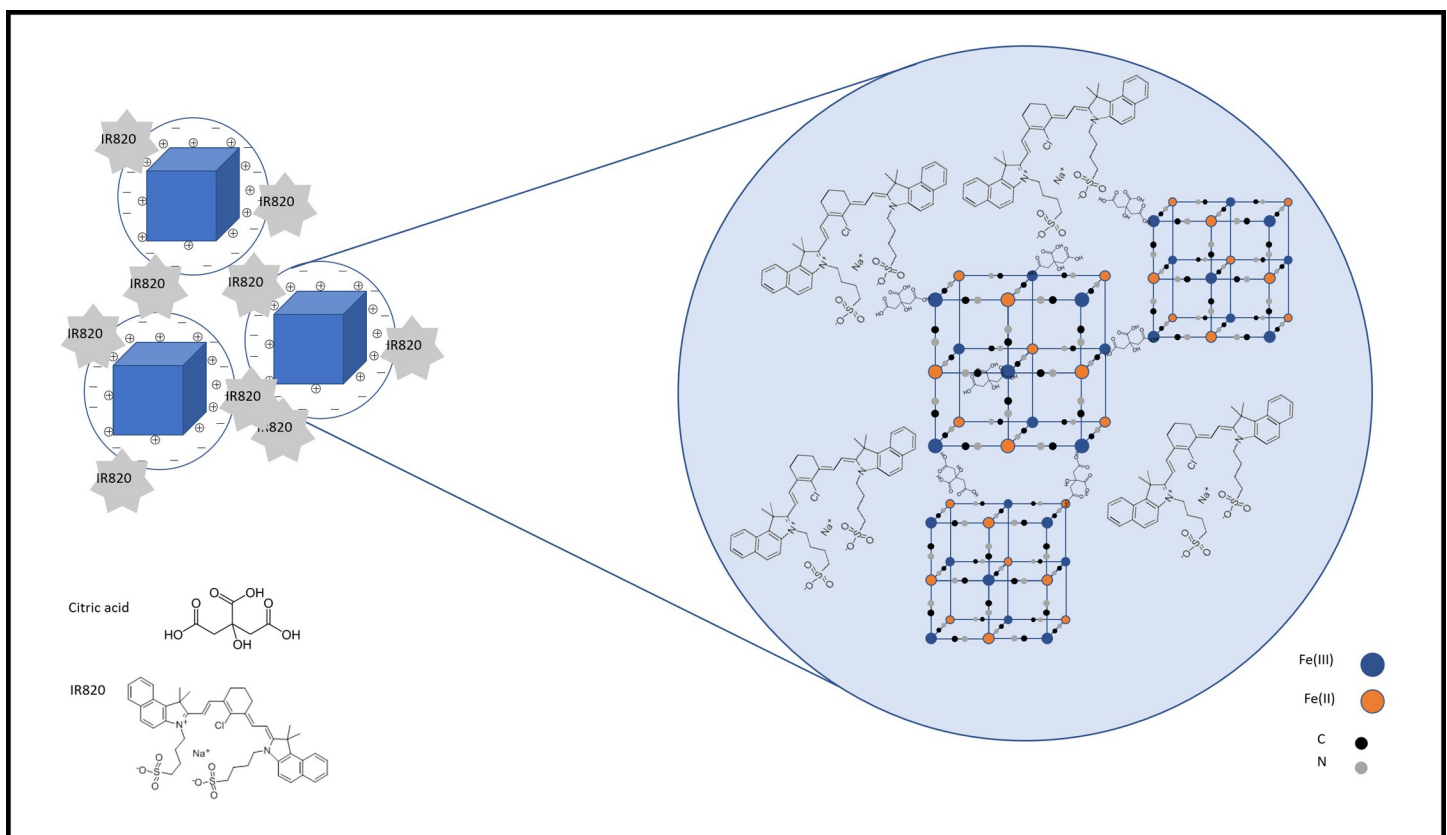


**Fig 1. Schematic illustration of the presumed connection of Prussian blue nanoparticles (PBNPs) with and without coating and the particle conjugation by IR820.** The blue halo around the PBNPs represent the non-biocompatible PBNP-species (PB-HCl) acting as a coating surface. The colors represent the following ions or atoms, respectively: blue: Fe (III); orange: Fe (II); black: C; gray: N.

<https://doi.org/10.1371/journal.pone.0264554.g001>

materials science and chemical engineering, there is a strong need for different types of measurements of the same materials, however the interpretation and the proper understanding of each method is needed to achieve the desired goals. The most frequently used methods to describe a nano system are the DLS, the AFM and the TEM. These methods differ from each other regarding the mathematical basics, the methods of, sensitivity and robustness; a direct comparison is unattainable, hence in most studies, not only one size-range, but a size distribution in form of either a histogram or figure is found [38–40].

For a better understanding of our results, the raw measurement data to our article in the supplemental information section of the manuscript is attached (S1-S4 Figs in [S1 File](#)).

### DLS and Zeta potential

The applied citric acid as surface-capping agent controlled the size and the biocompatibility of the synthesized particles and seemed an appropriate agent to avoid agglomeration [41]. The created nanoparticles were a colloidal stable system. The mean hydrodynamic diameter (intensity-based harmonic average) of complex PBNPs was  $82.91 \pm 1.21$  (average  $\pm$  SD), as determined by DLS. This had only changed slightly with time. There was no significant colloidal alteration during the 4-week duration of the study, as the calculated  $0.244 \pm 0.014$  polydispersity index (PDI) shows the PBNPs did not flocculate or aggregate during this time (not illustrated). The mean zeta potential of PBNPs at the measured pH range did not exceed 15 mV ( $n = 3$ ). At pH 7.4 the zeta potential was  $-33.3 \pm 3.8$  mV ( $n = 3$ ).

### Atomic force microscopy

AFM is a widely used imaging modality to measure and manipulate sub-nanometer samples [39]. During a measurement only the height of the particles could be determined due to the tip convolution which leads to artificially modified lateral dimensions on the images [42]. The measured width of the particles was influenced by tip convolution. [Fig 2](#) shows PBNPs on AFM images as objects with a flat rectangular surface protruding from a rounded halo. The rectangular surface represents the real geometry of the particles while their halo is the consequence of tip convolution, i.e., the effect of imaging a rectangular prism by a tetrahedral AFM tip. Rectangularity of the particles (together with their halo) was found to be  $0.774 \pm 0.111$  (mean  $\pm$  SD), indicating that PBNPs indeed represent rectangular topography. The height of the particles was  $36.457 \pm 9.496$  nm (mean  $\pm$  SD) ([Fig 2](#)).

### Transmission electron microscopy

The non-hydrated shape and size of the PBNPs were investigated with TEM. PBNPs appeared flat rectangular, dense objects in this case as well. The mean diameter of the nanoparticles was  $30.14 \pm 10.656$  nm (average  $\pm$  SD) ([Fig 3](#)), along with an average surface area of  $579.257 \pm 398.983$  nm<sup>2</sup> (mean  $\pm$  SD;  $n = 1059$  particles). The measured height by TEM was in good correlation with the results of AFM measurements describing the shape of non-hydrated particles. By both cases, the flat rectangular objects represent the real geometry of the particles ([Fig 3](#)).

### Magnetic resonance imaging

To demonstrate the positive MR contrast enhancing property of our PBNP sample, T1-weighted images of a phantom (containing three different Fe (III) concentrations (13.75 mM, 41.25 mM, and 82.5 mM) containing PBNP solutions) were scanned to visually evaluate the signal enhancement on T1-weighted image. Based on the inversion prepared gradient echo

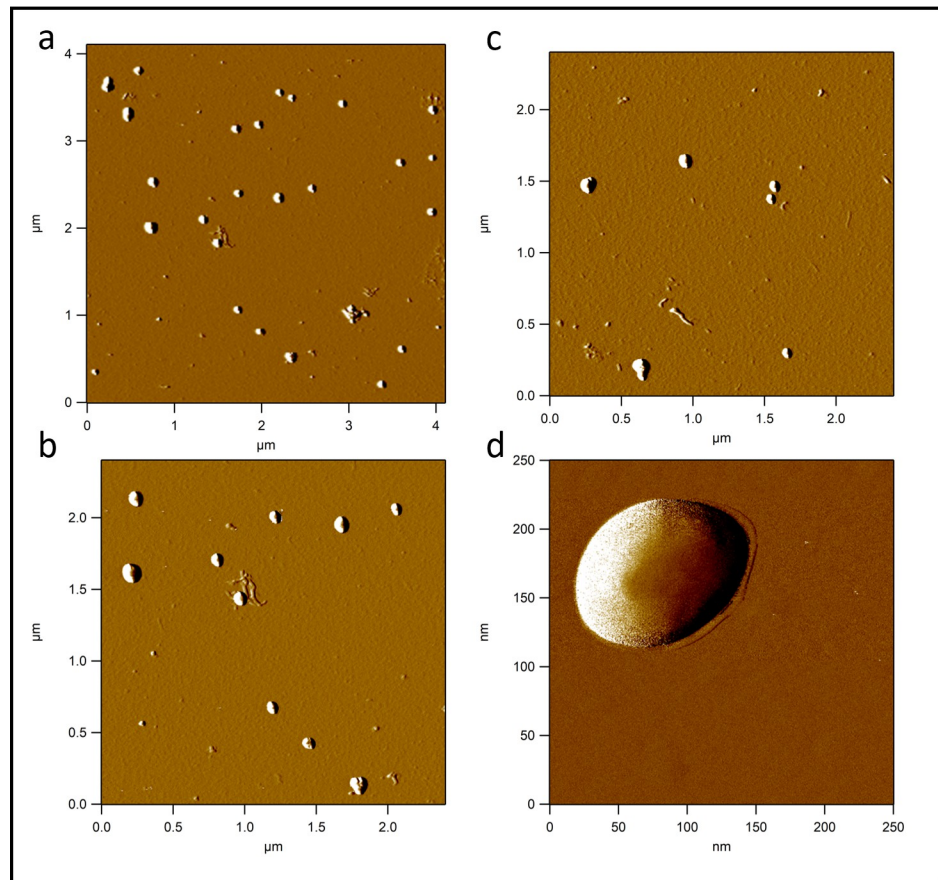


**Fig 2. Atomic force microscopy (AFM) amplitude-contrast images with different magnification of PBNPs on mica surface.** PBNPs on AFM images as objects with a flat rectangular surface protruding from a rounded halo. The rectangular surface represents the real geometry of the particles while their halo is the consequence of tip convolution. Rectangularity of the particles (together with their halo) was found to be  $0.774 \pm 0.111$  (mean  $\pm$  SD), indicating that PBNPs indeed represent rectangular topography. The height of the particles was  $36.457 \pm 9.496$  nm (mean  $\pm$  SD). The size of the images are  $4.125 \mu\text{m} \times 4.125 \mu\text{m}$  (Fig 2A),  $2.5 \mu\text{m} \times 2.5 \mu\text{m}$  (Fig 2B and 2C) and  $250 \text{ nm} \times 250 \text{ nm}$  (Fig 2D) respectively.

<https://doi.org/10.1371/journal.pone.0264554.g002>

scan and the multislice multiecho scan T1 relaxations rate were calculated. Afterward from these values, longitudinal relaxivity ( $r_1 = 0.0008 \pm 0.0002 \text{ mM}^{-1} \text{ ms}^{-1}$ ) was calculated. The more significant T1 shortening effect for PBNPs could be explained by a carbon-bound and low-spin of  $\text{Fe}^{2+}$  in the PB structure, in contrast to the high spin nitrogen-bound  $\text{Fe}^{3+}$  [36]. Our result demonstrates that PBNPs have substantial T1 MRI contrast compared to other T1 CAs [43, 44].

Nanoparticles without any conjugated specific *in vivo* targeting agent are initially dispersed in the circulation system and started to accumulate mainly in the reticuloendothelial system (RES; e.g. liver, spleen) [45, 46]. To investigate the PBNP uptake efficiency, especially in RES, the PBNP distribution was determined on T1-weighted MR images (Fig 4). In the case of *in vivo* MRI scans, we were able to register contrast changes between the pre- and post-injection scans immediately after the PBNP administration. Enhanced signal intensities were registered in the lungs, liver, kidneys, and abdominal vein (Fig 4), which supports the results of previous publication [47].



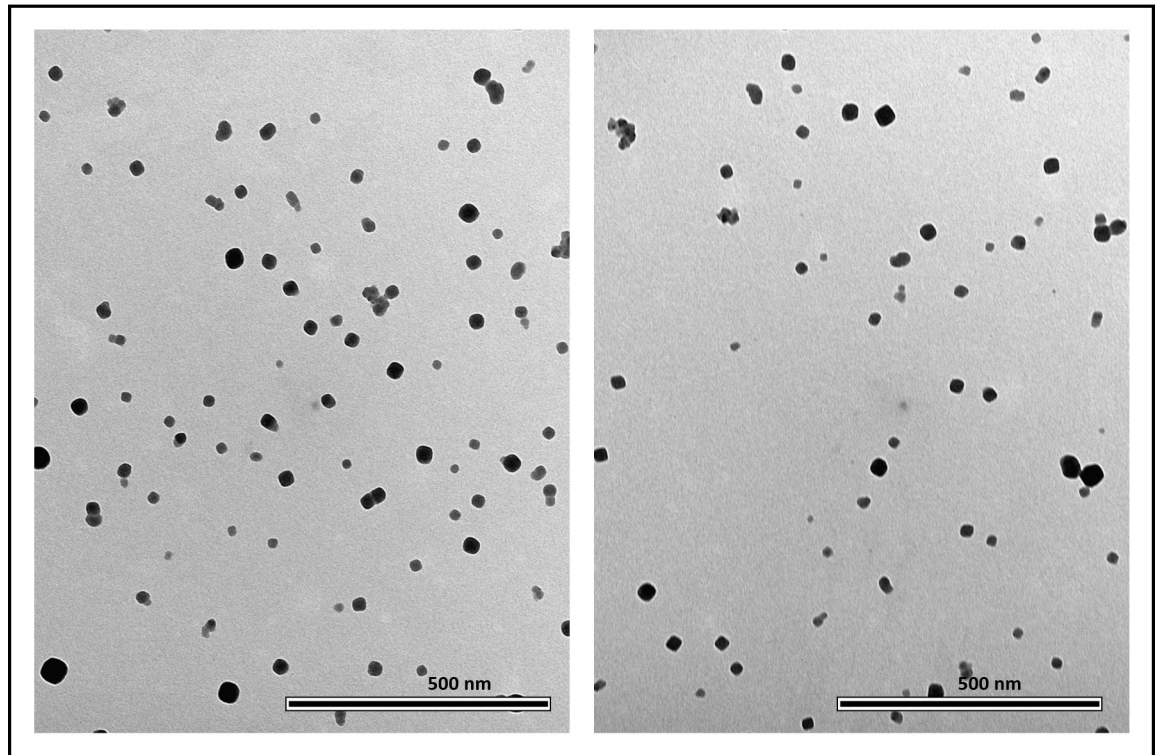


**Fig 3. TEM images of PBNPs on carbon-coated copper grid.** PBNPs appeared flat rectangular, dense objects. The mean diameter of the nanoparticles was  $30.14 \pm 10.656$  nm (average  $\pm$  SD). The smaller objects on the image are individual PBNP particles which are not conjugated into the final PBNP complex. Scale bar is 500 nm.

<https://doi.org/10.1371/journal.pone.0264554.g003>

### Optical imaging

Due to the strong visible fluorescent signal of IR820 conjugated PBNPs the semiquantitative distribution of the particles was determined based on their normalized mean fluorescent intensity. Fig 5A illustrates the autofluorescence signal from the animal at pre-injection condition at 690 nm, while Fig 5B shows the fluorescent signal after the PBNP administration. Enhanced dye concentration was registered in the head and thoracic region based on the high dye content of the circulation system, furthermore the images illustrated the liver of the animal. According to the studies of Zhang et. al. and Huang et. al., IR820 connected to different types of carrier systems shows great photo- and pH stability, as well as in aqueous media [48, 49] (Fig 5).

### The toxicity of PBNPs

To evaluate the biocompatibility, PBNPs were widely investigated and involved in cellular uptake, cell viability and toxicity studies. Shokouhimehr et. al. reported no possible toxicity of modified PBNPs on HEK-293 cells, furthermore, the cell viability was measured to be ca. 98% [36]. Additionally, Feng and colleagues were modifying PBNPs to make a new type of anticancer drug. Their experiments included the measurement of PBNPs on 4T1 cell line. The reported cell viability in this case was also above 90%, moreover, the relatively high (0.5 mg/mL) PBNP concentrations were also unable to induce cytotoxicity [50].

The cellular uptake of PBNPs was also examined several times; mesenchymal C3HT10T1/2 stem cells (MSC) were treated with the nanoparticles and the results were evaluated using

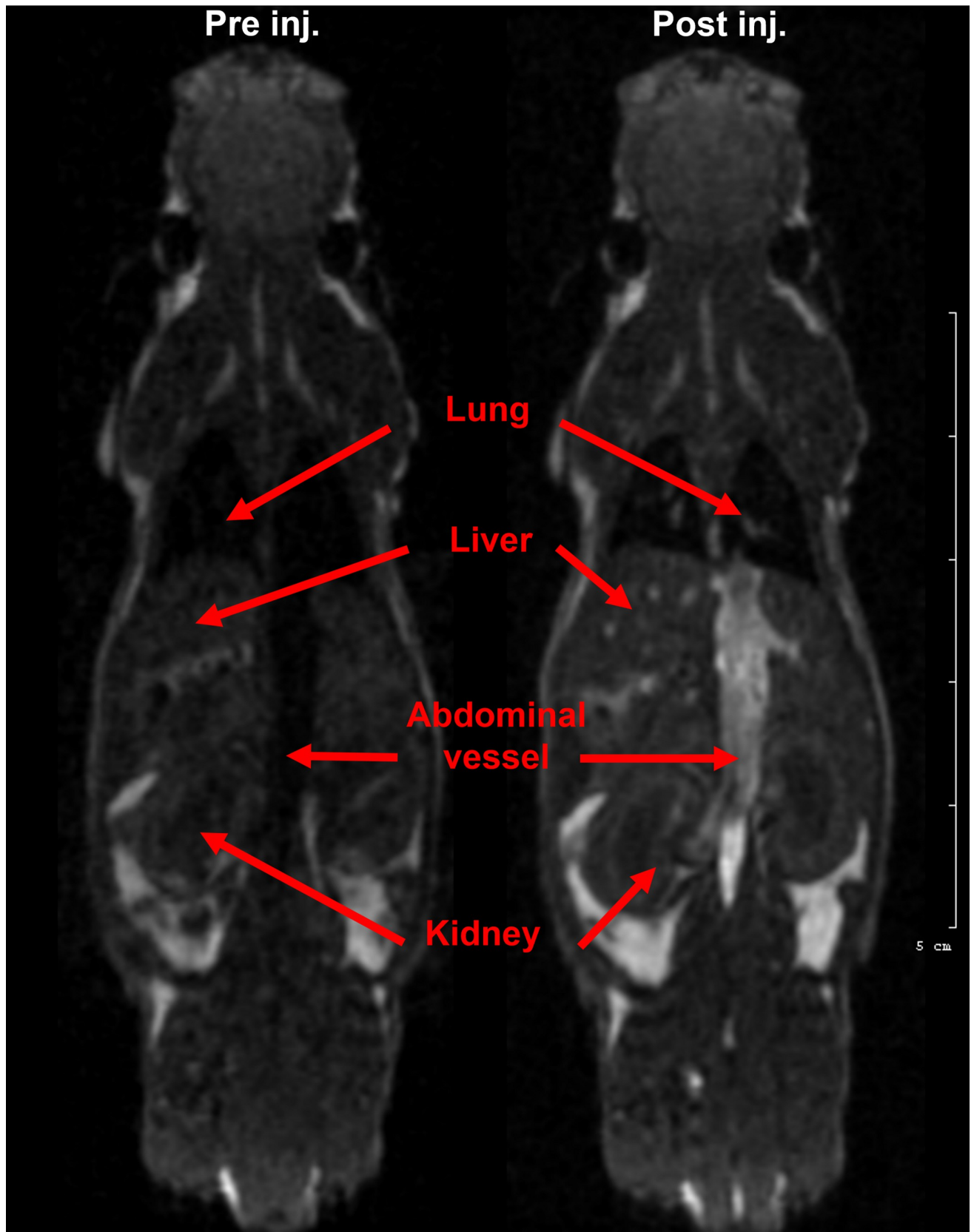


**Fig 4.** Axial T1-weighted MR images of a mouse (A) before and (B) after intravenous administration of Prussian Blue. Red arrows indicate that regions where signal intensity changes happened. Enhanced signal intensities were registered in the lungs, liver, kidneys, and abdominal vessel, which supports the results of a previous publication [47].

<https://doi.org/10.1371/journal.pone.0264554.g004>

TEM. After incubation, PBNPs were detected in the cytoplasm of the MSCs, but the cellular uptake was not yet described. The suggested mechanism of action could be like other types of noble metal and inorganic nanoparticles, which can be taken up via endocytosis, according to Kim et. al., Lu et. al. and Pan et. al. [51–54]. The cytotoxicity on the MSCs was studied for 72 hours, yet these experiments also suggested the lack of toxic effect as well as the lack of influence on the proliferation of MSCs [51].

Based on the broad spectrum of data regarding this matter, we conclude, that our PBNP-complexes have no potential cytotoxic nor proliferation-influencing effect on the cells of living organisms. Regarding the *in vivo* toxicity, our previous measurements suggested that PBNPs would be excreted by biliary as well as renal routes, mostly during a 72-hour period [22, 55].

## Conclusions

In conclusion, the synthesized NIR-820 conjugated PBNP nanoparticles seem an appropriate MRI and optical contrast material. The surface modification of citrate coated PBNPs with coatless nanoparticles produced slightly enlarged, iron rich complex nano system with enhanced *in vitro* and *in vivo* T1-weighted MR contrast. The further conjugation with NIR-820 dye resulted an optically active complex nano material for *in vivo* use. This nano system reported here exhibited high colloidal stability and monodispersity after each modification step. Its relaxivity constants demonstrated that this nano material is an appropriate candidate for further MRI and OI investigation.

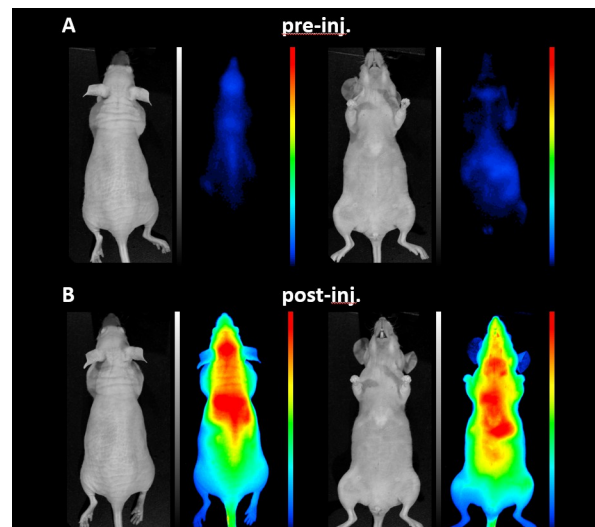


**Fig 5.** White and fluorescent images of a mouse (A) before and (B) after intravenous administration of Prussian Blue (images from left to right: prone white, prone fluorescent, supine white, supine fluorescent images) at 690 nm. After the PBNP administration enhanced dye concentration was registered in the head and thoracic region based on the high dye content of the circulation system, furthermore the images illustrated the liver of the animal. The images are highlighted on the same dynamic color look-up table, which illustrates the signal intensity with different tone from cold to hot colors.

<https://doi.org/10.1371/journal.pone.0264554.g005>

## Supporting information

**S1 File.**  
(DOCX)

## Acknowledgments

P. P. and B. G. acknowledges the support from Imaging Probe Development Platform (IPDP) of Lee Kong Chian School of Medicine and from the Cognitive Neuroimaging Centre (CONIC) at Nanyang Technological University, Singapore.

## Author Contributions

**Conceptualization:** Nikolett Hegedűs.

**Methodology:** Nikolett Hegedűs, László Forgách, Bálint Kiss, Zoltán Varga, Bálint Jezsó, Noémi Kovács, Polett Hajdrik, Domokos Máthé.

**Project administration:** Nikolett Hegedűs, Domokos Máthé.

**Supervision:** Balázs Gulyás, Krisztián Szigeti, Domokos Máthé.

**Visualization:** Nikolett Hegedűs, László Forgách, Ildikó Horváth, Noémi Kovács.

**Writing – original draft:** Nikolett Hegedűs.

**Writing – review & editing:** László Forgách, Parasuraman Padmanabhan, Balázs Gulyás, Domokos Máthé.

## References

1. Bhavesh R, Lechuga-Vieco A.V., Ruiz-Cabello J, & Herranz F. T1-MRI fluorescent iron oxide nanoparticles by microwave assisted synthesis. *Nanomaterials*. 2015; 5(4): 1880–1890. <https://doi.org/10.3390/nano5041880> PMID: 28347101
2. Rosado-de-Castro P.H., Morales M.D.P., Pimentel-Coelho P.M., Mendez-Otero R., & Herranz F. Development and application of nanoparticles in biomedical imaging. 2018.
3. Bulte J.W.M. Kraitchman D.L. Iron oxide MR contrast agents for molecular and cellular imaging. *NMR Biomed*. 2004; 17: 484–499. <https://doi.org/10.1002/nbm.924> PMID: 15526347
4. Babes .L, Denizot B., Tanguy G., Le Jeune J.J., Jallet P. Synthesis of Iron Oxide Nanoparticles Used as MRI Contrast Agents: A Parametric Study. *J. Colloid Interface Sci*. 1999; 212: 474–482. <https://doi.org/10.1006/jcis.1998.6053> PMID: 10092379
5. Pöselt E., Kloust H., Tromsdorf U., Janschel M., Hahn C., Maßlo C., et al. Relaxivity Optimization of a PEGylated Iron-Oxide-Based Negative Magnetic Resonance Contrast Agent for T2-Weighted Spin-Echo Imaging. *ACS Nano* 2012; 6: 1619–1624. <https://doi.org/10.1021/nn204591r> PMID: 22276942
6. Lartigue L., Innocenti C., Kalaivani T., Awwad A., Sanchez D., del Mar M., et al. Water-dispersible sugar-coated iron oxide nanoparticles. An evaluation of their relaxometric and magnetic hyperthermia properties. *J. Am. Chem. Soc*. 2011; 133: 10459–10472. <https://doi.org/10.1021/ja111448t> PMID: 21604803
7. Mccarthy JR., Weissleder R. Multifunctional magnetic nanoparticles for targeted imaging and therapy. *Adv. Drug Deliv. Rev*. 2008; 60: 1241–1251. <https://doi.org/10.1016/j.addr.2008.03.014> PMID: 18508157
8. Cunningham C.H., Arai T., Yang P.C., McConnell M.V., Pauly J.M., Conolly S.M. Positive contrast magnetic resonance imaging of cells labeled with magnetic nanoparticles. *Magn. Reson. Med*. 2005; 53: 999–1005. <https://doi.org/10.1002/mrm.20477> PMID: 15844142
9. Xiao N., Gu W., Wang H., Deng Y., Shi X., Ye L. T1-T2 dual-modal MRI of brain gliomas using PEGylated Gd-doped iron oxide nanoparticles. *J. Colloid Interface Sci*. 2014; 417: 159–165. <https://doi.org/10.1016/j.jcis.2013.11.020> PMID: 24407672
10. Hu F., Zhao Y.S. Inorganic nanoparticle-based T1 and T1/T2 magnetic resonance contrast probes. *Nanoscale* 2012; 4: 6235–6243. <https://doi.org/10.1039/c2nr31865b> PMID: 22971876



11. Zhou Z., and Zheng-Rong L. Gadolinium-based contrast agents for magnetic resonance cancer imaging. Wiley Interdisciplinary Reviews: Nanomed. Nanobiotechnol. 2013; 5: 1–18.
12. Silvio A., Botta M., and Terreno E. Gd (III)-based contrast agents for MRI." *Adv Inorg Chem.* 2005; 57: 173–237.
13. Merbach A.S., Helm L., and Toth E. The chemistry of contrast agents in medical magnetic resonance imaging. John Wiley & Sons. 2013.
14. Ventola C.L. The nanomedicine revolution: part 1: emerging concepts. *P T.* 2012; 37(9): 512–525. PMID: [23066345](#)
15. Buser H., Schwarzenbach D., Petter W., Ludi A.J.I.C. The crystal structure of Prussian blue: Fe<sub>4</sub> [Fe (CN)<sub>6</sub>]<sub>3</sub> · xH<sub>2</sub>O. *Inorg. Chem.* 1977; 16(11): 2704–2710.
16. Gautam M., Poudel K., Yong C.S., Kim J.O. Prussian blue nanoparticles: Synthesis, surface modification, and application in cancer treatment. *Int J Pharm.* 2018; 549(1–2): 31–49. <https://doi.org/10.1016/j.ijpharm.2018.07.055> PMID: [30053487](#)
17. Liang X., Deng Z., Jing L., Li X., Dai Z., Li C., Huang M. Prussian blue nanoparticles operate as a contrast agent for enhanced photoacoustic imaging. *Chem. Commun.* 2013; 49(94): 11029–11031. <https://doi.org/10.1039/c3cc42510j> PMID: [23884328](#)
18. Wu Y., Yang H., Shin H.J. Encapsulation and crystallization of Prussian blue nanoparticles by cowpea chlorotic mottle virus capsids. *Biotechnol Lett.* 2014; 36(3):515–521. <https://doi.org/10.1007/s10529-013-1399-8> PMID: [24190479](#)
19. Samain L., Grandjean F., Long G.J., Martinetto P., Bordet P., Strivay. Relationship between the synthesis of Prussian blue pigments, their color, physical properties, and their behavior in paint layers. *J. Phys. Chem. C.* 2013; 117(19): 9693–9712.
20. Adhikamsetty R., Jonnalagadda. Kinetics and mechanism of prussian blue formation. *Bull Chem Soc Ethiop.* 2009; 23(1): 47–54.
21. Fernandes R., Dumont M.F., Sze R.W., Conklin L.S., Hoffman H.A., Jaiswal J.K. Prussian blue-inspired constructs for multimodal imaging and therapy. Google Patents; 2017.
22. Szigeti K., Hegedűs N., Rácz K., Horváth I., Veres D.S., Szöllösi D., et al. Thallium labeled citrate-coated prussian blue nanoparticles as potential imaging agent. *Contrast Media Mol Imaging.* 2018. <https://doi.org/10.1155/2018/2023604> PMID: [29853803](#)
23. Fu G., Liu W., Feng S., & Yue X. Prussian blue nanoparticles operate as a new generation of photothermal ablation agents for cancer therapy. *Chemical communications.* 2012. 48(94): 11567–11569. <https://doi.org/10.1039/c2cc36456e> PMID: [23090583](#)
24. Máthé D., Szigeti K., inventors; Semmelweis Egyetem, assignee. Prussian blue based nanoparticle as multimodal imaging contrast material. United States patent application US 13/985,254. 2014.
25. Wang C., Wang Z., Zhao T., Li Y., Huang G., Sumer B.D., & Gao J. Optical molecular imaging for tumor detection and image-guided surgery. *Biomaterials.* 2018. 157: 62–75. <https://doi.org/10.1016/j.biomaterials.2017.12.002> PMID: [29245052](#)
26. Welzel J. Optical coherence tomography in dermatology: a review. *Skin Res Technol. Review article.* 2001; 7(1): 1–9. <https://doi.org/10.1034/j.1600-0846.2001.007001001.x> PMID: [11301634](#)
27. Ntziachristos V., Bremer C., & Weissleder R. Fluorescence imaging with near-infrared light: new technological advances that enable in vivo molecular imaging. *Eur. Radiol.* 2003; 13(1): 195–208. <https://doi.org/10.1007/s00330-002-1524-x> PMID: [12541130](#)
28. Vahrmeijer A.L., Hutteman M., Van Der Vorst J.R., Van De Velde C.J., & Frangioni J.V. Image-guided cancer surgery using near-infrared fluorescence. *Nature reviews Clinical oncology.* 2013. 10(9): 507–518. <https://doi.org/10.1038/nrclinonc.2013.123> PMID: [23881033](#)
29. Nguyen Q.T., & Tsien R.Y. Fluorescence-guided surgery with live molecular navigation—a new cutting edge. *Nature reviews cancer.* 2013. 13(9): 653–662. <https://doi.org/10.1038/nrc3566> PMID: [23924645](#)
30. Pellico J., Gawne P.J., & de Rosales R.T. Radiolabelling of nanomaterials for medical imaging and therapy. *Chemical Society Reviews.* 2021. <https://doi.org/10.1039/d0cs00384k> PMID: [33491714](#)
31. Moorthy M.S., Hoang G., Subramanian B., Bui N.Q., Panchanathan M., Mondal S., et al. Prussian blue decorated mesoporous silica hybrid nanocarriers for photoacoustic imaging-guided synergistic chemophotothermal combination therapy. *Journal of Materials Chemistry B.* 2018. 6(32): 5220–5233. <https://doi.org/10.1039/c8tb01214h> PMID: [32254759](#)
32. Long J., Guari Y., Guerin C., Larionova J. Prussian Blue Type Nanoparticles for Biomedical Applications *Dalton Trans.* 2016. 45: 17581–17587. <https://doi.org/10.1039/c6dt01299j> PMID: [27278267](#)
33. Peng J.R., Dong M.L., Ran B., Li W.T., Hao Y., Yang Q., et al. "One-for-All"-Type, Biodegradable Prussian Blue/Manganese Dioxide Hybrid Nanocrystal for Trimodal Imaging-Guided Photothermal Therapy and Oxygen Regulation of Breast Cancer *ACS Appl. Mater. Interfaces* 2017. 9: 13875–13886.

34. Cook J.R., Dumani D.S., Kubelick K.P., Luci J., Emelianov S.Y. Prussian blue Nanocubes: Multi-Functional Nanoparticles for Multimodal Imaging and Image-Guided Therapy (Conference Presentation). In *Photons Plus Ultrasound: Imaging and Sensing 2017*; Oraevsky, A. A.; Wang, L. V., Eds.; SPIE Proceedings Vol. 10064.
35. Jing L.J., Liang X.L., Deng Z.J., Feng S.S., Li X.D., Huang M.M., et al. Prussian Blue Coated Gold Nanoparticles for Simultaneous Photoacoustic/CT Bimodal Imaging and Photothermal Ablation of Cancer Biomaterials 2014. 35: 5814–5821. <https://doi.org/10.1016/j.biomaterials.2014.04.005> PMID: 24746962
36. Shokouhimehr M., Soehnlen E.S., Khitrin A., Basu S., & Huang S.D. Biocompatible Prussian blue nanoparticles: Preparation, stability, cytotoxicity, and potential use as an MRI contrast agent. *Inorg. Chem. Commun.* 2010; 13(1): 58–61.
37. BIO-RAD, L. Chelex®-100 and Chelex®-20 Chelating Ion Exchange Resin Instruction Manual. Bio-Rad Laboratories, 2000.
38. Tomaszewska E., Soliwoda K., Kadziola K., Tkacz-Szczesna B., Celichowski G., Cichomski M., et al. (2013). Detection limits of DLS and UV-Vis spectroscopy in characterization of polydisperse nanoparticles colloids. *Journal of Nanomaterials*, 2013.
39. Hoo C. M., Starostin N., West P., & Mecartney M. L. (2008). A comparison of atomic force microscopy (AFM) and dynamic light scattering (DLS) methods to characterize nanoparticle size distributions. *Journal of Nanoparticle Research*, 10(1), 89–96.
40. Eaton P., Quaresma P., Soares C., Neves C., De Almeida M. P., Pereira E., et al. (2017). A direct comparison of experimental methods to measure dimensions of synthetic nanoparticles. *Ultramicroscopy*, 182, 179–190. <https://doi.org/10.1016/j.ultramic.2017.07.001> PMID: 28692935
41. Walker H.K., Hall W.D., and Hurst J.W. *Clinical Methods: The History, Physical, and Laboratory Examinations*. 3rd ed. Boston. Massachusetts. USA. LexisNexis Butterworths. 1990.
42. Baalousha M., and Lead JR. Characterization of natural and manufactured nanoparticles by atomic force microscopy: Effect of analysis mode, environment and sample preparation. *Colloids Surf, A Physicochem Eng Asp.* 2013; 419: 238–247.
43. Sitterberg J., Özçetin A., Ehrhardt C., and Bakowsky U. Utilising atomic force microscopy for the characterisation of nanoscale drug delivery systems. *Eur. J. Pharm. Biopharm.* 2010; 74: 2–13. <https://doi.org/10.1016/j.ejpb.2009.09.005> PMID: 19755155
44. Noebauer-Huhmann I.M., Szomolanyi P., Juras V., Kraff O., Ladd M.E., & Trattnig S. Gadolinium-based magnetic resonance contrast agents at 7 Tesla: in vitro T1 relaxivities in human blood plasma. *Invest Radiol.* 2010; 45(9): 554–558. <https://doi.org/10.1097/RLI.0b013e3181ebd4e3> PMID: 20697225
45. Rohrer M., Bauer H., Mintonovitch J., Requardt M., & Weinmann H.J. Comparison of magnetic properties of MRI contrast media solutions at different magnetic field strengths. *Invest Radiol.* 2005; 40(11): 715–724. <https://doi.org/10.1097/01.rli.0000184756.66360.d3> PMID: 16230904
46. Zhang Y.N., Poon W., Tavares A.J., McGilvray I.D., & Chan WC. Nanoparticle–liver interactions: cellular uptake and hepatobiliary elimination. *J Control Release.* 2016; 240: 332–348. <https://doi.org/10.1016/j.jconrel.2016.01.020> PMID: 26774224
47. Quini C.C., Próspero A.G., Calabresi M.F., Moretto G.M., Zufelato N., Krishnan S., et al. Real-time liver uptake and biodistribution of magnetic nanoparticles determined by AC biosusceptometry. *Nanomedicine*, 2017; 13(4): 1519–1529. <https://doi.org/10.1016/j.nano.2017.02.005> PMID: 28214607
48. Zhang D., Zhang J., Li Q., Tian H., Zhang N., Li Z., et al. (2018). pH-and enzyme-sensitive IR820–paclitaxel conjugate self-assembled nanovehicles for near-infrared fluorescence imaging-guided chemo–photothermal therapy. *ACS applied materials & interfaces*, 10(36), 30092–30102. <https://doi.org/10.1021/acsami.8b09098> PMID: 30118198
49. Huang C., Hu X., Hou Z., Ji J., Li Z., & Luan Y. (2019). Tailored graphene oxide–doxorubicin nanovehicles via near-infrared dye–lactobionic acid conjugates for chemo–photothermal therapy. *Journal of colloid and interface science*, 545, 172–183. <https://doi.org/10.1016/j.jcis.2019.03.019> PMID: 30878783
50. Feng T., Wan J., Li P., Ran H., Chen H., Wang Z., et al. (2019). A novel NIR-controlled NO release of sodium nitroprusside-doped Prussian blue nanoparticle for synergistic tumor treatment. *Biomaterials*, 214, 119213. <https://doi.org/10.1016/j.biomaterials.2019.05.024> PMID: 31146175
51. Wen J., Zhao Z., Tong R., Huang L., Miao Y., & Wu J. (2018). Prussian blue nanoparticle-labeled mesenchymal stem cells: Evaluation of cell viability, proliferation, migration, differentiation, cytoskeleton, and protein expression in vitro. *Nanoscale research letters*, 13(1), 1–10.
52. Kim T., Lemaster J. E., Chen F., Li J., & Jokerst J. V. (2017). Photoacoustic imaging of human mesenchymal stem cells labeled with Prussian blue–poly (l-lysine) nanocomplexes. *ACS nano*, 11(9), 9022–9032. <https://doi.org/10.1021/acs.nano.7b03519> PMID: 28759195

53. Lu J., Ma S., Sun J., Xia C., Liu C., Wang Z., et al. (2009). Manganese ferrite nanoparticle micellar nanocomposites as MRI contrast agent for liver imaging. *Biomaterials*, 30(15), 2919–2928. <https://doi.org/10.1016/j.biomaterials.2009.02.001> PMID: 19230966
54. Pan D., Caruthers S. D., Hu G., Senpan A., Scott M. J., Gaffney P. J., et al. (2008). Ligand-directed nanobialys as theranostic agent for drug delivery and manganese-based magnetic resonance imaging of vascular targets. *Journal of the American Chemical Society*, 130(29), 9186–9187. <https://doi.org/10.1021/ja801482d> PMID: 18572935
55. Forgách L., Hegedűs N., Horváth I., Kiss B., Kovács N., Varga Z., et al. (2020). Fluorescent, Prussian Blue-Based Biocompatible Nanoparticle System for Multimodal Imaging Contrast. *Nanomaterials*, 10(9), 1732. <https://doi.org/10.3390/nano10091732> PMID: 32878344